

# Analytical Models for Calculating the Response of Temporary Soil-Filled Walls Subjected to Blast Loading

By  
Kevin Scherbatiuk

A thesis submitted to  
the Faculty of Graduate Studies  
in partial fulfilment of  
the requirements for the degree of  
**Doctor of Philosophy**

Department of Civil Engineering  
Faculty of Graduate Studies  
University of Manitoba  
Winnipeg, Manitoba

12 2009

© Copyright  
2009, Kevin Scherbatiuk

## Abstract

The aims of the thesis were to study the response of temporary soil-filled walls both experimentally and numerically, and to develop an efficient and accurate analytical model to predict 2-*D* planar response from blast loading which could be used to efficiently calculate a pressure–impulse (*P–I*) curve. An explicit finite element (FE) formulation was constructed using LS-Dyna software, and two analytical models were also derived and presented: a Rigid-Body Rotation model as a preliminary model, and the Rigid-Body Hybrid model as the proposed model of this thesis. Seven full-scale experiments which consisted of blast loading simple free-standing soil-filled Hesco Bastion (HB) walls are presented. Soil densities and moisture contents were measured in the field, and soil properties were obtained from triaxial tests of the samples collected and prepared to match field conditions. All models used some or all of the derived soil properties pertinent to the experiments as input, and whenever possible, the recorded pressure–time histories in the experiments were assumed as the loadings. The results of both analytical models and the FE models were compared with experimental results. In addition, the results were compared with one another within parametric studies concerning sensitivity of model responses to soil properties and different height-to-width ratio walls. The models were also used to calculate and compare *P–I* curves.

The FE models were found to be in excellent agreement in both the post-experiment deformation and the displacement–time histories for the seven experiments (most results

within 5 %). The Rigid-Body Rotation model was found to be in reasonable agreement with the post-experimental deformation in cases where the wall did not critically overturn but sustained moderate rotations. However, comparison with the experimentally derived displacement–time histories showed that it underestimated displacement–time histories and thus it possessed too much resistance. Apart from comparison of an experimental result where the soil-fill in the wall possessed sizable cohesion, the response of the Rigid-Body Hybrid model was in very good agreement with the experiments overall (within 10 %). A general recommendation for the model development follows that a sliding interface should be included in the model to capture sliding behaviour arising from use of soil-fills with substantial cohesion. A soil sensitivity study was conducted and overall very good agreement was reached between the Rigid-Body Hybrid model in comparison with the FE model in its ability to capture differences in displacement–time histories from differences in soil parameters.  $P$ – $I$  curves were developed using the analytical and FE models for the three different wall configurations studied in the experiments. The results demonstrated that the proposed Rigid-Body Hybrid model is useful for calculating a  $P$ – $I$  curve for a HB wall efficiently and yielded very accurate results (within 5 % for the impulse asymptotes). To establish the limitations of both analytical models, an aspect ratio study was conducted where the rotation of the analytical models were compared to that of the FE models for walls of different height-to-empty width ratios, across a range of impulsive loadings. Comparison with the FE model for different height-to-width ratios of walls showed that the Rigid-Body Hybrid model was within 10 % for all rotation angles and predictions of critical overturning impulse for height-to-width ratios of walls  $H/w_a \geq 1.43$ . For walls with  $H/w_a = 1.29$  the Rigid-Body Hybrid model was only in

agreement for rotation angles from 18 to 21 degrees. In view of this narrow range of accuracy, use of the model for walls  $H/w_a \leq 1.29$  in its existing form is not recommended. Consideration of sidewall folding and contact with the ground is proposed to improve its accuracy for walls  $H/w_a \leq 1.29$ . Apart from this, overall the Rigid-Body Hybrid model is on average within 10 % experimental results and FE model results. Recommendations are provided to address minor deficiencies within the model and to expand its range of application.

# Acknowledgments

The author would like to thank John Fowler of DRDC Suffield and Dan Pope of DSTL for their helpful suggestions, along with Keith Gerrard, Tom Storrie, Darrell Boechler, and Steve Mowers, also of DRDC Suffield, for their work in the conduct of the experiments. The author wishes to express his sincere gratitude to his supervisor, Prof. Nipon Rattanawangcharoen, P. Eng., for his guidance in this topic as well as his harsh but constructive advice. Deepest gratitude is extended to the members of the thesis advisory committee, Prof. Qiang Zhang, P. Eng. and Prof. Arvind Shah, P. Eng., and to the external examiner, Prof. Abass Braimah, P. Eng., for their guidance and advice, and substantial effort in reviewing this thesis.

The financial support from the Military Engineering Section is gratefully acknowledged. Sincere thanks are extended to Liz Abitia for helping with the formatting of this thesis. Finally, many thanks are extended towards my parents for their encouragement throughout the course of my studies.

# Dedication

To my parents Bill and Stella.

# Contents

## Front Matter

Contents .....	iii
List of Tables .....	vii
List of Figures .....	viii
List of Symbols .....	xv
List of Appendices .....	xxiv
<b>1 Introduction</b> .....	<b>1</b>
1.1 Objectives .....	3
1.2 Scope .....	4
1.3 Overview of Thesis .....	5
<b>2 Phenomenology and Literature Review</b> .....	<b>7</b>
2.1 Description of HB units .....	7
2.2 Blast loading phenomenology .....	10
2.2.1 Stress waves and shock waves .....	10
2.2.2 Detonation of explosives .....	11
2.2.3 Formation of a blast wave in air .....	12
2.2.4 Blast wave profiles and empirical curve fits .....	13
2.2.5 Blast scaling .....	16
2.2.6 Empirical performance of high explosives .....	17
2.2.7 Equating non-TNT explosives performance to equivalent TNT .....	21
2.2.8 Ground shock .....	22

2.3	Structural response to blast .....	23
2.3.1	SDOF systems.....	23
2.3.2	$P-I$ curves .....	26
2.4	Literature review of Hesco Bastion units.....	30
<b>3</b>	<b>Experimental Investigation</b>	<b>33</b>
3.1	HB wall experiments.....	33
3.1.1	Experiment setup .....	34
3.1.2	Wall details .....	35
3.1.3	Construction of walls .....	37
3.1.4	Laser scanning .....	38
3.1.5	Pressure measurements .....	39
3.1.6	Photo and video.....	41
3.1.7	Displacement and deformed position measurements.....	41
3.2	Soil properties .....	43
3.2.1	Particle size analysis and soil classification.....	44
3.2.2	Densities and moisture contents.....	45
3.2.3	Cone penetration tests .....	47
3.2.4	Yield relationship.....	48
3.2.5	Equation of State (EOS).....	53
3.2.6	Bulk and shear moduli .....	57
<b>4</b>	<b>FE Model</b>	<b>61</b>
4.1	Geometry.....	61
4.2	Material models .....	62
4.3	Initial and boundary conditions .....	65
4.4	Mesh resolution study .....	66
<b>5</b>	<b>Derivation of Analytical Models</b>	<b>67</b>
5.1	Rigid-Body Rotation model.....	67
5.2	A Rigid-Body Hybrid model .....	74
5.2.1	Response mechanism from the FE model.....	75



5.2.2	Assumptions in the formulation of the model.....	76
5.2.3	Derivation of equations of motion .....	79
5.2.4	Reverse Winkler formulation.....	83
5.2.4.1.	Plastic and elastic spring properties .....	83
5.2.4.2.	Deformed configuration of lower portion of wall.....	87
5.2.4.3.	Locating point $E$ .....	91
5.2.4.4.	Locating point $F$ .....	92
5.2.4.5.	Calculation of stresses and forces .....	94
5.2.4.6.	Derivation of shear displacement relationship.....	96
5.2.4.7.	Transformation of forces and locations .....	98
5.2.5	Calculation of inertial properties about the c.g. ....	99
5.2.6	Discretization .....	100
<b>6</b>	<b>Results and Discussion</b>	<b>102</b>
6.1	Experiment results and validations .....	102
6.1.1	Trial 1.....	103
6.1.2	Trial 2.....	106
6.1.3	Trial 3.....	107
6.1.4	Trial 4.....	108
6.1.5	Trial 5.....	113
6.1.6	Trial 6.....	115
6.1.7	Trial 7.....	117
6.2	Discussion of FE model .....	118
6.3	Discussion of Rigid-Body Rotation model .....	123
6.3.1	Examination of analytical behaviour .....	123
6.3.2	Comparison with experiment results .....	125
6.4	Discussion of Rigid-Body Hybrid model .....	127
6.4.1	Comparison with post-experiment deformation .....	127
6.4.2	Effect of cohesive soil-fill.....	128
6.4.3	Comparison of displacement–time histories.....	131
6.4.4	Examination of corner deformation .....	133

6.4.5	Soil sensitivity comparison .....	135
6.5	Calculation and comparison of $P$ – $I$ curves .....	137
6.6	Aspect ratio study and analytical model limitations .....	144
<b>7</b>	<b>Conclusions and Recommendations</b>	<b>149</b>
<b>Back Matter</b>		<b>158</b>
	Bibliography .....	158
	Appendix A .....	165
	Appendix B .....	171
	Appendix C .....	174
	Appendix D .....	176
	Appendix E .....	183
	Appendix F .....	191
	Appendix G .....	195
	Appendix H .....	199
	Appendix I .....	203
	Appendix J .....	207
	Appendix K .....	210

# List of Tables

Table 3.1	Overview of experiments on HB walls.....	34
Table 3.2	Overview of distances for cable displacement gauge setup in Figure 3.1 .....	42
Table 3.3	Soils testing program for the blast experiments.....	43
Table 3.4	Summary of the HB walls tested in each trial.....	47
Table 3.5	Data points for saturated soil from Set 1 triaxial tests .....	49
Table 3.6	Data points for unsaturated soil from Set 2 triaxial tests .....	52
Table 3.7	EOS points for saturated soil using triaxial cell in hydrostatic compression for Set 1 .....	53
Table 3.8	EOS points for unsaturated soil using triaxial cell in hydrostatic compression for Set 2.....	56
Table 3.9	Bulk and shear moduli measurements for Set 1.....	59
Table 3.10	Bulk and shear moduli measurements for Set 2 .....	60
Table 6.1	Summary of the comparison of the results from the Rigid-Body Hybrid model with the results from the experiments for displacement–time histories in Trials 4 through 7 .....	131

# List of Figures

Figure 1.1	HB concertainer® used to construct a protective structure. ....	2
Figure 2.1	Hesco Bastion Concertainer units: (a) folded Mil 3 units; (b), extended Mil 2 units; and (c), view of inside of unit and geotextile flaps of Mil 2 units. ....	8
Figure 2.2	Stages of HB construction: (a) unfolded Mil 1 units aligned in desired configuration and filled with soil; (b), compaction of soil every 30 cm lift..	8
Figure 2.3	Final constructed forms: (a) simple wall; (b), fully encapsulated structure with sheet pile roof.....	9
Figure 2.4	Shock wave development: (a) pressure and relative volume deformation relationship for liquids and gases, (modified from Henrych [5]), (b) formation of a shock front with distance or time, (taken from Cooper [6])	11
Figure 2.5	Formation of a shock wave in air (Source: Kinney and Graham [7]).....	12
Figure 2.6	Idealized pressure time histories Sources: (a) Baker [9] and (b) Gelfand [10] .....	13
Figure 2.7	Comparison of empirical curve fits for an experimental blast wave pressure-time history. ....	15
Figure 2.8	Hopkinson-Cranz scaling (Source: Baker [9]).....	17
Figure 2.9	Charge configurations: a – spherical; b – hemispherical; c – height of burst (Source: Gelfand [10]) .....	18

Figure 2.10	Incident and reflected hemispherical TNT performance as function of hemispherical scaled distance (Source: Remennikov [16]) .....	19
Figure 2.11	Diagram of the successive positions of air-induced and direct-induced ground shock, (dashed curves: sound-wave front; solid curves: front of the first maxima) (Source: Henrych [5]).....	22
Figure 2.12	Beam under time varying pressure loading and equivalent SDOF system..	23
Figure 2.13	Normalized $P-I$ curve for linear elastic oscillator (Source: Baker et al. [20]) .....	27
Figure 2.14	Curve-fitted $P-I$ curve through limited numerically generated points using a hyperbola.....	29
Figure 3.1	Experiment setup .....	35
Figure 3.2	Configurations of HB walls tested: (a) HB Mil 3 two course wall for Trials 1, 2, 4, and 6; (b) HB Mil 2 two course wall for Trial 3; and (c) HB Mil 1 one course wall for Trials 5 and 7.....	36
Figure 3.3	Additional details of HB walls: (a) Coiled joint separating HB columns, shown with clips connecting upper and lower course; (b) geotextile flaps preventing soil from draining along bottom wall sides; and (c) bulge at bottom constrained from geotextile flaps. ....	37
Figure 3.4	Laser scan volume measurements of Mil 3 HB wall in Trial 3: (a) overall volume and (b) geometry of bulges at mid-height.....	38
Figure 3.5	Width $w_a$ and average expanded width $w_b$ of HB columns for different sizes of HB units .....	39

Figure 3.6	Details of reflected pressure gauge setup: (a) pressure gauge in steel circular mount on wall facing the blast; (b) gauge mounted in steel tubing inside Hesco cell before filling; and (c) gauge cables run through rubber hose exiting wall facing away from the blast.....	40
Figure 3.7	Details of displacement gauge setup: (a) retractable cable displacement gauge; and (b) steel framing and protective housing for displacement gauges, (cables shown in dashed lines).....	41
Figure 3.8	Particle size analysis of the silty-sand used in the experiments.....	44
Figure 3.9	Measurement of densities: (a) density measurement for HB wall using nuclear densometer; and (b) manual density measurement. ....	45
Figure 3.10	Mohr-Coulomb analysis and best fit line for Set 1 triaxial tests.....	50
Figure 3.11	Mohr-Coulomb analysis and best fit line for Set 2 triaxial tests.....	52
Figure 3.12	Equation of State obtained from Set 1 triaxial tests.....	54
Figure 3.13	Equation of State obtained from Set 2 triaxial tests.....	57
Figure 4.1	FE model of Mil 3 two-course wall: (a) the entire wall and (b) two half-column model.....	65
Figure 4.2	Comparison of displacement–time histories with different mesh resolutions: (a) horizontal displacement and (b) vertical displacement .....	66
Figure 5.1	Configuration of a rigid-body rotation model: (a) diagram illustrating calculation of inertial properties, (b) 2D elevation view and section a-a ....	68
Figure 5.2	Deformed shape of finite element model and basic formulation of analytical model.....	75

Figure 5.3	Diagrams illustrating analytical model formulation: (a) assuming fixed cg and corner displaces, (b) assuming fixed corner and cg displaces .....	78
Figure 5.4	Free-body diagram for derivation of the equations of motion.....	80
Figure 5.5	Reverse Winkler foundation: (a) wall with soil having continuous compression properties, (b) wall with soil having equivalent spring displacement properties, (c) relationship for pressure as a function of volumetric strain, and (d) relationship for distributed force as a function of spring displacement .....	84
Figure 5.6	Calculation setup for equating $K_v$ to $k_v$ .....	86
Figure 5.7	Diagrams illustrating calculation of forces for reverse Winkler: (a) displacements and stresses, (b) points of interest plotted on spring distributed force versus displacement relationship .....	89
Figure 5.8	Locating points $C$ , $E$ , and $F$ by finding intersection of present displacement plane (line $O_I C$ ) with line of maximum displacement (dashed line), and line of zero stress (solid line) .....	92
Figure 5.9	Calculation of base pressure, equivalent reaction force, and location .....	94
Figure 5.10	Evaluating direction of shear force from horizontal rigid-body velocity at base .....	97
Figure 5.11	Transformation of forces and locations .....	98
Figure 5.12	Diagram illustrating calculation of inertial properties .....	100
Figure 5.13	Vertical displacement–time histories; (a) convergence study for time step size, (b) convergence study for number of discretizations along thickness using $\Delta t=0.1\ ms$ .....	101

Figure 6.1	Results of Trial 1: (a) recorded pressure–time history, (b) post-experiment photograph of the end of the five-column wall.....	103
Figure 6.2	Results of FE model for Trial 1: (a) overlay of maximum FE model response, (b) overlay of final FE model response with the photo of the end column of the wall .....	104
Figure 6.3	Results of analytical models for Trial 1: (a) overlay of maximum response of Rigid-Body Rotation model, (b) overlay of maximum Rigid-Body Hybrid model response.....	105
Figure 6.4	Reflected pressure–time history measured from Trial 2.....	106
Figure 6.5	Results of Trial 3: (a) recorded pressure–time history, (b) post-experiment photograph with overlay of FE model response .....	107
Figure 6.6	Results of analytical models for Trial 3: (a) overlay of maximum response of Rigid-Body Rotation model, (b) overlay of maximum response of Rigid-Body Hybrid model.....	108
Figure 6.7	Results of Trial 4: (a) recorded pressure–time history, (b) post-experiment photograph, (c) comparison of horizontal and vertical displacement–time histories of upper monitoring point, and (d) comparison of experimental and calculated cable displacement–time histories of lower monitoring point..	111
Figure 6.8	Results of Trial 5: (a) recorded pressure–time history, (b) post-experiment photograph, (c) comparison of horizontal and vertical displacement–time histories of upper monitoring point, and (d) comparison of experimental and calculated cable displacement–time histories of lower monitoring point..	114



Figure 6.9	Results of Trial 6: (a) recorded pressure–time history, (b) post-experiment photograph, (c) comparison of horizontal and vertical displacement–time histories of upper monitoring point, and (d) comparison of experimental and calculated cable displacement–time histories of lower monitoring point..	116
Figure 6.10	Results of Trial 7: (a) recorded pressure–time history, (b) post-experiment photograph, (c) comparison of horizontal and vertical displacement–time histories of upper monitoring point, and (d) comparison of experimental and calculated cable displacement–time histories of lower monitoring point..	118
Figure 6.11	Fraction of critical angle $\lambda_\alpha$ as a function of fraction of critical impulse $\lambda_\gamma$ for Rigid-Body Rotation model .....	124
Figure 6.12	Comparison of Rigid-Body Rotation model with post-experiment photo in Trial 3: (a) maximum response of Rigid-Body Rotation model, (b) post-experiment photo .....	126
Figure 6.13	Interaction of friction and internal shear stress.....	128
Figure 6.14	Illustration of determination of shear or sliding behaviour for different soil types: (a) cohesive soil, (b) cohesionless soil .....	130
Figure 6.15	Comparison between assumption of Rigid-Body Hybrid model and result of FE model: (a) Rigid-Body Hybrid model showing no contact of sidewall right of point $O_1$ , (b) FE model showing contact of sidewall with ground through folding.....	134
Figure 6.16	Comparison of Rigid-Body Hybrid (RBH) model to FE model in capturing changes in response to different soil parameters: (a) for $K$ , (b) for EOS slope $K_v$ , (c) for slope of yield relationship $\tan \phi$ , and (d) for density .....	136

Figure 6.17	$P-I$ curves calculated from FE and analytical models for failure defined by overturning: (a) two-course Mil 3 wall, (b) two-course Mil 2 wall.....	140
Figure 6.18	Final positions of FE model for one-course Mil 1 wall resulting from different impulses which illustrate inability to overturn completely: (a) $21^\circ$ rotation, (b) $36^\circ$ rotation, (c) $50^\circ$ rotation.....	142
Figure 6.19	$P-I$ curve for one-course Mil 1 wall for failure defined by $21^\circ$ rotation...	143
Figure 6.20	Rotation as a function of impulse for a range of $H/w_a$ ratios: (a) $H/w_a = 1.29$ (b) $H/w_a = 1.43$ , (c) $H/w_a = 1.57$ , (d) $H/w_a = 1.71$ , (e) $H/w_a = 1.86$ , (f) $H/w_a = 2.0$ .....	145
Figure 6.21	Comparison of post-experimental wall positions for Trial 7: (a) experiment result, (b) final FE model result showing residual angle of top of sidewall at approximately $60^\circ$ .....	148

# List of Symbols

$A$	horizontal distance from initial position of monitoring points to position of retractable displacement gauges
$A_I$	input constant for simplified Johnson-Cook material model
$b$	the thickness of the bulge of a single sidewall
$B_I$	input constant for simplified Johnson-Cook material model
$c$	cohesion of the soil
$c'$	effective cohesion of the soil
$cg$	centre of gravity
$c_1$	input constant for simplified Johnson-Cook material model
$C$	parameter in hyperbolic curve fit that determines how abrupt the transition region is
point $C$	location of intersection of ground with bottom of wall on blast loaded end
point $\hat{C}$	denotes highest compressive displacement experienced at current location of point $C$
$d$	diameter
$d_{EF}$	distance between points $E$ and $F$
$d_{O_1P}$	distance between points $O_1$ and $P$

$d_{PE}$  distance between points  $P$  and  $E$

point  $D$  location of normal force from base compression

$D_{result}$  gives level of damage from model or experiment as function of pressure and impulse

$D_{selected}$  pre-selected damage level

$e_n$  location of  $F_n$  with respect to point  $O_I$

$e_u$  location of  $F_u$  with respect to point  $O_I$

$e_v$  location of  $F_v$  with respect to point  $O_I$

$E$  Young's Modulus

point  $E$  location of intersection of present ground plane with past highest ground plane

point  $\hat{E}$  denotes the highest compressive displacement experienced at current location of point  $E$ , and since point  $E$  is the intersection of the past highest ground plane, point  $\hat{E}$  is equal to point  $E$

$f_E$  normal force per unit length at point  $E$

$f_F$  normal force per unit length at point  $F$

$f_n$  normal force per unit length

$f_P$  normal force per unit length at point  $P$   $\dot{\chi}$  velocity from rigid body movement at point  $D$

$f_s$  shear force per unit length

point  $F$  location of intersection of present ground plane with zero compressive stress plane (plane that has undergone compressive loading and unloading to zero stress)

point $\hat{F}$	denotes the highest compressive displacement experienced at current location of point $F$
$F_n$	normal force from compression at base of wall
$F_s$	shear force from shearing of base at wall slightly above ground plane
$F_u$	reaction force corresponding to corner deformation $u$
$F_v$	reaction force corresponding to corner deformation $v$
$G$	shear modulus
$h_m$	height of monitoring point
$H$	height of the wall
$H_{EXP}^d$	heat of detonation of the explosive in question
$H_{TNT}^d$	heat of detonation of TNT
$I$	specific impulse
$I_{cg}$	rotational second moment of area about the centre of gravity per unit length
$I_{crit}$	critical impulse
$I_{crit}$	critical impulse required to rotate Rigid-Body Rotation model of wall to critical angle $\alpha$
$I_{Oz}$	effective moment of inertia about axis of rotation $Oz$
$I_{\lambda\alpha}$	impulse required to rotate wall to fraction $\lambda_\alpha$ of critical angle $\alpha$
$I_{\lambda\alpha}$	impulse required to rotate wall to fraction $\lambda_\alpha$ of critical angle $\alpha$

$k$	distributed spring constant for unloading or reloading which relates pressure at the base to displacement of the $cg$ through unloading or reloading according to bulk modulus $K$
$k_D$	cohesive parameter for Drucker-Prager yield relationship
$k_v$	distributed spring constant for new loading which relates pressure at the base to displacement of the $cg$ through the EOS slope $K_v$
$K$	bulk modulus
$KE$	kinetic energy
$K_L$	load constant in Biggs SDOF notation
$K_M$	mass constant in Biggs SDOF notation
$K_v$	slope of Equation of State which relates pressure to volumetric strain
$L_c$	length of each HB unit
$m$	mass per unit length
MC	moisture content
$M_{res}$	resisting moment
$n$	the spring displacement in the vertical direction
$n_E$	normal spring displacement at point $E$
$n_F$	normal spring displacement at point $F$
$n_p$	normal spring displacements at point $P$
$n_{max}$	the maximum experienced spring displacement in the vertical direction at a given point

$n_0$	the spring displacement in the vertical direction at a given point that has displaced to a maximum at that point and has since been unloaded to the extent where zero stress occurs
$n_1$	input constant for simplified Johnson-Cook material model
$N$	propagation velocity
point $O_1$	location of the corner in its fixed position in Rigid-Body Hybrid model
$Oz$	axis of rotation for Rigid-Body Rotation model
$p_b$	pressure at the base of the wall
$p_{step}$	ideal step pressure
$p_{stepcrit}$	critical ideal step pressure
$p(t)$	applied time history of blast pressure
$P$	peak pressure
point $P$	uncompressed position of corner
$PE$	potential energy
$q(r,t)$	spring displacement in direction parallel with height of wall at any time, denoted by function of $r$ for position along coordinate $r$
$q_{max}(r)$	maximum experienced spring displacement in direction parallel with height of wall, denoted by function of $r$ for position along coordinate $r$
$r$	coordinate for distance from point $P$ along rotated base of wall in thickness direction
$\hat{r}$	adjusted $r$ used in interpolation formula based on $\theta$
$r_C$	distance along $r$ coordinate to point $C$

$r_E$	distance along $r$ coordinate to point $E$
$r_{i-1}$	value of $r$ at the $i$ -th minus one discretization
$r_i$	value of $r$ at the $i$ -th discretization
$R$	distance from the axis of rotation $Oz$ to the location of the centre of gravity
$\hat{R}$	the distance from point $D$ to the $cg$
$RHS_u$	right-hand-side of horizontal equation of motion for Rigid-Body Hybrid model
$RHS_v$	right-hand-side of vertical equation of motion for Rigid-Body Hybrid model
$RHS_\theta$	right-hand-side of rotational equation of motion for Rigid-Body Hybrid model
$R(z)$	resistance function
$s$	distance from axis of rotation or the $cg$ axis to centre of infinitesimal element
$s_o$	standoff (or observation distance) from the centre of the explosive source
$t$	time
$t_a$	arrival time of the primary positive shock
$t_d$	positive phase duration
$t_d$	blast load duration
$u$	localized horizontal corner deformation in Rigid-Body Hybrid model whose direction rotates along with the wall rotation $\theta$
$u_{FE}$	displacement in the $x$ - direction in finite element model
$u_m$	horizontal displacement–time history at a monitoring point
$u_{ml}$	horizontal displacement–time histories of the lower monitoring point
$u_{mu}$	horizontal displacement–time histories of the upper monitoring point



$U$	centre of gravity horizontal displacement
$\dot{U}$	horizontal velocity of the $cg$
$v$	localized vertical corner deformation in Rigid-Body Hybrid model whose direction rotates along with the wall rotation $\theta$
$v_{FE}$	displacement in the $y$ - direction in finite element model
$v_m$	vertical displacement–time history at a monitoring point
$v_{ml}$	vertical displacement–time history of the lower monitoring point
$v_{mu}$	vertical displacement–time history of the upper monitoring point
$V$	centre of gravity vertical displacement
$\dot{V}$	vertical velocity of the $cg$
$\bar{V}$	volume per unit length of wall
$W$	energy or mass of the explosive
$w$	generalized width of the wall, taken as unfilled width
$w_a$	unfilled width of soil-filled wall
$w_b$	filled width at location of bulge maximum of soil-filled wall
$w_{FE}$	displacement $z$ - direction in finite element model
$W_E$	equivalent weight of TNT for the explosive
$W_{EXP}$	actual weight of the explosive in question
$\bar{x}$	horizontal distance from $cg$ to point $O_I$
$x_L(z)$	location of the wall edge on the left-hand side
$x_R(z)$	location of the wall edge on the right-hand side
$\bar{y}$	vertical distance from $cg$ to point $O_I$

$z$	applied displacement
$z_{\max}$	selected maximum allowable deflection
$Z$	scaled distance
$\alpha$	angle between the line connecting axis $Oz$ and the cg, which is also the critical rotation angle in Rigid-Body Rotation model
$\alpha_D$	slope parameter for Drucker-Prager yield relationship
$\beta$	decay coefficient depending on the dimensionless scale distance from the centre of the charge to the gauge location
$\Delta s$	change in length of bottom retractable displacement gauge cables
$\delta_{tot}$	total displacement
$\varepsilon_A$	axial strain
$\varepsilon_b$	strain at the base of the wall
$\varepsilon_v$	volumetric strain
$\Theta$	relative volume deformation, volumetric strain, or dilation
$\theta$	time history of rotation
$\dot{\theta}$	rotational velocity
$\lambda$ ,	as consequence of linear spring compressibility with linear unloading and re-loading, is a ratio of $n_o$ to $n_{max}$ , which is ratio of displacement where zero stress is achieved, (i.e. $\lambda=1$ signifies perfectly plastic behaviour where spring unloading modulus $k$ is infinitely high, while $\lambda=0$ signifies elastic behaviour, where unloading modulus is equal to $k_v$ )
$\lambda_l$	fraction of critical overturning impulse

$\lambda_\alpha$	fraction of the critical angle $\alpha$ in Rigid-Body Rotation model
$\mu$	coefficient of friction between bottom of wall and the ground
$\nu$	Poisson's ratio
$\rho$	mass density
$\rho_b$	density at the base of the wall
$\rho_s$	density of steel
$\rho_{wet}$	from wet density
$\sigma$	pressure or stress
$\sigma_A$	axial stress
$\sigma_h$	confining pressure
$\sigma_m$	mean stress
$\sigma_{VM}$	Von Mises stress
$\sigma_Y$	yield stress
$\sigma_y$	flow stress in simplified Johnson-Cook material model
$\tau$	shear stress
$\tau'$	effective shear stress
$\phi$	angle of friction of the soil
$\phi'$	effective angle of friction of the soil
$\psi(x)$	shape function

# List of Appendices

Appendix A. Detailed Description of the Formation of a Blast Wave in Air

Appendix B. Sachs Scaling

Appendix C. Empirical Comparison of Spherical and Hemispherical Charge Performance

Appendix D. Blast Clearing

Appendix E. Description of Mach Stem and Performance

Appendix F. Detailed Derivation of Impulse-Dominated Solution

Appendix G. Detailed Derivation of Pressure-Dominated Solution

Appendix H. Effect of Including Geotextile in FE Model

Appendix I. Analytical Solution for Locating Points  $E$  and  $F$

Appendix J. Calculation of Change in c.g. Location with Local Shear Deformation

Appendix K. Further Blast Loading Details and CFD

# Chapter 1

## Introduction

The need for military protective structures has existed since the origin of war to provide a defensive position. Above ground protective structures are required in many cases because they provide the ability to maintain a protected but offensive position. In addition, an above ground structure may be the only alternative in comparison to a buried structure in a case where practical construction difficulties are encountered, such as rocky ground or ground with a shallow water table.

Historically above ground protective structures have been permanent structures, taking the form of stone forts or castles. Before the 1990s, many above ground protective structures were constructed using reinforced concrete or gabion baskets filled with stones. However modern warfare has presented the need to rapidly construct robust above-ground protective structures while minimizing effort, shipping weights for materials, and construction machinery. In areas where large stones are not available, or lack of curing time prevents construction of reinforced concrete structures, the only alternative may be the use of sandbags and timber framed structures. Although sandbags are lightweight to ship and do not require substantial machinery for use for construction, they are laborious

to fill and place to form walls, and lack durability and robustness against blast loads. The military began using the HESCO Bastion (HB) concertainers® (cubical units) for constructing above ground military protective structures, as they were easier to work with, required less labour, and offered more protection and durability compared to sandbags.

HESCO Bastion concertainers® (HESCO Bastion [1]) were introduced in 1991 and were originally designed for civil engineering applications such as retaining walls, flood and shore-line protection. They were first used by the US military in the Gulf war in the early 1990s and are widely used today. Since then, several other products have originated that are similar to HB concertainers, (Instomat [2], Dynawall [3], etc.). These HB concertainers, details in Section 2.1, are prefabricated units made of galvanized steel weld mesh arranged in cubical shapes, lined with non-woven polypropylene geotextile, as shown in Figure 1.1. The units are placed in the desired geometrical configuration and filled with soil to form walls and structures for civil engineering applications.



**Figure 1.1 HB concertainer® used to construct a protective structure.**

Expedient assessment of the protective capability of HB walls and structures from specified blast loadings is important for military engineers so that they can formulate sufficient protective designs and security protocols. However, there only appears to be limited stud-

ies available concerning development of computational models for HB units subjected to blast loading, apart from a paper presented by Pope et al. [4] in which the LS-Dyna finite element (FE) code was used to construct a model of a HB wall, calculate blast loading response, and iteratively calculate a pressure-impulse curve.

The preferred methodology for expedient structural response calculations by military engineers is in the form of pressure-impulse or  $P-I$  curves, which will be presented in detail in Subsection 2.4.2. These  $P-I$  curves are very useful in blast resistant design, as they illustrate what combinations of blast loadings in terms of peak pressures  $P$  and impulses  $I$  can be sustained for a selected defined level of damage. The calculation of a  $P-I$  curve is computationally expensive, as every single point within a  $P-I$  curve often requires several iterations to solve. Furthermore, a single  $P-I$  curve is typically only valid for a specific component sizes, dimension, and material properties. Thus separate  $P-I$  curves must be calculated for each unique configuration of material properties and dimensions. The analysis using an FE model of an HB wall typically can take several hours or days to calculate, which is not sufficient to provide expedient assessments for a number of different possible scenarios and different wall configurations. Therefore an efficient semi-analytical model is required to enable calculation of  $P-I$  curves efficiently.

## 1.1 Objectives

The aims of the thesis are:

1. To study the response of HB walls both experimentally and numerically, and

2. To develop an efficient semi-analytical model to predict 2-*D* planar response from blast loading that is reasonably accurate, and that can be used to efficiently calculate a *P–I* curve.

## 1.2 Scope

The response of HB units is complex and not all possible wall configurations and soil-fill conditions can be covered. In view of the absence of previous analytical models, an analytical model for 2-*D* planar response is a substantial contribution to the development of robust 3-*D* analytical models for modeling the response of HB walls within protective structures. Therefore main focus of this thesis is the development of a validated 2-*D* planar hybrid rigid-body rotation model for calculating the response of HB walls subjected to far-field blast loading, suitable for expediently calculating a *P–I* curve. Therefore the thesis will have the following scope:

1. Only free-standing 2-*D* planar response of the walls will be considered for development of the analytical models. Axial loading from possible protective structure configurations with supported overhead roofs will not be considered.
2. Straight free-standing five column HB walls subjected to substantially uniform blast loading will be considered for the experiments to approximate 2-*D* planar response. Only a single column HB unit with uniform loading and appropriate planar boundary conditions will be considered in the FE model.
3. Only response from far-field blast loading will be considered.



4. Although this study may be applicable to other makes of soil-filled welded wire mesh geotextile-lined cubical baskets, only selected sizes pertinent to common sizes of HB units will be considered.
5. The experiments conducted will only be using DRDC Suffield Fuel-air site silty-sand as fill for the HB units. The soil-fill is compacted by foot at every 30 cm lift of soil.
6. The effect of the geotextile liner in the FE model and analytical models will be omitted from this study. This decision results from pre-study FE model calculations showing its effects on the far-field blast loaded response to be negligible, while in addition, substantially increasing computational time.

### 1.3 Overview of Thesis

The thesis is composed of seven chapters. Following the introductory chapter, Chapter 2 will provide a detailed explanation of what HB units are and how walls and structures are constructed using them. A review of selected topics within the field of blast loading pertinent to the study will also be conducted. Additionally, an introduction to structural response to blast loading will be presented, including single-degree-of-freedom (SDOF) approximations, impulsive and pressure-dominated asymptotic solutions, as well as a detailed explanation of what  $P-I$  curves are and how they are typically calculated. Chapter 3 will present the details of the experiment setup and instrumentation used. The soils tests used to characterize the mechanical properties of the soil-fill will also be covered. The details concerning the development of the FE model will be covered in Chapter 4. Two

analytical models for planar response of HB walls will be derived in Chapter 5: the Rigid-Body rotation model and the Rigid-Body Hybrid model. The latter combines rigid-body behaviour with a model for calculating localized deformation at the base of the wall. Chapter 6 will be composed of four sections which will discuss the following:

1. Results of full-scale experiments conducted on HB walls subjected to blast loading.
2. FE model results and validation with experiment results.
3. Analytical model results and comparison with experiment and FE model results.
4. As a further validation of the analytical model, comparison of  $P-I$  curves generated using the analytical models and the FE model for different wall sizes.

Chapter 7 will present the conclusions and recommendations for future work within the realm of this study.

## Chapter 2

# Phenomenology and Literature Review

This section will focus on providing a qualitative description of soil-filled units and a literature review of studies applicable to deriving an analytical model for this thesis. In order to appreciate the findings of this research, an understanding of certain terminologies and the nature of blast loading and structural response must be reached. The remainder of this chapter will focus on providing the basic knowledge needed to comprehend this study by presenting necessary background information covering pertinent issues regarding blast loading, response of structures, and pressure-impulse curves.

### 2.1 Description of HB units

A soil-filled unit such as the HESCO Bastion (HB) concertainers® is a prefabricated unit which is made of galvanized steel weld mesh lined with non-woven polypropylene geotextile (<http://hescobastion.com>, [1]), as shown in Figure 2.1 (a). The HB unit can be used in many civil applications, e.g. shoreline protection, retaining walls, etc. HB structures have also been extensively used for expeditionary military structures since the Gulf war in the early 1990s. The units come in a variety of sizes and are collapsed for efficient

transport prior to assembling in theatre, Figure 2.1 (a). The most common sizes used in protective structures are the Mil 1, Mil 2, and Mil 3 units. These specific names will be fully explained in Chapter 3. Fill materials from any particular area of operation can be used when assembling. The convenience during assembling, along with the ability to easily construct well-formed walls contribute to their popularity.



**Figure 2.1 Hesco Bastion Concertainer units: (a) folded Mil 3 units; (b), extended Mil 2 units; and (c), view of inside of unit and geotextile flaps of Mil 2 units.**

To form a structure, the strings of cells are unfolded in the desired wall configuration as shown in Figure 2.1 (b). Geotextile lines the inside of the cells, preventing soil-fill from draining through the welded wire mesh spacing. Extended flaps fold underneath, as shown in Figure 2.1 (c), to prevent soil from draining from the lower edges.



**Figure 2.2 Stages of HB construction: (a) unfolded Mil 1 units aligned in desired configuration and filled with soil; (b), compaction of soil every 30 cm lift.**

Once the cells are unfolded, they are filled with local soil, (Figure 2.2 (a)) and the soil is compacted by foot, shown in Figure 2.2 (b), approximately every 30 cm lift of soil. Simple walls or fully encapsulating structures can be constructed. Note that when the cells are filled, the weld mesh side walls bulge outwards due to the lateral pressure from the soil being compacted, as shown from Figure 2.3 (a). Units can also be stacked on top of one another using custom clips which provide some connection strength between the upper and lower units. If beam-like supporting elements, such as steel profile sheeting, are placed across the top of the structure, additional HB units can be put on top of the sheeting to provide a substantial roof, as shown in Figure 2.3 (b).



(a)



(b)

**Figure 2.3 Final constructed forms: (a) simple wall; (b), fully encapsulated structure with sheet pile roof.**

The structural strength of the HB walls results from filling the units with soil. The soil-fill gives substantial mass, while wire and geotextile provide confinement for the soil-fill, enabling it to sustain higher levels of shear resistance when loaded, as well as directly contributing to the strength and the stiffness of the unit to a limited extent. The ability of the wall to stand and resist overturning is due to gravity and the orthogonal shape, and no

anchoring exists to provide any cantilever behaviour. Quantitative details such as the diameter of the wire mesh and spacing will be further described in Chapter 3.

## 2.2 Blast loading phenomenology

### 2.2.1 Stress waves and shock waves

A stress wave or pressure wave is a disturbance that propagates through a continuous medium. For a stress wave to propagate, the medium must exhibit resistance under compressive and/or tensile force, and possesses inertia. Any time-varying stress applied to such a material will cause a stress wave that will propagate.

The general expression for wave speed in a material, derived through continuity of momentum, is given in Henrych [5] as

$$N = \sqrt{\frac{d\sigma}{d\rho}} = \sqrt{\frac{1}{\rho} \frac{d\sigma}{d\Theta}}, \quad (2.1)$$

where  $N$  is the propagation velocity,  $\rho$  is the mass density of the material,  $\sigma$  is the pressure or stress, and  $\Theta$  is the relative volume deformation, volumetric strain, or dilation. The wave speed depends on the slope of the stress-strain relationship at a given

stress or pressure in Figure 2.4 (a), which corresponds to the  $\frac{d\sigma}{d\Theta}$  term in Eq. (2.1). A

shock wave is formed in a material when stresses are high enough in magnitude to cause material stiffening resulting in increases in propagation velocity. Parts of the wave at higher stresses propagate more quickly and catch up to the wave front, as shown in Figure 2.4 (b). This is the required condition for a stable shock wave to occur. The wave

front continues steepen until it approaches a vertical front. If the wave is externally disturbed, it will shock up again and resume its steep front.

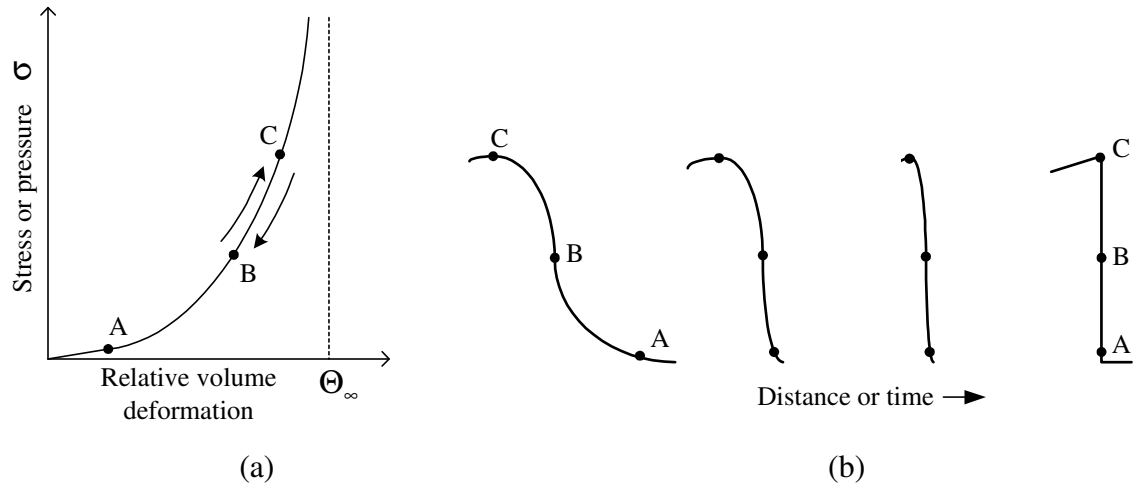


**Figure 2.4 Shock wave development: (a) pressure and relative volume deformation relationship for liquids and gases, (modified from Henrych [5]), (b) formation of a shock front with distance or time, (taken from Cooper [6])**

### 2.2.2 Detonation of explosives

Detonation can be described as a highly exothermic oxidizing reaction. A necessary characteristic of a chemical explosive is that its explosion energy must equal or exceed that amount of energy necessary for activating the explosion reaction in adjacent material (Kinney and Graham [7]). Detonation in an explosive can be initiated by mechanical shock, temperature, electrical shorting, or even intense light. Detonation initiation by a shock wave requires a critical energy fluence that is specific to the particular explosive (Cooper [6]). Once initiated, the energy released from the reaction increases the pressure, temperature and density causing a detonation wave to accelerate away from the initiation point. The propagation of the detonation wave reaction front, under ideal conditions, is

continuously supported by the energy released within the reaction and the high pressures and temperatures it causes. A comprehensive overview of detonation theory is presented in the book by Fickett and Davis [8].

### 2.2.3 Formation of a blast wave in air

A shock wave in air forms as a result of the rapid expansion of high-pressure detonation product gases. A pressure wave is emitted, and the profile of the wave depends on the velocity-time history of the interface between the detonation product gases and the surrounding air. Due to the high velocities at this interface, the pressure wave emitted as a function of time or distance is of a high enough magnitude that it will ‘shock up’, as shown in Figure 2.5.

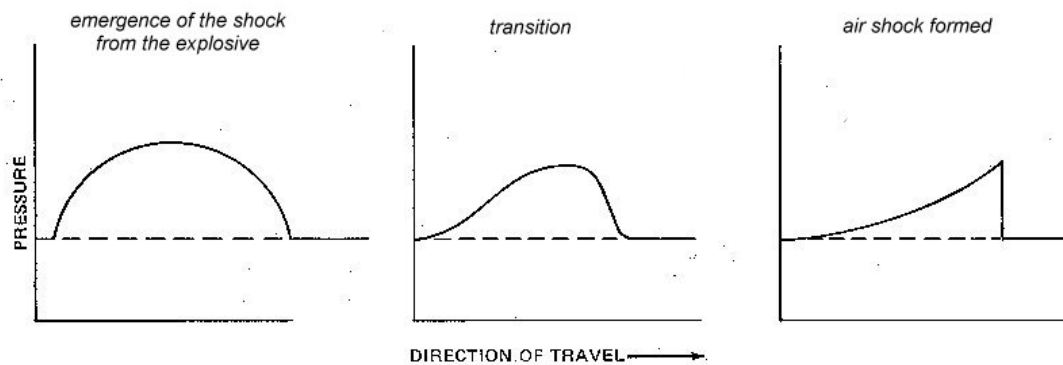


Figure 2.5 Formation of a shock wave in air (Source: Kinney and Graham [7])

However this explanation is highly idealized, as the process of emitting the pressure wave and the shock up occur simultaneously. The detonation product gases also over expand and substantial negative gauge pressures are created. This causes the detonation gas products to retract inward, creating a rarefaction wave behind the primary shock wave.



The subsequent implosion of the detonation gas products causes a secondary shock wave which follows the negative phase and is of a much lesser magnitude than the primary shock wave. A more detailed description of the formation of a blast wave in air from a high explosive is presented in Appendix A.

#### 2.2.4 Blast wave profiles and empirical curve fits

Blast waves outside of the range of interaction of detonation product gases show a characteristic sharp front followed by a decay and negative phase. Figures 2.6 (a) and (b) are examples of idealized blast wave profiles.

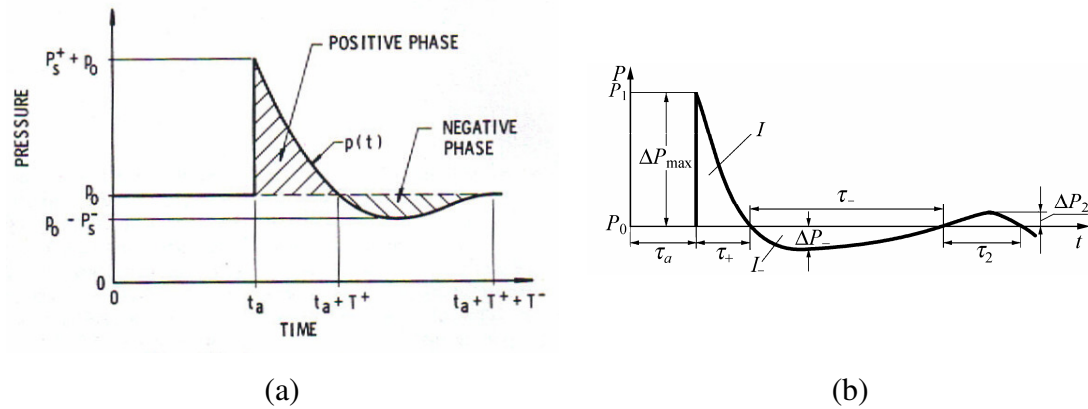


**Figure 2.6 Idealized pressure time histories** Sources: (a) Baker [9] and (b) Gelfand [10]

The time of arrival,  $t_a$ , denotes the arrival time of the primary positive shock. At the time of arrival, the pressure is assumed to jump virtually instantaneously from ambient pressure to peak positive pressure. The peak pressure is followed by a decay in pressure, which intersects ambient pressure at a time  $t_a + t_d$ , where  $t_d$  is the positive phase duration. The impulse is the integral or area underneath the pressure–time history. Note that

the term ‘impulse’ is loosely used, and the more precise term is the specific impulse, as it refers to the impulse per unit area. Typically only the positive phase impulse is considered. The blast wave exhibits a negative phase caused by the contraction of the detonation gas products after they over-expand. Some authors also include the secondary shock in their description of an idealized blast wave, as shown in Figure 2.6 (b).

Use of an analytical curve fit enables one to summarize complex time histories of pressure recorded experimentally with only a few parameters, which later can be transcribed back into an idealized pressure-time history for calculation purposes. The simplest curve fit is a triangular pulse load, which requires two parameters. The mathematical representation of such curve is

$$p(t) = \begin{cases} 0 & t < t_a \\ P \left( 1 - \frac{t - t_a}{t_d} \right) & t_a \leq t \leq (t_a + t_d) \\ 0 & t > (t_a + t_d) \end{cases}, \quad (2.2)$$

where  $P$  is the reflected peak pressure. The time duration for this curve fit normally is not set equal to the time duration of the positive phase of the experimental trace, but is typically assumed as a value that will enable the positive phase impulse to match that of the experimental trace. Another two parameter curve fit that is widely used is in the form of an exponentially decaying wave, represented by the following mathematical description.

$$p(t) = \begin{cases} 0 & t < t_a \\ P e^{-\frac{P(t-t_a)}{I}} & t \geq t_a \end{cases}, \quad (2.3)$$

where  $I$  is the specific impulse. This curve fit is convenient for analytical solutions and is in most cases a better description of a blast wave in comparison with the triangular fit. Figure 2.7 shows exponential curve fits to a sample pressure trace and the resulting cumulative impulse traces.

Increasing accuracy in fitting experimental traces can be attained with more parameters. Past experimental investigations (U.S. Department of the Army [11] and Watson [12]) have shown that an increasingly accurate simulation of blast loading can be expressed by a Friedlander curve fit, which involves three parameters, as:

$$p(t) = \begin{cases} 0 & t < t_a \\ P \left( 1 - \frac{t - t_a}{t_d} \right) e^{-\frac{\beta(t - t_a)}{t_d}} & t_a \leq t \leq (t_a + t_d) \\ 0 & t > (t_a + t_d) \end{cases}, \quad (2.4)$$

where  $\beta$  is a decay coefficient depending on the dimensionless scale distance from the centre of the charge to the gauge location.

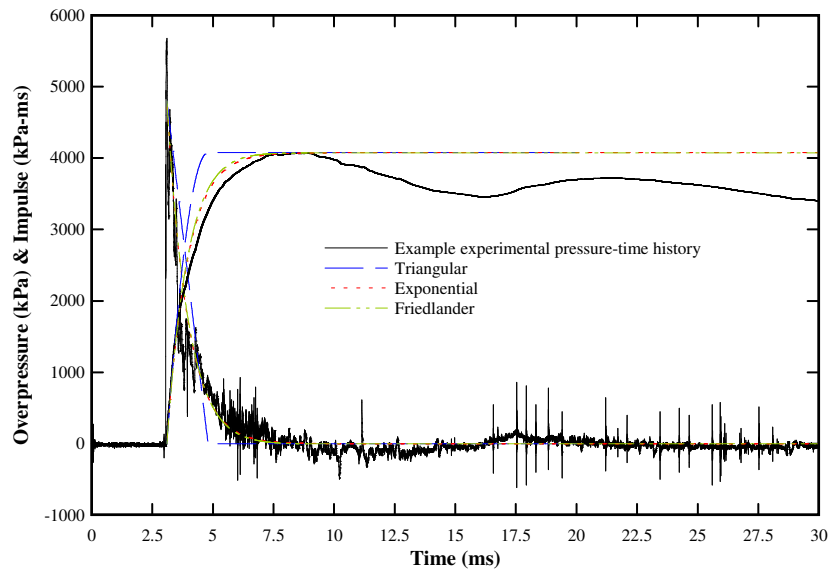


**Figure 2.7 Comparison of empirical curve fits for an experimental blast wave pressure-time history.**

Note that the preceding analytical curve fits are only intended for the positive phase. There are limited proposed analytical curve fits for the negative phase. Although the gauge pressures associated with the negative phase are typically very low compared with the positive phase, the effect on the cumulative impulse from the negative phase can be significant. This can affect structures whose response is sensitive to impulse. The relative proportion of the negative phase impulse decreases however with strong blast waves at smaller scaled distances (see Subsection 2.2.5). However the negative phase is often ignored for the reason that it is difficult to measure and establish consistent experimental data. This is because the positive phase pressures which occur at the beginning of a blast wave are much greater in magnitude than the negative phase pressures which follow, creating difficulties for precise measurement of the negative phase. In design practice, the negative phase is omitted and this leads to a conservative result due to the fact that the net loading is overstated.

### 2.2.5 Blast scaling

Hopkinson-Cranz scaling was first proposed by B. Hopkinson [13] in 1915. The law states that self-similar blast waves are produced at identical scaled distances when two charges of the same geometry and explosive type are detonated in the same atmosphere. The scaled distance is given by

$$Z = \frac{s_o}{W^{1/3}}, \quad (2.5)$$

where  $s_o$  is the standoff (or observation distance) from the centre of the explosive source and  $W$  is the energy or mass of the explosive. Figure 2.8 shows a schematic comparing

the pressure-time histories arising from two charge size standoff scenarios. Since  $W^{1/3}$  is directly proportional to the charge diameter  $d$ , both scenarios possess the same scaled distance, and both produce self similar blast waves that can be scaled with one another.

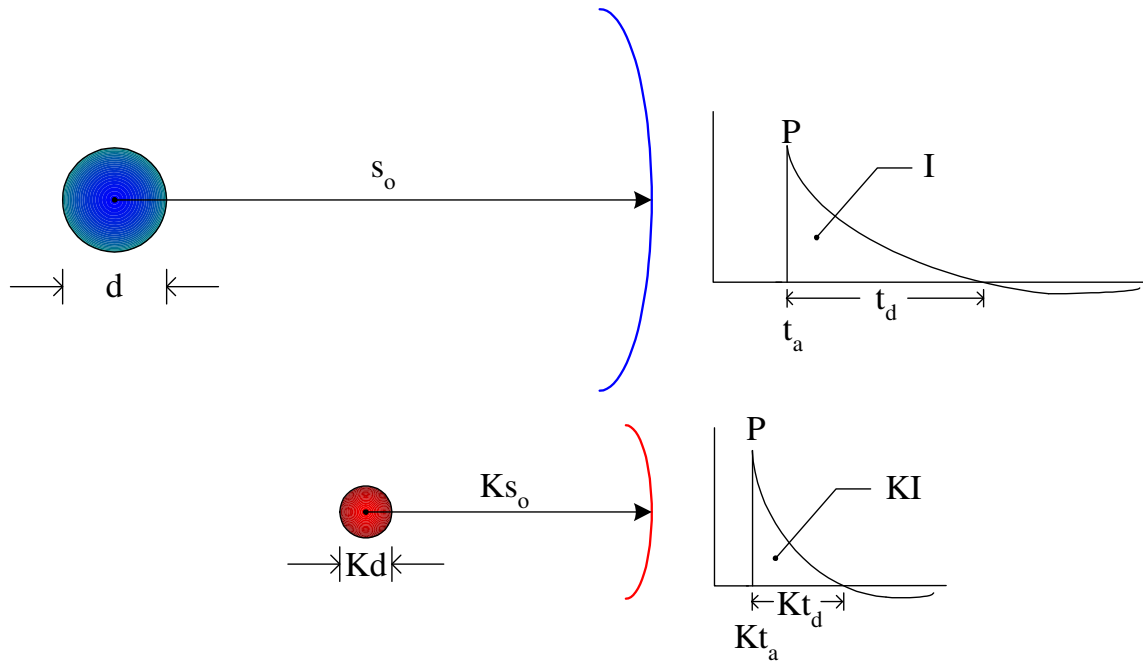


**Figure 2.8** Hopkins-Cranz scaling (Source: Baker [9])

Appendix B presents the extension of this scaling law to consider differing atmospheric conditions formulated by Sachs [14] in 1944.

### 2.2.6 Empirical performance of high explosives

The majority of empirical data generated from the start of when high explosives were first studied has been for TNT. Due to the large quantity of empirical studies using this explosive compared with other explosives, TNT has been adopted as a benchmark high explosive. A hemispherical configuration is a half-space approximation, shown in Figure

2.9 (b), that was historically used to help relate established spherical performance to hemispherical performance. Appendix C provides further details concerning this approximation.

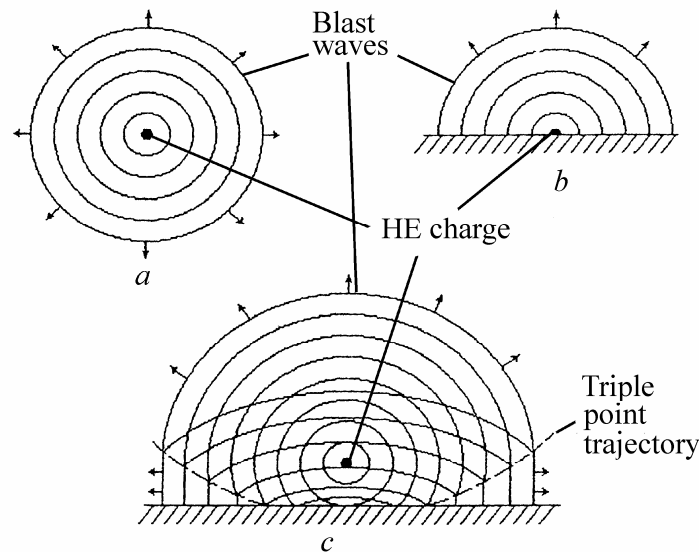


**Figure 2.9 Charge configurations: a – spherical; b – hemispherical; c – height of burst (Source: Gel-fand [10])**

Kingery and Bulmash [15], through compiling extensive experimental data for TNT, derived empirical equations consisting of polynomial equations in logarithmic space as a function of scaled distance for the performance of both spherically and hemispherically configured TNT at sea level. Empirical performance for hemispherically configured TNT is presented graphically in Figure 2.10.

Note that the subscript ‘r’ represents the normally reflected parameters and subscript ‘so’ represents the incident parameters. The incident parameters are obtained through gauges that allow the blast wave to pass by relatively unaffected and do not cause any substantial stagnation in particle velocities. To accomplish this, the gauge is mounted on a surface

that is parallel to the direction of the shock wave propagation and its particle velocity direction.

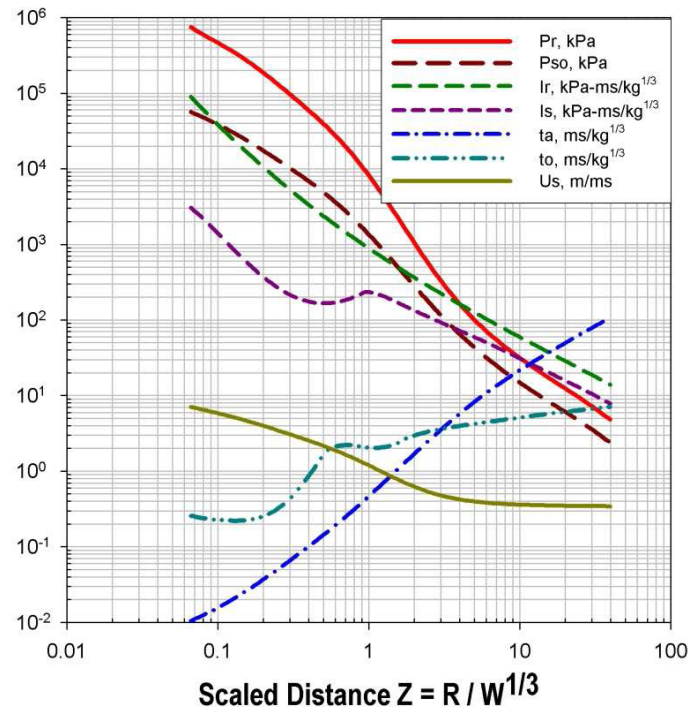


**Figure 2.10 Incident and reflected hemispherical TNT performance as function of hemispherical scaled distance (Source: Remennikov [16])**

The reflected parameters are obtained from a gauge on a surface that is perpendicular or normal to the incoming blast wave, where stagnation in the particle velocity takes place. Thus for a given situation in calculating the loading, one must decide if the loading surface with respect to the blast is best represented as a parallel or perpendicular surface to select whether the incident or reflected parameters best represent the loading case. These are idealized cases, and one should also consider the possibility of blast clearing, refraction, and Mach stem effects, which are not considered in the above graph, which occur

for all high explosives. Additional information about blast clearing is presented in Appendix D, while an explanation of Mach stem formation and performance increases are presented in the Appendix E. Also note that the reflected impulse is assumed to take place off an infinitely large normal surface, (or surface large enough that blast clearing effects need not be considered).

Due to complexities in the height of burst configuration, (formation of Mach stem and additional height of burst parameter), limited information is available to predict performance of height of burst scenarios, although TM5-1300 (U.S. Department of the Army Technical Manual [11]) does contain approximate methodologies for accounting for increases in incident pressures arising from the Mach stem produced in height of burst scenarios. Note that if the height of burst is small compared with the standoff distance, hemispherical performance can be assumed. A comprehensive study of when this assumption is reasonably accurate is not available in references however, and assumption of a hemispherical burst performance in a height of burst situation will understate performance. This is due to the fact that Mach stem formation (which improves performance) only occurs for a HOB scenario and not a hemispherical scenario. In addition, a hemispherical scenario produces more cratering and thus more energy is lost compared with a HOB scenario. In a hemispherical burst scenario, it is estimated that approximately 20 % energy is lost through cratering. As a measure of the fraction of energy imparted due to cratering, ConWep (Hyde [17]) quotes a coupling factor of 0.14 while Henrych [5] quotes 0.22.



### 2.2.7 Equating non-TNT explosives performance to equivalent TNT

To calculate performance of explosives other than TNT, empirically established TNT equivalence factors are often used as an estimate. These factors can be used to relate a charge of a given size and explosive type to an equivalent TNT charge size, enabling one to subsequently use established empirical performance tabulations for TNT to calculate loading for an alternate explosive. The three most common methods of calculating TNT equivalence are by heat of detonation, by pressure, and by impulse. TM5-1300 gives the following equation for equivalence based on heat of detonation:

$$W_E = \frac{H_{EXP}^d}{H_{TNT}^d} W_{EXP} \quad (2.6)$$

where the equivalent weight of TNT for the explosive in question is  $W_E$ , while  $W_{EXP}$  is the actual weight of the explosive in question. The heat of detonation of TNT and the explosive in question are given by  $H_{TNT}^d$  and  $H_{EXP}^d$ , respectively. Equivalence by Pressure or Impulse are also widely used, Hyde [17], where an equivalence factor is determined by taking the ratio of the peak pressure or impulse from the explosive in question with the peak pressure or impulse from the same size of TNT charge at the same standoff. Ratios are calculated for a range of scaled distances and the equivalence factor is taken as the average ratio. A list of TNT equivalences for a variety of explosives can be found in the book by Cooper [6] or within the ConWep software (Hyde [17]).

### 2.2.8 Ground shock

When an explosion occurs at or near the ground surface, ground shock results from energy imparted to the ground by the explosion. Some of this energy is transmitted through the air in the form of air-induced ground shock and some is transmitted to the ground as direct-induced ground shock. Henrych [5] provides an illustration of the wave fronts created by these two phenomena, shown in Figure 2.11.

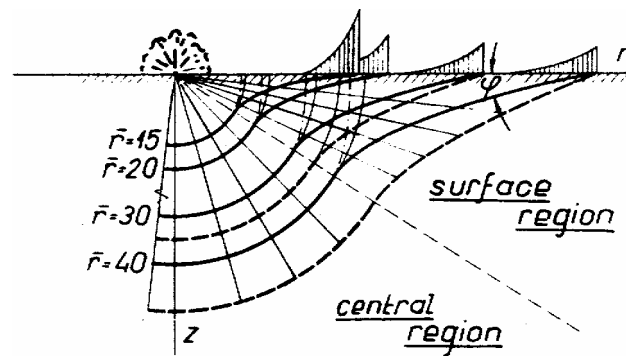


**Figure 2.11** Diagram of the successive positions of air-induced and direct-induced ground shock, (dashed curves: sound-wave front; solid curves: front of the first maxima) (Source: Henrych [5])

Air-induced ground shock results when the air-blast shock compresses the ground surface and sends a stress pulse into the underlying media, producing displacements in the downward direction. Direct-induced ground shock results from explosive energy transmitted directly through the ground. The resulting waves from direct-induced ground shock waves tend to be sinusoidal and are of much longer durations than air-induced ground shock waves. The overall ground movement is the net of the motions caused by the summation of air-induced and direct-induced ground shock waves. At close ranges to the explosive event, the air blast propagates faster than the ground shock, but the air shock eventually slows and the ground shock outruns the air blast.

## 2.3 Structural response to blast

This section provides an introduction to structural response to blast loading, the solutions to single degree of freedom systems, their asymptotic solutions, and the generation of  $P-I$  curves.

### 2.3.1 SDOF systems

In many cases, a structure can be represented by a dynamically equivalent single-degree-of-freedom, (SDOF), system which behaves time wise nearly in the same manner as the actual structure. Although all structures possess many modes of response, one mode usually dominates the response, and this mode can be used to derive an equivalent SDOF system based on equivalent energy. A derivation of a SDOF system for an elastic beam subjected to general dynamic loading can be found in Tedesco [18]. An equivalent SDOF system for a beam, represented by a concentrated mass, and single mass-less spring, and applied force is shown in Figure 2.12.

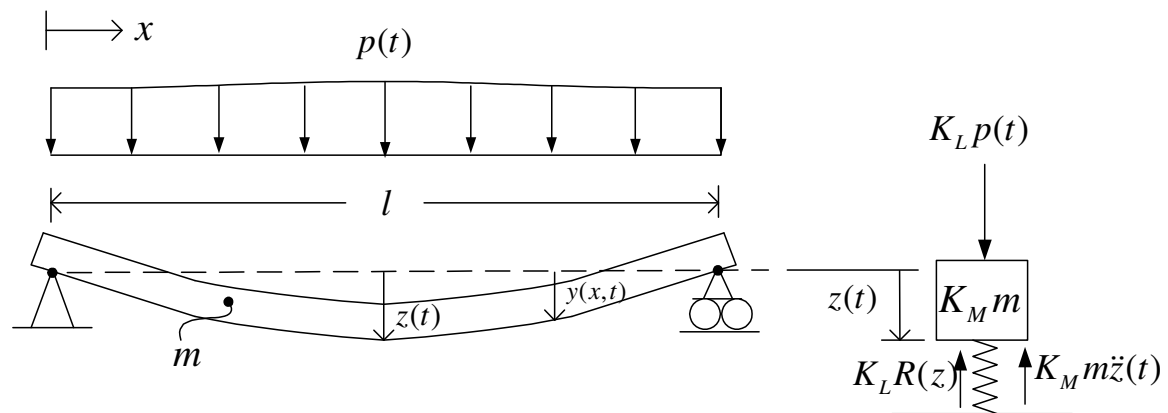


Figure 2.12 Beam under time varying pressure loading and equivalent SDOF system

Note that damping is hardly ever considered in SDOF calculations involving blast, this is because (TM5-1300 [11]):

- a) Damping has very little effect on the first peak of response which is usually the only cycle of response that is of interest
- b) The energy dissipated through plastic deformation is much greater than that dissipated by normal structural damping, and
- c) Ignoring damping is a conservative approach

In many cases concerning blast loading, it is of interest to be able to calculate the response nearing ultimate failure and the assumption of a linear elastic beam may not be valid. The equation of motion for the equivalent SDOF system shown in Figure 2.13, accounting for non-linear resistance to loading, is given by Biggs [19] as

$$K_M m \ddot{z} + K_L R(z) = K_L p(t), \quad (2.7)$$

where  $m$  is the distributed mass per unit length.  $R(z)$  is termed the resistance function and is a function which gives the resistance of a beam in terms of uniformly applied pressure for an applied displacement  $z$ . Constants  $K_M$  and  $K_L$  are calculated based on the shape function,  $\psi(x)$ , that is selected to follow the displaced shape of the beam. The shape function is typically selected based on the static deflection, or for large displacements of a simply supported beam, it is selected based on the formation of a plastic hinge at the centre span. The constants  $K_M$  and  $K_L$  are given respectively as

$$K_M = \int_0^L \psi^2(x) dx, \text{ and} \quad (2.8)$$

$$K_L = \int_0^L \psi(x) dx. \quad (2.9)$$

Idealized cases exist for very short duration loads and very long duration blast loads, which can be solved through energy balance. If the loading is very short compared with the response time of the structure, the majority of the response immediately after the application of loading will be in the form of kinetic energy absorption. The remainder of its response is subsequently governed by its ability to absorb the kinetic energy through strain energy absorption. The peak displacement for this type of loading is independent of the peak pressure applied, and only depends on the impulse. The critical impulse  $I_{crit}$  for this idealized case can be derived as

$$I_{crit} = \sqrt{2 \frac{K_M}{K_L} m \int_0^{z_{max}} R(z) dz}, \quad (2.10)$$

where  $z_{max}$  is the selected maximum allowable deflection. The detailed derivation of this equation is presented in Appendix F. Note that this equation shows that no matter the complexity of the resistance function, the amount of impulse absorption ability is proportional to the square root of the area underneath the resistance function to  $z_{max}$ . Also note that an increase in mass, with no increase in strength properties, leads to an increase in impulse absorption capability that is proportional to the square root of the mass increase. Eq. (2.10) is only valid if impulsive loading is a valid assumption, and the range of validity of this assumption can be found in Baker et al. [20].

For a very long duration blast loading that approaches an ideal step pressure loading another energy balance technique can be applied. The response is only peak pressure de-

pendent, the term peak pressure dominated loading is often referred to. An approximate description is given in Kinney and Graham [7]. This technique is possible because the transient loading can be reduced to a constant loading and  $p(t) = p_{step} = p(z)$  applies. The critical step loading,  $p_{stepcrit}$ , can be derived as the maximum of the cumulative average resistance within the interval of 0 to  $z_{max}$ , i.e.

$$p_{stepcrit} = \text{Max} \left\{ \frac{1}{z} \int_0^z R(z) dz \right\}; \quad 0 \leq z \leq z_{max} . \quad (2.11)$$

The detailed derivation of this equation is presented in Appendix G.

### 2.3.2 $P-I$ curves

Assessing the effect of blast loading on structural components can be achieved by developing a bespoke Pressure-Impulse ( $P-I$ ) or ‘iso-damage’ diagram for a particular structural component. A  $P-I$  curve, shown in Figure 2.13, gives the possible combinations of blast waves capable of causing a selected level of damage, and effectively informs engineers whether a particular blast loading will cause damage above or below the selected damage level. Some examples of damage which could be defined are values of peak deflection, rotation, velocity at a given location, a rupture or any form of collapse which is deemed to cause excessive damage or may pose a hazard to personnel within a structure, etc. If the reflected peak pressure and peak positive impulse from the blast plot above and to the right of the  $P-I$  curve, the component is assumed to have exceeded the selected damage level, and if, on the other hand, the loading plots below the  $P-I$  curve, the component is assumed not to have exceeded the selected damage level. Some examples of

damage are an excessive deflection, rupture or any form of collapse. The extent to which the applied impulse or pressure dominates the structural response depends on the response time of the structure relative to the duration of the applied blast load. Response to relatively short duration loads are dominated by the magnitude of impulse applied while response to relatively long duration loads are dominated by the magnitude of peak pressure. There also exists an intermediate region, however, often termed dynamic (Baker et al. [20]), where the loading contribution of both the impulse and the peak pressure must be considered. These regimes are labelled in the generic  $P$ – $I$  curve produced for a single-degree of freedom linear spring mass oscillator subjected to an exponentially decaying blast load as shown in Figure 2.13. The parameter  $X_{max}$  is the given maximum displacement representing the threshold of damage.

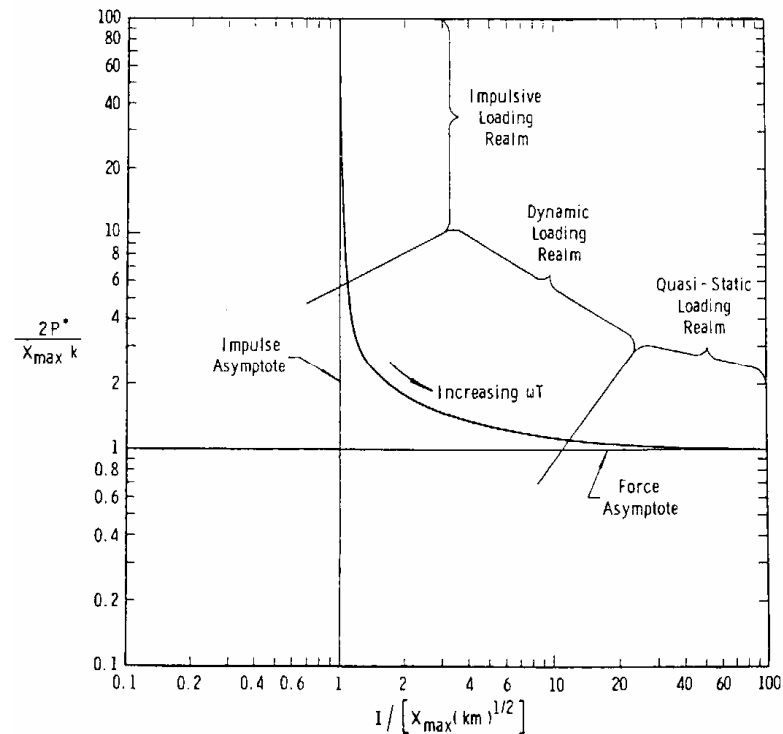


Figure 2.13 Normalized  $P$ – $I$  curve for linear elastic oscillator (Source: Baker et al. [20])

The asymptotes can be located by using the energy balance techniques explained in the previous section, and often  $P$ – $I$  curves are normalized with respect to their asymptotic expressions as in Figure 2.13. Solving for the dynamic regime of the  $P$ – $I$  curve can be tedious.  $P$ – $I$  curves are numerically solved for by iteratively solving the equation

$$D_{result}(P, I) = D_{selected}, \quad (2.12)$$

where  $D_{selected}$  is a pre-selected damage level, (typically a peak displacement), defined by the individual generating the  $P$ – $I$  curve. The function  $D_{result}(P, I)$  is the damage calculated by the underlying computational model used to generate the  $P$ – $I$  curve. The underlying computational model can be any type of model; e.g. single-degree-of-freedom (SDOF), discrete element, finite element, or even blast experiments, which gives a resulting damage when subjected to a blast load of a peak pressure,  $P$ , and peak positive impulse,  $I$ . Note that in assuming a blast loading characterized by these two parameters, one must assume a curve fit to the time-dependent pressure profile. The two most popular curve fits to the time-dependent pressure profile of a blast wave are the triangular and exponential fit, given by Eqs. (2.2) and (2.3), and the  $P$ – $I$  curve location differs slightly in the dynamic regime depending on which curve fit is selected, (Li and Meng [21], and Baker et al. [9]).

To comprehensively generate a  $P$ – $I$  curve using a finite element (FE) model or experiments by iteratively solving Eq. (2.12) for several dozens of points, (for sufficient smoothness), can be prohibitively time consuming and expensive. However, use of a curve fit enables one to calculate an approximate  $P$ – $I$  curve using only a limited number



of points solved using Eq. (2.12). The most popular curve fit form is a hyperbola, given as

$$(P - p_{stepcrit})(I - I_{crit}) = C, \quad (2.13)$$

The parameter  $C$  determines how abrupt the transition region is. Decreasing  $C$  will sharpen the transition and increasing  $C$  will soften the transition in the Dynamic loading realm. Once one or more points in the dynamic regime are generated, in addition to the asymptotes, the parameter  $C$  can be altered to fit these points in the dynamic regime as shown in Figure 2.14

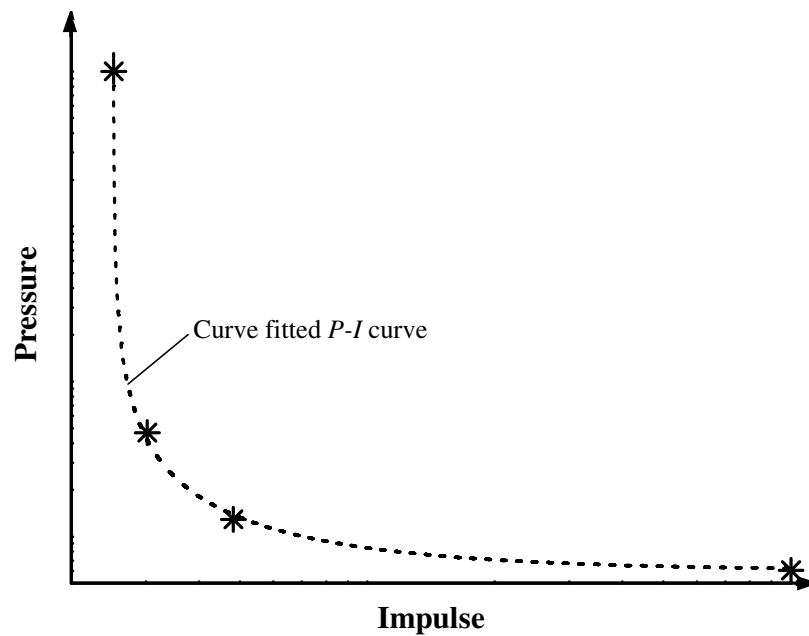


Figure 2.14 Curve-fitted  $P-I$  curve through limited numerically generated points using a hyperbola

Through numerous empirical comparisons of comprehensive numerically solved  $P-I$  curves with hyperbolic curve fits within the Dynamic loading realm, the following empirical equation was proposed by Oswald and Skerhut [22].

$$(P - p_{stepcrit})(I - I_{crit}) = 0.4 \left( \frac{p_{stepcrit}}{2} + \frac{I_{crit}}{2} \right)^{1.5}. \quad (2.14)$$

This hyperbolic equation provides a very good estimation of the location of the  $P-I$  curve in the Dynamic loading realm without using Eq. (2.12), but only using the asymptotic values of  $I_{crit}$  and  $p_{stepcrit}$  as solved in the previous section as input. Additionally, if there are known points solved through Eq. (2.12) in the dynamic regime, the right hand side of this Eq. (2.14) serves as a very good starting guess of parameter  $C$  in Eq. (2.13).

## 2.4 Literature review of Hesco Bastion units

Available literature sources concerning the performance against blast loading of soil-filled HB units is scarce. Prior to the time at the start of this thesis, there appeared to be no studies available in the literature, apart from a paper presented by Pope et al. [4] in which the LS-Dyna finite element (FE) code was used to construct a model of a HB wall. The (FE) model was iteratively used to calculate the location of a Pressure-Impulse ( $P-I$ ) curve for the wall, and calculating approximately a dozen points on the  $P-I$  curve required a substantial computational effort. Scherbatiuk et al. [23] examined reductions in transferred velocity in the thickness direction of a 1-D column of soil from blast, and presented differences in transferred velocity by assuming rigid uncoupled versus coupled loading and deformable soil. The velocity difference for a column of soil through the

thickness of an HB wall from coupled versus uncoupled loading was found to be negligible, establishing that use of uncoupled loading for HB wall response was a reasonable assumption. In conjunction with this thesis, Scherbatiuk et al. [24] derived a rigid-body rotation model, and found reasonable agreement with HB wall experiments, although slightly under predicting response. The rigid-body rotation model offered an expedient way to quickly calculate pressure-impulse curves. Scherbatiuk and Rattanawangcharoen [25] conducted experiments measuring the displacement–time histories at points on the back of HB walls loaded by blast and compared them to those obtained through using a FE model. Good agreement was achieved. Scherbatiuk and Rattanawangcharoen [26] derived a rigid-body hybrid model, incorporating localized compression and shearing at the corner of rotation with a rigid-body model. Very good agreement was achieved in comparison with FE models and experimental displacement–time histories.

Several authors have presented work related to this thesis topic. Zhang and Makris [27] studied rocking response of free-standing blocks under cycloidal pulses of ground displacement. Van Leeuwen [28] presented a mathematical model for calculating overturning dominoes, accounting for both the resistance towards overturning and the impact and effect of friction. Houlsby et al. [29] presented a generalized Winkler model for the behaviour of shallow foundations under cyclic loading. Rose et al. [30] reported on the effectiveness of cantilever walls in attenuating blast waves produced by a range of explosive threats detonated at different distances from a wall. The test program demonstrated that a free standing wall can reduce the last peak pressure behind the wall by 70 % and reduce the blast impulse by 60 %, depending of the type of material, the width, the height

of the wall and the location of the monitoring point. However, in these approaches the assessment of protective level is based on the assumption that the structure could withstand the blast loading, and not much attention was spent on to the investigation of structural response. Several authors have investigated soil modeling under blast loading (Wang et al. [31], Laine and Sandvik [32], Fišerová et al. [33]), which involved deriving soil properties, modelling blast wave propagation in soil using AutoDyn® Computational Fluid Dynamics/ Computational Solid Dynamics software [34].

# Chapter 3

## Experimental Investigation

The first half of this chapter provides the details of the full-scale experiments conducted on HB walls subjected to blast loading. The second half of the chapter focuses on the details of the soil testing and determination of the soil mechanical properties.

### 3.1 HB wall experiments

Seven experiments were conducted on HB walls subjected to blast loading: Trials 1 through 7. All experiments were conducted at DRDC Suffield at the Fuel Air Site, and were undertaken within three different trial series. Trials 1 and 2 were conducted in 2003, Trial 3 in 2004, and the remainder of the trials were conducted in 2006. An overview of the experimental details are presented in Table 3.1 while the following sections present an overview of each of the experimental components.

**Table 3.1 Overview of experiments on HB walls**

<b>Trial</b>	<b>HB Unit (width × depth × height) (mm × mm × mm)</b>	<b>Courses (wall height, m)</b>	<b>Filled Width <math>w_b</math> (m)</b>	<b>Instrumentation</b>
1 (2003)	Mil 3 (975 × 975 × 975)	2 (1.95)	1.2	Before and after photos, single pressure-time measurement, manual filled width measurements
2 (2003)	Mil 3 (975 × 975 × 975)	2 (1.95)	1.2	Same as Trial 1
3 (2004)	Mil 2 (600 × 600 × 600)	2 (1.2 m)	0.74 m	Before and after photos, single pressure-time measurement, laser scanned filled width measurements
4 (2006)	Mil 3 (975 × 975 × 975)	2 (1.95)	1.2	Before and after photos, 3 pressure-time measurements, laser-scanned filled width measurements, and cable displacement–time measurements
5 (2006)	Mil 1 (1050 × 1050 × 1350)	1 (1.35)	1.33	Same as Trial 4
6 (2006)	Mil 3 (975 × 975 × 975)	2 (1.95)	1.2	Same as Trial 4
7 (2006)	Mil 1 (1050 × 1050 × 1350)	1 (1.35)	1.33	Same as Trial 4

### 3.1.1 Experiment setup

The general experiment setup used for the trials is shown in Figure 3.1. For each trial, the blast wave was produced from the detonation of an explosive charge. The details of the charge and distance have been omitted for security reasons. All trials utilized reflected pressure gauges, (one for Trials 1 to 3, three for Trials 4 through 7), mounted on the side of the wall facing the blast. Framework housing five retractable displacement gauges was

used in Trials 4 through 7 to measure displacement–time histories at the points of the wall facing away from the blast as shown.

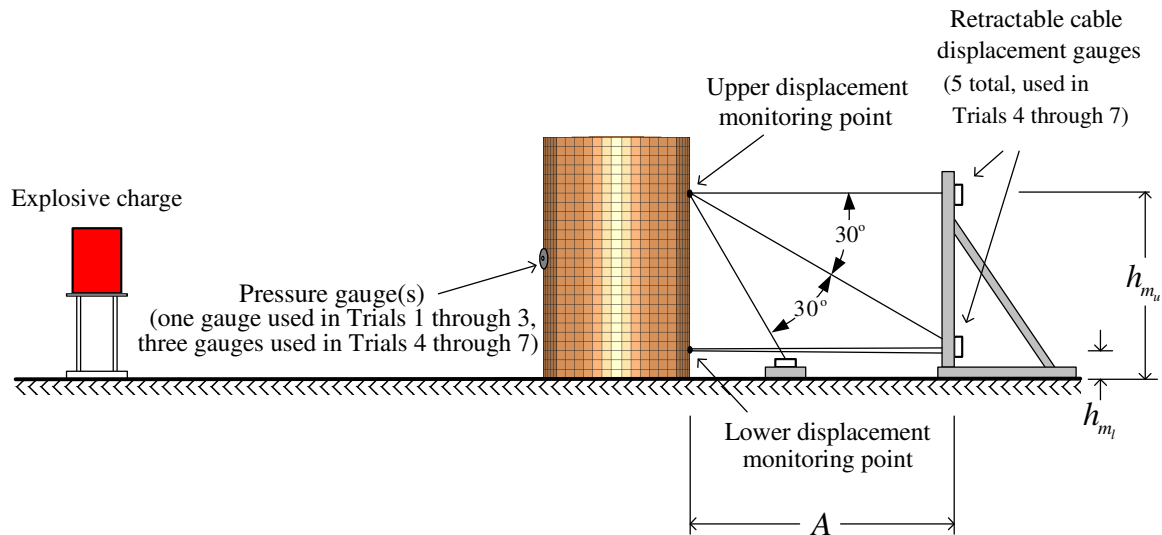


**Figure 3.1 Experiment setup**

### 3.1.2 Wall details

Three different wall configurations were used in the seven trials. Each wall consisted of a simple straight free-standing HB wall with five interconnected columns. Trials 1, 2, 4 and 6 were a Mil 3 two course wall consisting of 975×975×975 mm HB units, as shown in Figure 3.2 (a). Trial 3 was a Mil 2 two course wall consisting of 610×610×610 mm HB units, as shown in Figure 3.2 (b). Trials 5 and 7 were a Mil 1 one course wall consisting of 1050×1050×1350 mm units. For all HB walls tested, the mesh was made of 4 mm diameter Galfan® coated steel wire, spaced at 75 mm both horizontally and vertically. The joints consisted of 4 mm diameter steel wire coiled to approximately 20 mm diameter, which tie the welded wire mesh of adjacent HB units together as shown in Figure 3.3 (a).

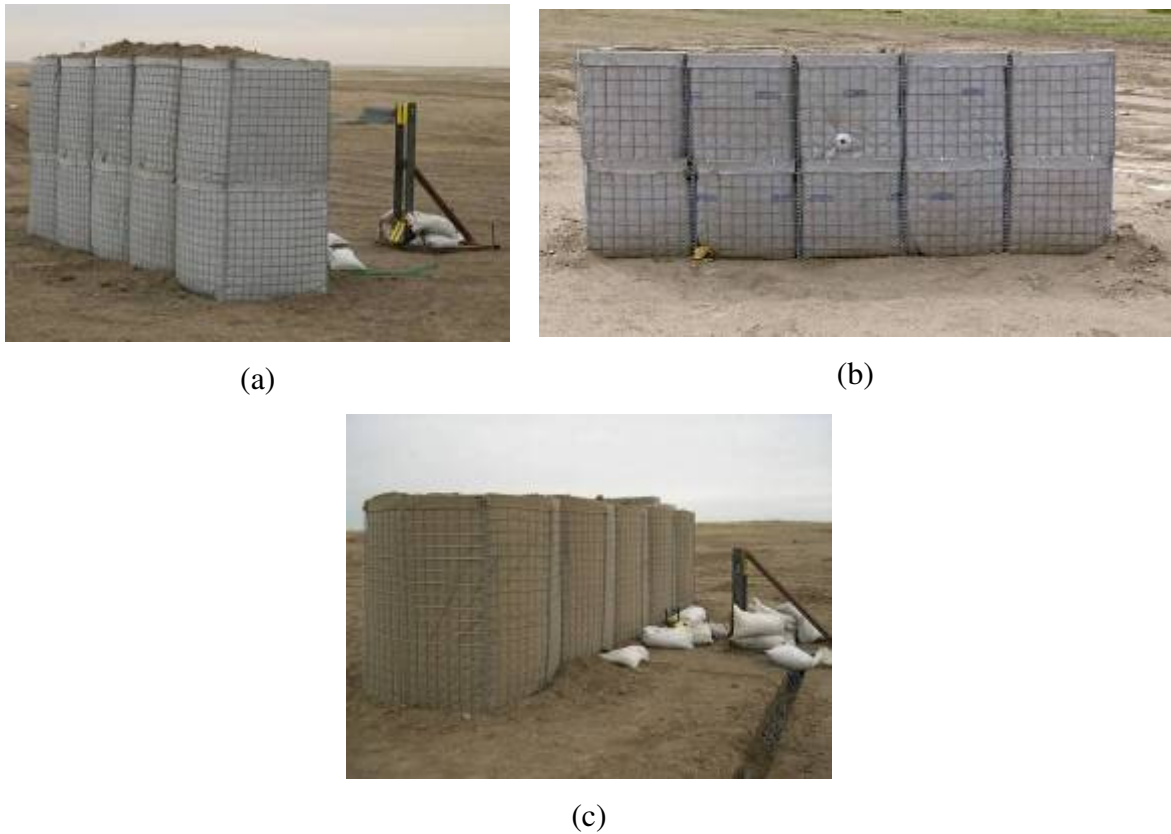


**Figure 3.2 Configurations of HB walls tested: (a) HB Mil 3 two course wall for Trials 1, 2, 4, and 6; (b) HB Mil 2 two course wall for Trial 3; and (c) HB Mil 1 one course wall for Trials 5 and 7.**

The upper and lower layers of the two course walls were connected together using the custom clips supplied with the HB units. The clips consisted of 4 mm diameter wire, attaching the upper and lower course at two points along each cell column, as shown in Figure 3.3 (a). More details regarding the material and wire mesh specifications for HB walls can be found on the manufacturing website, <http://hescobastion.com> [1].

The geotextile in the HB units was 2 mm thick heavy-duty non-woven polypropylene. Additional geotextile which form flaps at the bottom provided a prevention of soil draining from the lower edges, shown in Figure 3.3 (b).





(a) (b) (c)  
**Figure 3.3 Additional details of HB walls: (a) Coiled joint separating HB columns, shown with clips connecting upper and lower course; (b) geotextile flaps preventing soil from draining along bottom wall sides; and (c) bulge at bottom constrained from geotextile flaps.**

Upon filling with soil and compacting, a sizable bulge in the sidewalls occurred, as seen in the walls in Figure 3.2. However the bulge was largely constrained at the bottom due to the geotextile flaps, Figure 3.3 (c). Due to this, it is advised that prior to filling, the flaps be pulled out to relieve this constraint as much as possible, improving the stability of the wall resulting after filling.

### 3.1.3 Construction of walls

All of the tested walls were filled with local silty-sand originally excavated from the site and stockpiled. This fill was moderately well mixed and then compacted by foot for approximately 1 minute at every 0.3 m lift of soil. The soil was not watered during compaction and had an existing moisture content of 7 to 15 %. The experiments took place within two days of the construction of the walls, and negligible precipitation took place in the time between the construction and the testing of the walls. The moisture content of the fill depended on the moisture content of the soil stockpiled, which itself depended on

the precipitation at the given time of year that the respective trials took place. Additional details regarding soil material properties will be presented in a following section.

### 3.1.4 Laser scanning

Laser scanning was employed in Trials 3 through 7 to measure the pre-experiment volume, geometries of the bulges, and pre- and post-experiment wall positions. The additional volume due to the bulges can add as much as 30 % more soil volume, (and mass), over the empty pre-construction volume of the HB units. The type of laser scanner used was a HDS300, which utilized Cyclone® post processing software, both manufactured by Leica Geosystems®, Heerbrugg, Switzerland [35]. Figure 3.4 (a) illustrates a volume measurement conducted using Cyclone® post-processing software. Figure 3.4 (b) contains a cross-section at mid-height of the wall, illustrating the extent of the bulges caused by lateral soil pressure. The extent of the bulged width was surveyed for each column at a number of different heights for each type of wall used, and the average bulged width was calculated and is shown schematically in Figure 3.5 and listed in Table 3.1.

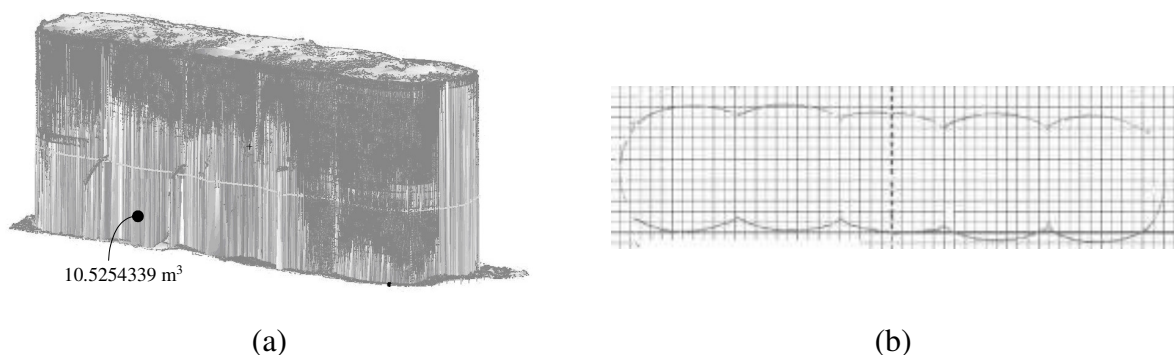


**Figure 3.4 Laser scan volume measurements of Mil 3 HB wall in Trial 3: (a) overall volume and (b) geometry of bulges at mid-height**

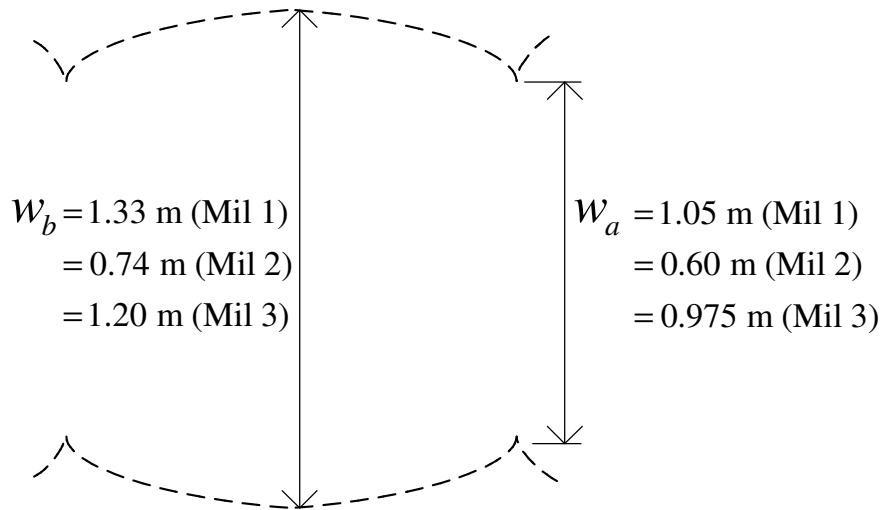


**Figure 3.5** Width  $w_a$  and average expanded width  $w_b$  of HB columns for different sizes of HB units

For Trials 1 and 2, a laser scanning device was not employed and the bulged width was manually measured at the top of each column using a tape measure. The average bulged width  $w_b$  for the Mil 3 two course walls in Trials 1 and 2, as listed in Table 3.1, is 1.20 m.

### 3.1.5 Pressure measurements

For each experiment, the loading was provided by an explosive charge at a standoff that produced a nearly uniform pressure over the wall face, as validated using AutoDyn Computational Fluid Dynamics software [34] as well as ConWep [17]. Note that the validity of assuming uniform loading for this study will be discussed in Section 6.2. Prior to each trial, calculations were performed using ConWep to estimate the loading and select appropriate standoffs for the experiments. The overpressure-time history exerted on the face of the walls from the blast loading in all experiments was measured by PCB® pressure

sensors with Delrin® inserts in the steel circular mounts as shown in Figure 3.6 (a). The mounts were installed into the HB walls prior to filling them with soil, and Figure 3.6 (b) shows the enclosed steel tubing on the inside of the wall used to house and protect each pressure gauge. The gauge cabling was threaded through the hose connected to the steel tubing, which is shown to protrude out the back of the wall (the side facing away from the blast) in Figure 3.6 (c). A sampling interval of 1  $\mu\text{s}$  was used for recording the pressure-time histories. For Trials 1 through 3, one pressure gauge was mounted at approximately mid-height of the middle column to measure the pressure-time history applied to the face of the wall. Although pressure traces were successfully recorded for Trials 1 through 3, only a modest success rate was achieved in recording entire pressure-time histories due to gauges being struck by dust or debris. Thus for Trials 4 through 7, three reflected pressure gauges were used for each wall; one at each of the centre three columns. This was done to help ensure that at least one successful pressure-time history would be recorded. Three gauge mounts in Trial 4 can be seen in the centre three columns of the Mil 3 wall shown in Figure 3.2 (a).

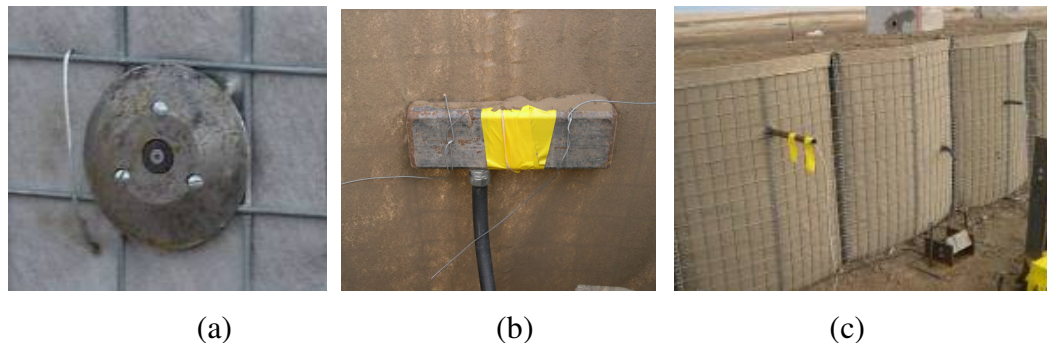


**Figure 3.6 Details of reflected pressure gauge setup: (a) pressure gauge in steel circular mount on wall facing the blast; (b) gauge mounted in steel tubing inside Hesco cell before filling; and (c) gauge cables run through rubber hose exiting wall facing away from the blast**

### 3.1.6 Photo and video

Pre- and post-experiment photos were taken for a visual record of the deformation. A Phantom® high speed video camera in a protected enclosure was used to record the experiment operating at a frame rate of 1 frame/ms. The aim of the high speed video was to capture a visual record of the response of the walls, which based on preliminary FE modelling was expected to last at least 500 ms. However, dust and debris raised from the blasts obscured the response of the walls from view. Therefore only the pre- and post-experiment photos are available for a visual record of the final deformation.

### 3.1.7 Displacement and deformed position measurements

In Trials 4 through 7, the displacement–time histories of the walls at selected points were measured using the Intertechnology Incorporated Celesco® retractable displacement gauges, Figure 3.7 (a), mounted within steel frame stands behind each wall, as shown in Figure 3.7 (b).



**Figure 3.7 Details of displacement gauge setup: (a) retractable cable displacement gauge; and (b) steel framing and protective housing for displacement gauges, (cables shown in dashed lines)**

The upper monitoring point displacement was recorded by three retractable cable displacement gauges separated at 30 degree angles (see Figure 3.1). Note that only two gauges are required to calculate both horizontal and vertical displacements, but a third was added for redundancy and to ensure a successful measurement in case one of the three gauges failed to measure properly due to the harsh loading environment. Two additional displacement gauges were used to measure displacement at the lower monitoring point with both cables initially at horizontal (Figure 3.1). Although only one displacement gauge was necessary for this measurement, additional displacement gauge was used for redundancy. Table 3.2 lists the relevant distances,  $h_{m_u}$ ,  $h_{m_l}$ , and  $A$  in Figure 3.1, for Trials 4 through 7 involving cable displacement measurements.

**Table 3.2 Overview of distances for cable displacement gauge setup in Figure 3.1**

<b>Trial</b>	<b>HB Unit (width × depth × height) (mm × mm × mm)</b>	<b>Height of upper displacement monitoring point, <math>h_{m_u}</math> ( m)</b>	<b>Height of lower displacement monitoring point, <math>h_{m_l}</math> (m)</b>	<b>Horizontal distance from displacement monitoring point to frame displacement gauges, <math>A</math> (m)</b>
4 (2006)	Mil 3 (975 × 975 × 975)	1.50	0.225	2.25
5 (2006)	Mil 1 (1050 × 1050 × 1350)	0.825	0.225	0.942
6 (2006)	Mil 3 (975 × 975 × 975)	1.425	0.225	2.25
7 (2006)	Mil 1 (1050 × 1050 × 1350)	0.825	0.225	0.942

Note that the discrepancy in the height of the upper monitoring point between Trial 4 and 6 was due to an oversight occurring during the experimental setup, and the height origi-

nally intended for the upper monitoring point in Trial 6 was 1.50. The cable displacement measurements were sampled every 0.02 ms.

## 3.2 Soil properties

Several soil tests were conducted to characterize the soil and derive its mechanical properties. The testing pertinent to each experiment is outlined in Table 3.3.

**Table 3.3 Soils testing program for the blast experiments**

<b>Trial</b>	<b>HB Unit (width × depth × height) (mm × mm × mm)</b>	<b>Courses (wall height, m)</b>	<b>Filled Width <math>w_b</math> (m)</b>	<b>Soils tests</b>
1 (2003)	Mil 3 (975 × 975 × 975)	2 (1.95)	1.2	Densometer ( $\rho_{wet}$ , MC); triaxial tests, Set 1, fully saturated (yield relationship, EOS, $K$ , $G$ )
2 (2003)	Mil 3 (975 × 975 × 975)	2 (1.95)	1.2	Same as Trial 1
3 (2004)	Mil 2 (600 × 600 × 600)	2 (1.2 m)	0.74 m	Densometer ( $\rho_{wet}$ , MC), no triaxial, but other properties assumed same as trials 4 through 7 due to similarity in density and MC
4 (2006)	Mil 3 (975 × 975 × 975)	2 (1.95)	1.2	Densometer ( $\rho_{wet}$ , MC); triaxial tests, Set 2, un-saturated (yield relationship, EOS, $K$ , $G$ ); sieve and hydrometer particle size analysis; and standard cone penetrometer
5 (2006)	Mil 1 (1050 × 1050 × 1350)	1 (1.35)	1.33	Same as Trial 4
6 (2006)	Mil 3 (975 × 975 × 975)	2 (1.95)	1.2	Same as Trial 4
7 (2006)	Mil 1 (1050 × 1050 × 1350)	1 (1.35)	1.33	Same as Trial 4

To obtain the Equation of State (EOS), the Yield Relationship, and the Bulk and Shear moduli ( $K$  and  $G$ , respectively), two sets of triaxial tests were conducted; one for the trial series in 2003 consisting of Trials 1 and 2, and one set for the trial series in 2006 consisting of Trials 4 through 7. Note that Trial 3 was conducted as a side experiment to a larger series involving alternate trial objectives. For Trial 3, apart from wet density ( $\rho_{wet}$ ) and moisture content (MC) measurements using a densometer, detailed soils testing was not undertaken due to constraints in trial objectives and budget.

### 3.2.1 Particle size analysis and soil classification

For the trial series in 2006 (Trials 4 through 7), several disturbed samples of soil were taken from the walls immediately after each experiment.

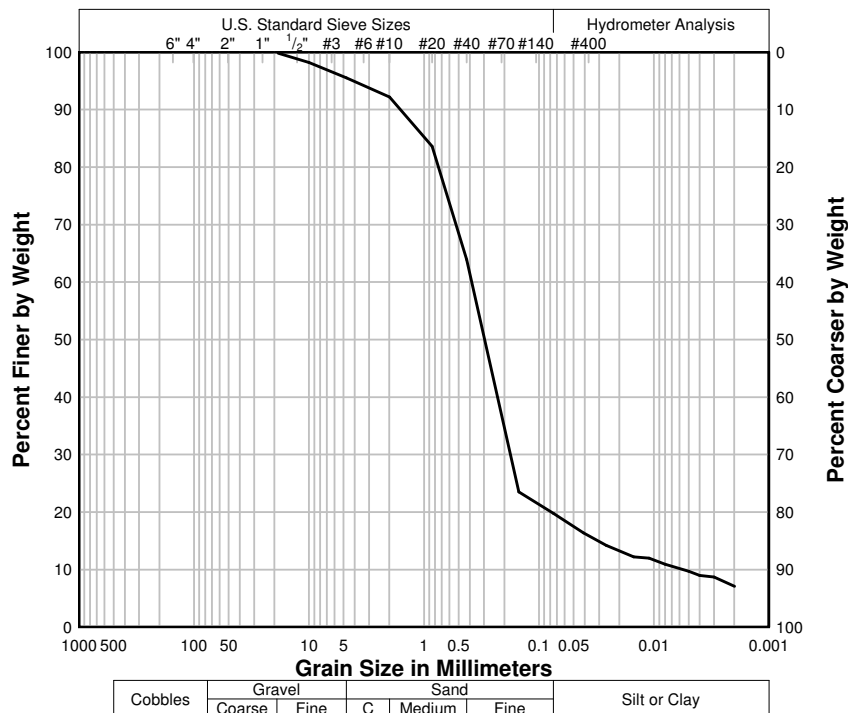


Figure 3.8 Particle size analysis of the silty-sand used in the experiments



A sieve analysis was conducted for the fill (ASTM D 422 – 63 [36]), and the soil was classified as a silty-sand under the Unified Classification system (ASTM D 2487 – 90 [37]) with 19.8 % passing the no. 200 sieve. A hydrometer analysis was conducted for the fine particles and the resulting gradation curve is shown in Figure 3.8. Particle size analysis was not conducted for the soil in the trial series in 2003 or 2004, however throughout the HB wall test program the site and source of soil-fill remained consistent, apart from seasonal changes in moisture content and resulting compacted density.

### 3.2.2 Densities and moisture contents

The density and moisture content of the soil-fill was measured within two hours prior to each experiment using the Humboldt Scientific Incorporated Model 5001 B nuclear densometer, which is shown in Figure 3.9 (a).



(a)



(b)

**Figure 3.9 Measurement of densities: (a) density measurement for HB wall using nuclear densometer; and (b) manual density measurement.**

For the two-course walls, in Trials 1 and 2, only the density at the top of the three centre HB columns were measured, while for Trials 3, 4, and 6 density measurements were con-

ducted for the three centre HB columns at the top of each course. The densities in all trials were measured using the direct transmission mode using a probe depth of 200 mm. Due to the proximity of the sidewalls of the HB units in this measurement configuration, care was taken to apply correction factors to the density and moisture content readings to help mitigate errors caused by possible boundary effects. This was conducted by comparing measurements of the standard count inside and outside the walls using the standard density block supplied with the densometer. The corrections were calculated according to the operator's manual supplied by the densometer manufacturer, Humboldt [38]. The density and MC readings were averaged to obtain an overall density and MC reading for each wall. The average wet density measurements and MCs for each HB wall are listed in Table 3.4. Note that the trial series in 2003 consisting of Trials 1 and 2 were performed in late March when the soil was in a moist condition, enabling significantly higher compacted densities compared with the other trials which were carried out in August through October. The densities and MC measured in each wall were reasonably close within their respective trial series, where the density did not vary by more than  $50 \text{ kg/m}^3$  (for density measurements ranging from  $1566$  to  $1850 \text{ kg/m}^3$ ) and the MC did not vary by more than 2 % for individual measurements made within each trial series. The density of the ground at the base of the walls was significantly higher than the densities measured in the walls, and averaged  $2100 \text{ kg/m}^3$  with 10 % moisture. To validate the densities measured by the densometer, six comparative manual measurements were undertaken. For each comparison, a density measurement was taken at a given spot using the densometer, and then the area surrounding the probe hole was carefully excavated, as shown in Figure 3.9 (b). This removed soil was weighed and the excavation was lined with thin plastic and filled with

water until level with the surrounding ground. The weight of water required to fill the excavation was recorded and compared with the weight of soil removed to calculate the in-situ soil density. In all instances, the manually measured densities were within 50 kg/m<sup>3</sup> of the densities recorded by the densometer.

**Table 3.4 Summary of the HB walls tested in each trial**

<b>Trial (year)</b>	<b>HB Unit (width × depth × height) (mm × mm × mm)</b>	<b>Courses (wall height, m)</b>	<b>Filled Width <math>w_b</math> (m)</b>	<b>Average Soil <math>\rho_{\text{wet}}</math> (kg/m<sup>3</sup>)</b>	<b>Average % MC</b>
1 (2003)	Mil 3 (975 × 975 × 975)	2 (1.95)	1.2	1850	15.5
2 (2003)	Mil 3 (975 × 975 × 975)	2 (1.95)	1.2	1850	15.1
3 (2004)	Mil 2 (600 × 600 × 600)	2 (1.2)	0.74	1646	9.5
4 (2006)	Mil 3 (975 × 975 × 975)	2 (1.95)	1.2	1572	7.6
5 (2006)	Mil 1 (1050 × 1050 × 1350)	1 (1.35)	1.33	1577	7.7
6 (2006)	Mil 3 (975 × 975 × 975)	2 (1.95)	1.2	1566	7.5
7 (2006)	Mil 1 (1050 × 1050 × 1350)	1 (1.35)	1.33	1575	7.7

### 3.2.3 Cone penetration tests

To determine the rigidity of the supporting ground compared with the soil-fill in the HB walls, standard penetrometer tests were conducted for the trial series involving Trials 4 through 7. A 25 mm cone Humboldt HS 4210 standard cone penetrometer (ASTM D1586 – 08a [39]) with a probe penetration depth of 100 mm was used. The readings for the soil

within the HB cells averaged  $3 \text{ kg/cm}^2$  while the readings for the supporting ground averaged  $27 \text{ kg/cm}^2$ . The readings within the HB cells ranged from 1 to  $10 \text{ kg/cm}^2$  while the readings for the supporting ground ranged from 22 to  $41 \text{ kg/cm}^2$ . The tests gave an indication of the bearing strength of the soil, but also illustrated that the ground was far more rigid than the soil-fill in the HB units. This is consistent with the fact that far greater densities were measured for the ground versus the soil in the walls, ( $2100 \text{ kg/m}^3$  versus 1550 to  $1850 \text{ kg/m}^3$ ), as shown in the previous section.

#### 3.2.4 Yield relationship

To derive the Yield Relationship, the EOS,  $K$  and  $G$ , two sets of triaxial tests were conducted; ‘Set 1’, for the trial series in 2003 consisting of Trials 1 and 2; and ‘Set 2’, for the trial series in 2006 consisting of Trials 4 through 7. Undrained Tests were chosen due to the abrupt loading and response in the experiment. The explanations and test results for the following sections are partitioned into ‘Set 1’ and ‘Set 2’.

##### ***Set 1:***

The yield relationship for the soil in Trials 1 and 2 was derived through three Consolidated Undrained (CU) Triaxial tests performed in 2003 according to ASTM D4767 – 95 [40]. Confining pressures of approximately 1000, 1500, and 2000 kPa were used. The relatively high pressures were selected based on the magnitude of blast overpressures in the experiment. The wall construction occurred in the spring, therefore the soil was especially moist and enabled the soil-fill in the walls to be well compacted. The density meas-

ured in the walls was  $1850 \text{ kg/m}^3$  and the average MC for Trial 1 is 15.5 and Trial 2 is 15.1 %. The samples of soil were obtained from the soil-fill in the walls post-experiment. Triaxial test specimens were formed by compaction to 100 % Standard Proctor density, (ASTM D 1557 – 02 [41]), which resulted in samples averaging  $1860 \text{ kg/m}^3$ . The average MC of the samples prepared was 16.7 % MC, which was within 10 % of the average MC of 15.3 % measured within the walls in Trials 1 and 2, as shown in Table 3.4. The tests were undrained which meant that once the confining pressure  $\sigma_h$  had been established and the soil was in a saturated state and shearing was about to commence, the drainage from the soil specimen was closed. Pore water in the soil was unable to leave the system resulting in appreciable pore water pressure  $\sigma_u$ . Under these conditions it is assumed that only the soil skeleton is capable of sustaining shear stress, and thus the Mohr's circles and failure envelope is based on the stresses on the soil skeleton which are the effective stresses. The data obtained from the three tests is presented in Table 3.5.

**Table 3.5 Data points for saturated soil from Set 1 triaxial tests**

Test No.	Initial $\rho_{wet}$ in Saturated State ( $\text{kg/m}^3$ )	MC in Saturated State (%)	Confining Pressure, $\sigma_h$ (kPa)	Peak Total Axial Stress, $\sigma_A$ (kPa)	Pore Pressure at Peak Axial Stress, $\sigma_u$ (kPa)	Effective Confining Pressure, $\sigma'_h$ (kPa)	Peak Effective Axial Stress, $\sigma'_A$ (kPa)
1	2063	21.7	1034	1439	928	106	511
2	2073	20.9	1555	2417	1271	284	1146
3	2097	19.8	1999	3032	1471	528	1561

The effective stresses are calculated by subtracting the pore water pressure from the confining pressure  $\sigma_h$  and axial stress  $\sigma_A$ . The primes denote effective rather than total quantities. The Mohr-Coulomb criteria can be represented by the line

$$\tau' = c' + \tan(\phi')\sigma_n', \quad (3.1)$$

where  $c'$  is the effective cohesion of the soil and  $\phi'$  is the effective angle of friction of the soil. The resulting Mohr's circles from Table 3.5 and best fit line are shown in Figure 3.10.

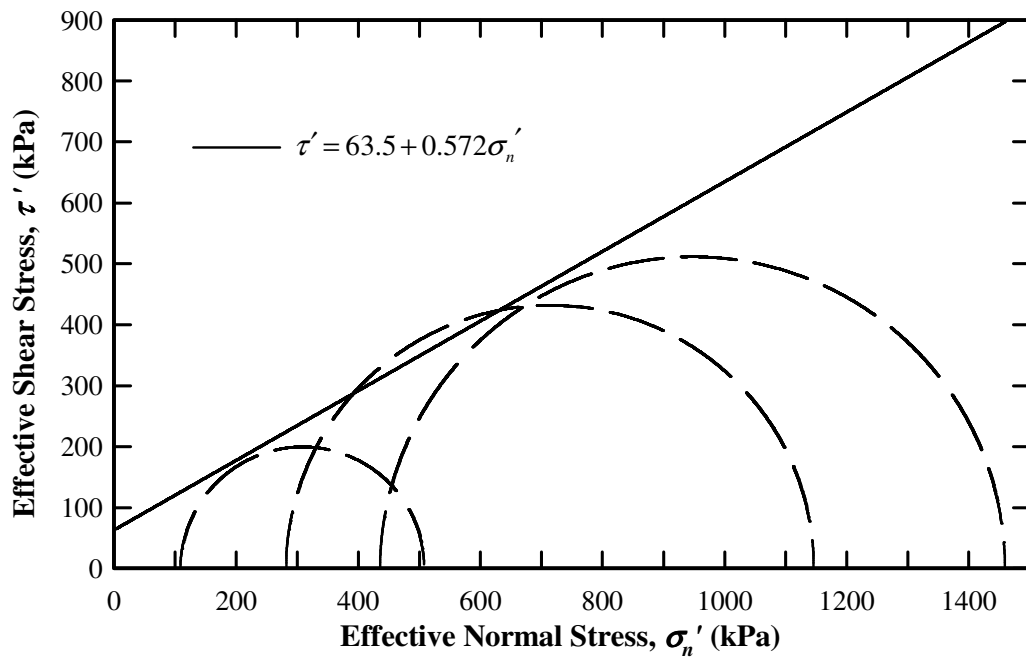


Figure 3.10 Mohr-Coulomb analysis and best fit line for Set 1 triaxial tests

The best fit line in Figure 3.10 resulted in  $c' = 63.5$  kPa and  $\tan(\phi') = 0.572$ , which corresponds to an effective angle of friction  $\phi' = 29.8^\circ$

***Set 2:***

To obtain the yield relationship pertinent to Trials 4 through 7, four Unconsolidated Undrained (UU) triaxial tests were performed in 2006 on disturbed samples according to the specifications in ASTM standard D4767 – 02 [42]. The confining pressures of 40, 70, 110, and 160 kPa were used. Note that the pressures selected were lower than in Set 1 because according to pre-trial finite element (FE) model results, (which were not available in 2003), apart from the initially high compressive stresses applied to the soil at the face of the blast, the majority of the response of the wall took place after the blast loading. The response was more dependent on the properties of soil compressed at the base, and the pressures at the base near the corner of rotation were shown to not exceed 160 kPa in the pre-trial FE model. One additional change was made in the soil test, i.e. to derive soil properties to represent the actual soil conditions in the blast experiments, contrary to what was performed in Set 1 and contrary to ASTM standards [42], no saturation phase was undertaken. The samples were watered and compacted in a cylindrical mould to approximately match the densities and MC measured in the soil-filled walls in the experiments in Table 3.4 for Trials 4 through 7. It was expected that even under high compression from blast, the soil would be dry enough that a saturated state would not occur and substantial pore pressure would not develop. Thus the effective stresses would be roughly equal to the total stresses. The compacted soil in the experiments at the measured density and MC in Table 3.4 was too loose to form cohesive samples at the experimental densities. Therefore the triaxial test specimens were formed at  $\rho_{wet}$  of 1700 kg/m<sup>3</sup>. This density is within 3.2 % of the density in Trial 3, thus the properties derived for Set 2 for Tri-

als 4 through 7 are also applicable for Trial 3. The initial  $\rho_{wet}$  and MC of the triaxial test specimens are listed in Table 3.6. Each sample undergoing a triaxial test was initially confined under hydrostatic stress, and then subjected to additional axial stress until failure. The test data for these four triaxial tests are also given in Table 3.6.

**Table 3.6 Data points for unsaturated soil from Set 2 triaxial tests**

Test No.	Initial $\rho_{wet}$ (kg/m <sup>3</sup> )	MC (%)	Confining Pressure, $\sigma_h$ (kPa)	Peak Total Axial Stress, $\sigma_A$ (kPa)
1	1718	8.9	40	108.8
2	1712	8.8	70	168.5
3	1730	8.8	110	295.8
4	1719	8.9	160	417.9

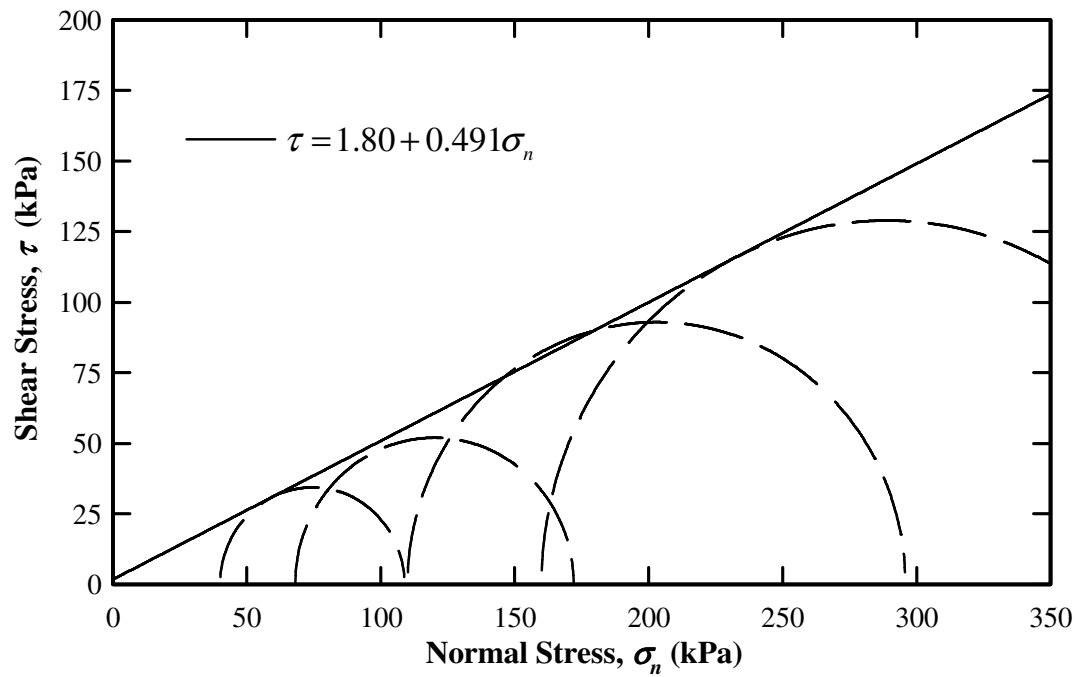


**Figure 3.11 Mohr-Coulomb analysis and best fit line for Set 2 triaxial tests**



Using the points in Table 3.6, Mohr-Coulomb analysis was conducted based on the total stresses and the results are plotted in Figure 3.11. The best fit line is given by

$$\tau = 1.80 + 0.491\sigma_n \quad (\text{in kPa}), \quad (3.2)$$

which corresponds to a cohesion and angle of friction of  $c = 1.80$  kPa and  $\phi = 26.2^\circ$ , respectively.

### 3.2.5 Equation of State (EOS)

#### *Set 1:*

The samples used to obtain the yield relationship for Set 1 were also used to obtain the EOS. The EOS was measured through monitoring volume changes within the initial hydrostatic compression phase of the tests after the soil underwent saturation.

**Table 3.7 EOS points for saturated soil using triaxial cell in hydrostatic compression for Set 1**

Test No.	Initial Wet Density (kg/m <sup>3</sup> )	Initial MC (%)	Initial $\rho_{wet}$ in Saturated State (kg/m <sup>3</sup> )	MC in Saturated State (%)	Confining Pressure, $\sigma_h$ (kPa)	Pore Pressure Pre-shearing, $\sigma_u$ (kPa)	Effective Confining Pressure, $\sigma_h'$ (kPa)	Volumetric Strain, $\varepsilon_v$
1	1841	14.6	2063	21.7	1034	565	469	0.0525
2	1887	18.3	2073	20.9	1555	597	958	0.0589
3	1855	17.1	2097	19.8	1999	487	1512	0.0956

The pore pressure was monitored and recorded for each test at the total confining pressures of 1000, 1500, and 2000 kPa. The data recorded for the triaxial tests pertinent to the compression phase are summarized in Table 3.7. Due to the samples being saturated before compression, pore pressures were subtracted from total pressures to obtain the pressures sustained by the soil skeleton. A plot of the effective hydrostatic pressure with the volume change on the horizontal axis is shown in Figure 3.12.

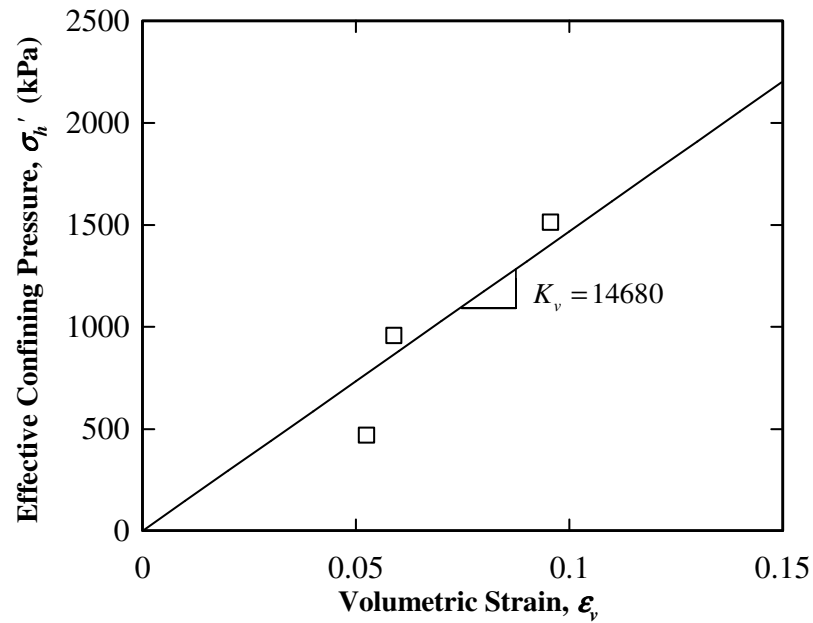


Figure 3.12 Equation of State obtained from Set 1 triaxial tests

Linear regression was used to obtain the relationship between the effective confining pressure  $\sigma'_h$  and the resulting volumetric strain  $\epsilon_v$  as

$$\sigma'_h = 14680\epsilon_v \quad (\text{in kPa}). \quad (3.3)$$

The correlation coefficient of Eq. (3.3) is 0.892.

**Set 2:**

Three additional unconsolidated undrained (UU) triaxial tests were conducted on disturbed samples of soil from the post-experiment HB walls in 2006 to obtain the EOS. The additional tests were conducted so that EOS data could be generated for measurable compressions so that a relationship could be provided to accommodate the relatively high pressures arising from the blast load, as the previous tests at 40, 70, 110, and 160 kPa did not yield measurable volumetric strains in the compression phase. These additional UU tests were conducted at the same confining pressures as used in generating the EOS for Set 1: 1000, 1500, and 2000 kPa. Regarding the selection of hydrostatic pressures applied, note that the peak pressure from the blast loading in the experiments ranged from 4,000 to 20,000 kPa during the first millisecond of the loading, and numerical results using the FE models indicated that, after this first millisecond of the loading, the soil stresses were typically lower than 160 kPa. Thus the range in pressure values tested (1,000 to 2,000 kPa) was deemed to be a reasonable compromise between the high peak pressures of the blast loading and the low pressures involved in the HB wall response. Furthermore the triaxial testing machine available was limited to pressures at or below 2000 kPa. Yield results had already been obtained from the four previous tests at 40, 70, 110, and 160 kPa. Therefore, contrary to the ASTM standard [42], the test specimens were only hydrostatically compressed and subsequent application of axial loading was not performed. No initial saturation phase was undertaken as the specimens were to be tested at MC equivalent to the soil in the blast experiments. The initial saturation level of the test specimens averaged approximately 34 %. The three additional specimens were formed from the excess soil sampled, and were watered and compacted in a cylindrical mould to approximately 8 % MC and 1700 kg/m<sup>3</sup>. Note that the densities of the speci-

mens prepared were again increased from the target density of 1550-1600 kg/m<sup>3</sup> due to the inability to form cohesive samples. Volumetric strain measurements were recorded through measuring changes in fluid volume within the confining cell of a Double Cell Triaxial System, Jian-Hua [43]. The initial  $\rho_{wet}$  and the MC of each sample formed was recorded as presented in Table 3.8.

**Table 3.8 EOS points for unsaturated soil using triaxial cell in hydrostatic compression for Set 2**

Sample No.	Initial $\rho_{wet}$ (kg/m <sup>3</sup> )	Initial MC (%)	Confining Pressure, $\sigma_h$ (kPa)	Volumetric Strain, $\epsilon_v$
1	1697	8.5	1000	0.0539
2	1723	8.8	1500	0.0607
3	1708	8.6	2000	0.1004

Note that none of the samples approached 100 % saturation when subjected to the confining pressures. The highest saturation level calculated was for Sample 3 which reached 45 % saturation. A plot of the results in Table 3.8 is shown in Figure 3.13. Linear regression was used to obtain the relationship between the confining pressure  $\sigma_h$  and the resulting volumetric strain  $\epsilon_v$  as

$$\sigma_h = 20740\epsilon_v \quad (\text{in kPa}). \quad (3.4)$$

Note that the best linear fit line was constrained to passing through the origin for both Sets 1 and 2, representing zero pressure at zero volumetric strain. The correlation coefficient of Eq. (3.4) is 0.918. In lieu of specialized testing to test above total confining pressures of 2000 kPa, the best fit line was extrapolated to higher pressures and used in this thesis because the peak pressures only constitute a minor aspect of the loading and the

majority of the response from pre-trial FE modelling had shown response to be impulse dominated (Scherbatiuk [24]).

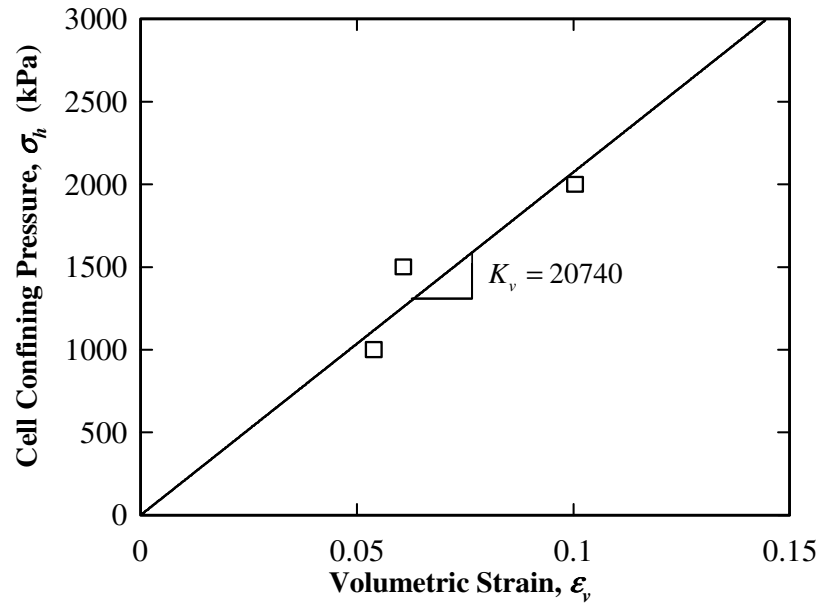


Figure 3.13 Equation of State obtained from Set 2 triaxial tests

### 3.2.6 Bulk and shear moduli

#### *Set 1:*

The bulk modulus  $K$  and shear modulus  $G$  were determined at the initial compression phase of the three triaxial tests used to derive the EOS and yield relationship for Set 1. Upon loading the specimens with axial pressure, measurements of the changes in axial strain and pore pressure were recorded and effective axial and confining stresses were calculated. For each test, the first three of the readings of measurable volume change when the axial load was applied were used to determine the values for  $K$  and  $G$  and

these three results were averaged. This was done because in measuring very small volumetric strains, errors in the measurements that are disproportionately large compared to the measured values would occur. Averaging the measurements was deemed as a way to reduce this error. Secondly, since no unloading cycles take place in the initial compression phase and the bulk modulus is only a description of the unloading modulus, an approximation is made that the unloading modulus is equal to the initial modulus. So it is approximated that most of the deformation is elastic and it is assumed that a small amount of plastic deformation is tolerable as an error in the measurement. Note that the values for  $K$  and  $G$  decrease with increased readings, indicating that volumetric yielding is taking place. Thus taking the first three measurements provides a compromise between reducing the error in the volumetric strain measurement, while still providing elastic coefficients based mostly on deformation that is recoverable. Furthermore errors in the measured values of  $K$  and  $G$  are tolerable because, as will be shown in Subsection 6.4.5, no noticeable changes in the response of the finite element model occur with increasing or decreasing  $K$  and  $G$  by a factor of two.  $K$  and  $G$  were calculated from

$$K = \frac{\sigma_m}{\epsilon_v}, \text{ and} \quad (3.5)$$

$$G = \frac{\sigma_A - \sigma_h}{3\epsilon_A - \epsilon_v}. \quad (3.6)$$

Here  $\sigma_m$  is the mean stress, and is given by

$$\sigma_m = \frac{2\sigma_h + \sigma_A}{3}, \quad (3.7)$$

while parameters  $\varepsilon_v$  and  $\varepsilon_A$  represent the volumetric strain and the axial strain, respectively. Note that since the specimens were saturated, pore pressures were subtracted from the axial and confining stress in order to obtain effective stresses which are pertinent to the stiffness of the soil skeleton. The effective stresses were used with Eqs. (3.5) and (3.6) to calculate the bulk and shear moduli. The individual readings are given in Table 3.9. The average  $K$  and  $G$  of all measurements were calculated to be 187.6 and 15.4 MPa, respectively.

**Table 3.9 Bulk and shear moduli measurements for Set 1**

Test No.	Reading	$K$ (MPa)	$G$ (MPa)
#1 (at 1000 kPa)	1	99.7	8.19
	2	61.46	5.05
	3	50.02	4.11
#2 (at 1500 kPa)	1	415.92	34.19
	2	289.02	23.76
	3	254.19	20.89
#3 (at 2000 kPa)	1	265.62	21.83
	2	145.78	11.98
	3	106.39	8.74

**Set 2:**

$K$  and  $G$  were determined at the initial compression phase of the four triaxial tests (at 40, 70, 110, and 160 kPa) used for the yield relationship for Set 2. Since the soil was not

saturated for this test, nor did it approach saturation in the hydrostatic compression, no adjustments were necessary to account for pore pressure. Using Eqs. (3.5) and (3.6), the following values were calculated and are presented in Table 3.10. The average  $K$  and  $G$  of all measurements were calculated to be 163.3 and 8.3 MPa, respectively.

**Table 3.10 Bulk and shear moduli measurements for Set 2**

Test No	Reading	$K$ (MPa)	$G$ (MPa)
#1 (at 40 kPa)	1	223.64	3.304
	2	146.32	2.493
	3	125.26	2.178
#2 (at 70 kPa)	1	309.2	4.549
	2	211.82	3.36
	3	131.2	2.27
#3 (at 110 kPa)	1	137.86	24
	2	112.28	10.62
	3	118.24	15.33
#4 (at 160 kPa)	1	229.14	9.178
	2	132	13.66
	3	83.08	9.218



# Chapter 4

## FE Model

This chapter provides the details for the formulation of the finite element (FE) model. This includes the geometry, material models, their input parameters, and the boundary conditions. A mesh resolution study is conducted at the end of this chapter to determine the appropriate element size.

### 4.1 Geometry

The LS-Dyna explicit FE code was used to construct a FE model of the wall. TrueGrid software was used to generate the FE mesh. The pre-experimental volumes of the filled walls were calculated using laser scanning as shown in Figure 3.4 (a) and (b), and the volumes of the FE models of the walls were tailored to match the measured volumes in the experiments. The bulges of the filled HB unit sidewalls were approximated using cosine functions, and the extent of the bulges for the given wall size in each experiment are presented in Table 3.1 and Figure 3.5. Fully integrated eight node constant stress solid elements were used (Livermore Software Technology Corporation [44]). The element

size was chosen to be proportional to the sizes of the steel mesh of the HB units in order to merge the nodes of the soil elements with those of the wire mesh.

## 4.2 Material models

The material model selected in LS-Dyna to model the soil was MAT\_SOIL\_CONCRETE (Livermore Software Technology Corporation [44]). This material model calls for user-defined tabulated piecewise-linear descriptions for the EOS and yield relationship, as well as the density, bulk and shear modulus. The MAT\_SOIL\_CONCRETE material model was selected because it was general enough to consider both linear and non-linear EOS or yield relationships. The EOS, Yield relationships,  $K$  and  $G$ , and appropriate  $\rho$  presented in the previous section on soil properties were used for the models. For the Mohr–Coulomb yield parameters to be compatible with the MAT\_SOIL\_CONCRETE material model, the following two equations were used to find the equivalent Drucker–Prager yield parameters (Desai and Siriwardane [45]):

$$\alpha_D = \frac{6\sin\phi}{3-\sin\phi}, \text{ and} \quad (4.1)$$

$$k_D = c \frac{6\cos\phi}{3-\sin\phi}, \quad (4.2)$$

where  $c$  and  $\phi$  are the Mohr–Coulomb cohesion and angle of friction. The Drucker–Prager relationship in terms of parameters  $\alpha_D$  and  $k_D$  are given as

$$\sigma_Y = k_D + \alpha_D \sigma_m, \quad (4.3)$$

where the mean stress,  $\sigma_m$ , can be calculated from Eq. (3.7) or from the principal stresses as

$$\sigma_m = \frac{\sigma_1 + \sigma_2 + \sigma_3}{3}. \quad (4.4)$$

The Von Mises stress in each element is compared to the yield stress,  $\sigma_y$ , Eq. (4.3), within the FE program to determine if yielding occurs, and if so a perfectly plastic stress-strain relationship is assumed. The Von Mises stress is given as

$$\sigma_{VM} = \sqrt{\frac{1}{2}[(\sigma_1 - \sigma_2)^2 + (\sigma_1 - \sigma_3)^2 + (\sigma_2 - \sigma_3)^2]}. \quad (4.5)$$

Beam elements of a 4 mm diameter were used to represent the steel wire and the nodes of the steel wire coincided with the nodes of the solid elements. The Simplified Johnson–Cook model (Johnson and Cook [46]) was used to model the mild steel weld mesh. The steel parameters used in the model were

$$E = 200 \text{ GPa}; \quad \nu = 0.3; \quad \text{and} \quad \rho_s = 7800 \text{ kg/m}^3, \quad (4.6)$$

where  $E$ ,  $\nu$ , and  $\rho_s$  are the Young's Modulus, Poisson's ratio, and density of steel, respectively. In the model, Johnson and Cook expressed the flow stress,  $\sigma_y$ , as

$$\sigma_y = (A_1 + B_1 \bar{\epsilon}^{p^{n_1}})(1 + c_1 \ln \epsilon^*), \quad (4.7)$$

where  $A_1$ ,  $B_1$ ,  $c_1$ , and  $n_1$  are input constants given by Pope et al. [4] which were set at  $3.5 \times 10^5$  kPa,  $2.75 \times 10^5$  kPa,  $2.2 \times 10^{-2} \text{ s}^{-1}$ , and 0.36, respectively, while  $\bar{\epsilon}^p$  is an effective plastic strain and  $\epsilon^*$  is the effective strain rate. Note that if the welded steel wire mesh

failed, it failed before the coils in all previous experiments. Therefore a pin connection was used to model the coils joining the welded wire mesh panels of the adjacent units.

The contribution of the geotextile was found to be minimal in affecting the overall response as shown in Appendix H. Less than a 3 % change in the displacement at any time occurred from inclusion of the geotextile into the model. Furthermore, modelling the contact forces between the geotextile and the soil increased the calculation time of the model by a factor of four. Therefore the geotextile was omitted from the FE model.

As mentioned in Chapter 3, the measured  $\rho$  of the ground at the base of the wall averaged 2100 kg/m<sup>3</sup>, which was much higher than the measured densities of the soil in the HB walls. Standard cone penetrometer tests presented in Subsection 3.2.3 showed the ground to be much stiffer in comparison to the compacted fill within the HB walls (values of 27 kg/cm<sup>2</sup> for the ground versus an average of 3 kg/cm<sup>2</sup> for the soil-fill within the walls). Therefore, it was justified to consider the ground to be a rigid planar surface. The tangent of the angle of friction was assumed as the coefficient of friction for the contact between the HB wall and the ground. The angle of friction from the yield relationship was 29.8° for Set 1, pertinent to Trials 1 and 2; and 26.2° for Set 2, pertinent to Trials 3 through 7. These two angles of friction correspond to coefficients of friction of 0.571 and 0.491 respectively.

### 4.3 Initial and boundary conditions

Body acceleration in the vertical direction was used in the model to simulate gravity. The model allowed the soil to settle under gravity and reach equilibrium in the first 500 ms. The FE model of a filled Mil 3 two course HB wall is shown in Figure 4.1 (a). Since the charges in each experiment were far enough to produce a uniformly distributed load on the wall face as stated in Subsection 3.1.5, only two half-columns of each HB wall, shown in Figure 4.1 (b), were simulated to reduce computational effort. Displacement boundary conditions of the nodes on the  $yx$ -plane of the edge surfaces are

$$u_{FE}, v_{FE} \neq 0; w_{FE} = 0, \quad (4.8)$$

where  $u_{FE}$ ,  $v_{FE}$ , and  $w_{FE}$  are displacements in the  $x$ -,  $y$ -, and  $z$ - directions, respectively.

The pressure-time histories measured from the experiments were applied to the face of the wall in the calculation.

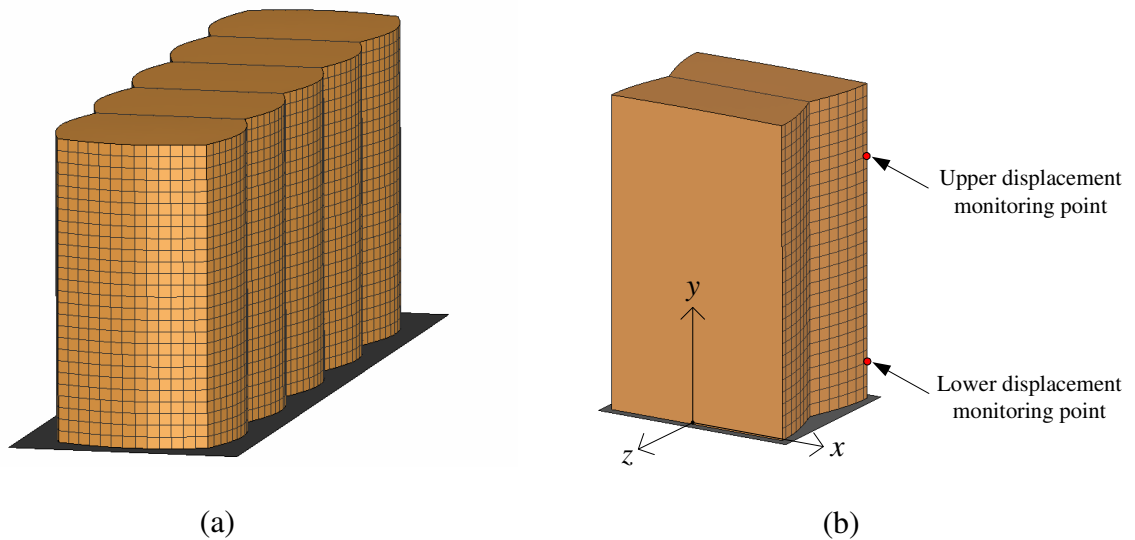


**Figure 4.1** FE model of Mil 3 two-course wall: (a) the entire wall and (b) two half-column model

## 4.4 Mesh resolution study

To determine the appropriate element size in the FE analysis, the Mil 3 two course HB wall size used in Trial 1 was selected for the mesh resolution study. The element sizes of 75, 37.5, 25, and 18.75 mm in each dimension were selected based on divisions of the 75 mm welded wire mesh spacing. Horizontal and vertical displacement–time histories of a monitoring point at 3/4 of the height of the wall on the back of the wall are shown in Figure 4.2 (a) and (b), respectively. It can be seen from the figures that the convergence was achieved when the element size was 37.5 mm or less. Therefore, an element size of 37.5 mm was selected for the FE analysis. Note that the model using 18.75 mm elements for a two half-column took approximately 110 h to calculate on an Intel® Pentium IV® 2.2 GHz processor with 1 GB ram while the model using 37.5mm elements took approximately 4 h to compute.

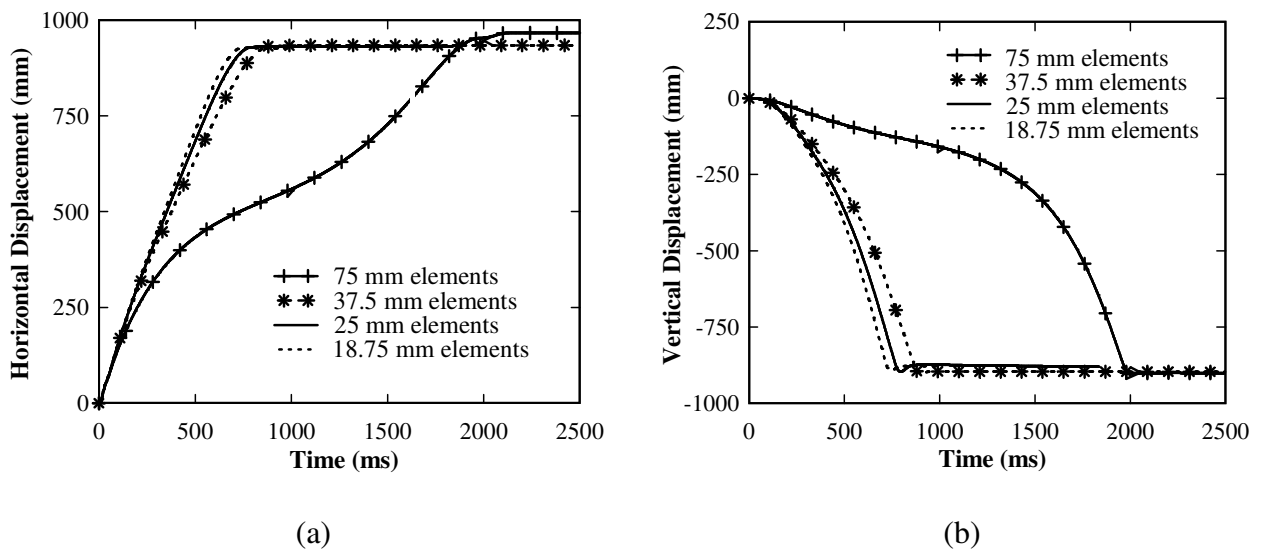


Figure 4.2 Comparison of displacement–time histories with different mesh resolutions: (a) horizontal displacement and (b) vertical displacement

# Chapter 5

## Derivation of Analytical Models

One of the aims of this thesis is to develop an efficient analytical model to calculate 2-*D* planar response of HB walls subjected to blast loading that enables rapid calculation of *P-I* curves. During the course of this thesis, although several models were investigated, only two models are successfully validated and reported, (Scherbatiuk and Rattanawangcharoen [24] and [26]). These two models consist of the preliminary model based on simple Rigid-Body Rotation, and the final model for this thesis, namely a Rigid-Body Hybrid model. The Rigid-Body Hybrid model combines rigid-body rotation with localized compression and shear deformation at the base of the wall. The following sections present the derivations of these models.

### 5.1 Rigid-Body Rotation model

Based on observations of experiment and results of an FE analysis, Rigid-Body Rotation appeared to contribute significantly toward the overall response. After careful and thor-

ough investigation of the behaviour of an HB wall under blast loading, four assumptions were made in order to achieve this simple and efficient model:

1. At the time of filling with soil, the weight of the soil caused each HB unit to expand laterally at the mid-length, and this expansion was assumed uniform throughout the height of the unit.
2. The dominant mode of deformation of the wall after subjecting to a blast load was rotation.
3. The axis of rotation was located at the bottom corner of the wall ( $Oz$  axis in Figure 5.1 (a)).
4. Ground shock and sliding of the wall were neglected.

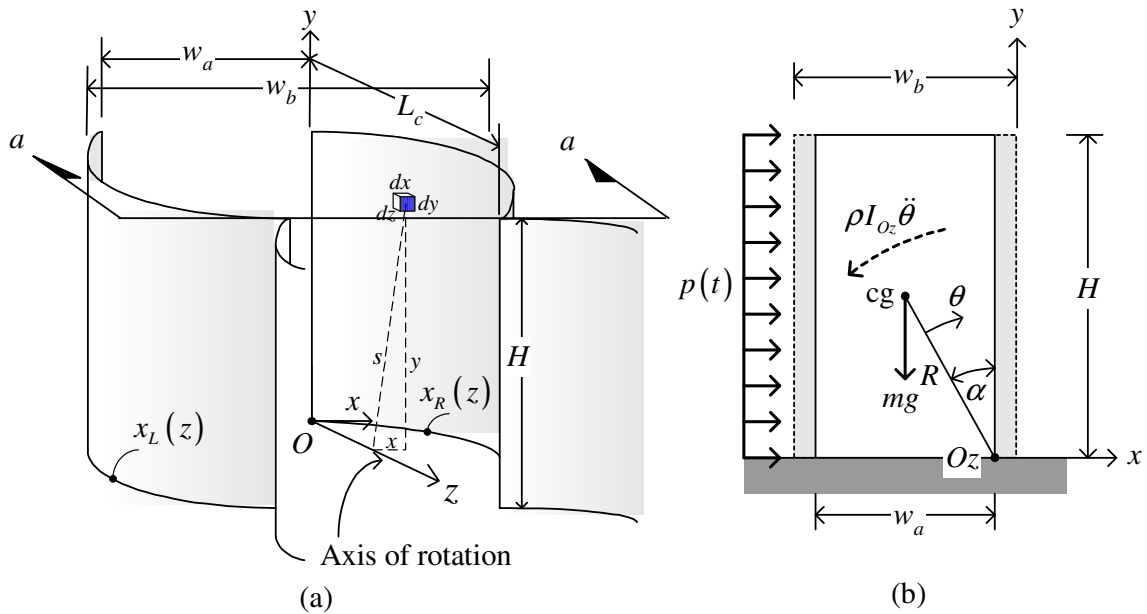


**Figure 5.1** Configuration of a rigid-body rotation model: (a) diagram illustrating calculation of inertial properties, (b) 2D elevation view and section a-a



The configuration of the model is shown in Figure 5.1 (a) with a side view shown in Figure 5.1 (b).

The lateral blast loading pressure  $p(t)$  is assumed to be applied uniformly and normal to the surface along the height of the wall  $H$ . The length of each HB unit is  $L_c$ . The width of the wall,  $w$ , varies along its length from the unfilled width,  $w_a$ , and the outermost extreme width of the lateral expansion or bulge after the wall has been filled and soil has been settled or compacted,  $w_b$ . This rigid block model has a uniform mass density  $\rho$ , an average mass per unit length  $m$  and a rotary inertia  $I_{Oz}$  about axis  $Oz$ . The block incurs a time history of rotation, denoted by  $\theta$ , about axis  $Oz$ , which is assumed to be located at the extent of the unfilled width  $w_a$ .  $R$  is the distance from the axis of rotation  $Oz$  to the location of the centre of gravity,  $cg$ . An angle  $\alpha$  is the angle between the line connecting axis  $Oz$  and the  $cg$ , referenced with the vertical, and represents the critical angle that the wall must rotate to in order to tip over with no further loading. From the geometry in Figure 5.1 (b),  $R$  and  $\alpha$  can be calculated based on unfilled dimensions, respectively, as

$$R = \frac{1}{2} \sqrt{(H^2 + w_a^2)}, \quad (5.1)$$

$$\alpha = \tan^{-1} \left( \frac{w_a}{H} \right). \quad (5.2)$$

Functions  $x_L(z)$  and  $x_R(z)$  denote the position of the wall on the left-hand side and right-hand side, respectively. These functions approximate the shape of the bulge using a sine function over the length of one unit, and are given as

$$x_L(z) = -w_a - \frac{(w_b - w_a)}{2} \sin\left(\frac{\pi z}{L_c}\right), \text{ and} \quad (5.3)$$

$$x_R(z) = \frac{(w_b - w_a)}{2} \sin\left(\frac{\pi z}{L_c}\right). \quad (5.4)$$

Consider an infinitesimal cubic element of dimensions  $dx$ ,  $dy$ , and  $dz$ , in the  $x$ -,  $y$ -, and  $z$ -directions, respectively, as shown in Figure 5.1 (a). The effective moment of inertia  $I_{Oz}$  of an HB column can be derived from

$$I_{Oz} = \frac{1}{L_c} \int_0^{L_c} \int_0^H \int_{x_L(z)}^{x_R(z)} s^2 dx dy dz, \quad (5.5)$$

where  $s$  is the distance from the axis  $Oz$  to the infinitesimal element as shown in Figure 5.1 (a). The result of the integration in Eq. (5.5), after simplification, is

$$I_{Oz} = \frac{w_a H}{3} \left\{ w_a^2 + H^2 + \frac{(w_b - w_a)^3}{3\pi w_a} + \frac{3}{8} (w_b - w_a)^2 + \frac{(3w_a^2 + 2H^2)(w_b - w_a)}{\pi w_a} \right\}. \quad (5.6)$$

An effective volume-per-unit length of an HB column can be calculated in a similar fashion as

$$\bar{V} = \frac{1}{L_c} \int_0^{L_c} \int_0^H \int_{x_L(z)}^{x_R(z)} dx dy dz. \quad (5.7)$$

Explicit expression of the effective volume-per-unit length of an HB column is

$$\bar{V} = w_a H + \frac{2H}{\pi} (w_b - w_a). \quad (5.8)$$

The mass-per-unit length of an HB column  $m$  can be obtained by multiplying the effective volume-per-unit length in Eq. (5.8) with the filled density  $\rho$ . The governing equation

of motion for the time-dependent rotational degree of freedom  $\theta$  of the rigid block model shown in Figure 5.1 (b) can be written as

$$\rho I_{O_z} \ddot{\theta} + mgR \sin(\alpha - \theta) = \frac{H^2}{2} p(t). \quad (5.9)$$

The impulse-dominated solution can be derived by assuming that, during the entire duration of blast loading, the wall has not deformed a significant amount so as to cause a change in its initial resistance and position. The blast load duration is very short compared to the duration of the response. Hence, the problem can be separated out to the blast loading imparting a velocity and corresponding kinetic energy to the wall. From this initial kinetic energy, absorption of energy due to strain or potential energy with rotation governs the maximum value of rotation achieved. The value calculated for the critical amount of impulse to topple the wall corresponds to the vertical asymptote of a  $P$ – $I$  diagram. This asymptote is approached when the load duration is very short and the pressures are very high. The initial response over the course of the blast loading approaches achieving an instantaneous velocity with negligible displacement. The energy balance requires that

$$KE = PE, \quad (5.10)$$

where  $KE$  and  $PE$  are kinetic and potential energies, respectively. Since the change in the stiffness of the differential equation during the duration of loading, Eq. (5.9), the velocity delivered by the blast loading that is used to calculate kinetic energy can be obtained by integrating the equation of motion over the blast load duration  $t_d$ . The rotational velocity transferred by triangular pulse is therefore

$$\dot{\theta}(t_d) = \frac{I}{\rho I_{O_z}} \left[ \frac{H^2}{2} - \frac{2mgR}{P} \sin \alpha \right], \quad (5.11)$$

where  $I$  is the impulse and  $P$  is the peak pressure. A triangular pulse was selected for this analysis because it has a time duration that is finite. The impulse for a triangular blast wave is given by

$$I = \frac{Pt_d}{2}. \quad (5.12)$$

The kinetic energy at the end of the blast loading can be calculated directly from Eq. (5.11), i.e.

$$KE = \frac{1}{2} \rho I_{O_z} [\dot{\theta}(t_d)]^2 = \frac{I^2}{2\rho I_{O_z}} \left[ \frac{H^2}{2} - \frac{2mgR}{P} \sin \alpha \right]^2. \quad (5.13)$$

The potential energy available for rotation up to the critical rotation  $\alpha$  can be expressed as

$$PE = mgR \int_0^\alpha \sin(\alpha - \theta) d\theta = mgR(1 - \cos \alpha) = mg \left( R - \frac{H}{2} \right). \quad (5.14)$$

Equating Eqs. (5.13) and (5.14), the critical impulse required to topple the wall can be calculated as

$$I_{crit} = \frac{2P \sqrt{2\rho I_{O_z} mg \left( R - \frac{H}{2} \right)}}{PH^2 - 4mgR \sin \alpha}. \quad (5.15)$$

Eq. (5.15) is not very sensitive to the chosen peak pressure value. When the pressure is doubled, the critical impulse decreases by less than 0.1 % for a two course Mil 3 wall. For engineering purposes, the peak pressure value can be arbitrarily chosen as the uppermost pressure value on the  $P$ – $I$  curve. For a perfectly impulsive load of a finite impulse

but infinitesimal time duration and infinite peak pressure, the second term in the denominator becomes negligibly small compared to the first term, and Eq. (5.15) reduces to

$$I_{crit} = \frac{2}{H^2} \sqrt{2\rho I_{Oz} mg \left( R - \frac{H}{2} \right)}. \quad (5.16)$$

The pressure-dominated solution is derived based on assuming that the impulse and time duration of the blast loading is infinite. The blast loading time history approaches an ideal step pressure load. Considering a resisting moment as a function of angle  $\theta$  at any time, i.e.

$$M_{res} = mgR \sin(\alpha - \theta), \quad (5.17)$$

where  $M_{res}$  is a resisting moment and is a function of the geometry and time-dependent rotation. Note that this function starts at an initial moment resistance ( $\theta = 0$ ) and decreases as the rotation  $\theta$  increases. For any moment applied from an ideal step-pressure load that is less than the initial moment resistance of the wall, the wall will not incur any motion. If the moment applied by the peak pressure ideal step load is slightly greater than the moment resistance of the wall, the wall will tip over entirely. There is no solution for an ideal step pressure loading that will lead to a maximum rotation that lies between zero rotation and complete overturning. Therefore, this critical ideal step pressure wave value can be solved for by equating the moment caused by the applied ideal step pressure to the initial moment resistance of the wall as

$$\frac{H^2}{2} p_{step} = mgR \sin \alpha. \quad (5.18)$$

The value of ideal step pressure  $p_{step}$  that will cause overturning, defined as  $p_{stepcrit}$ , is given as

$$p_{stepcrit} = \frac{2mgR}{H^2} \sin \alpha . \quad (5.19)$$

Note that the same solution for deriving the ideal step loading asymptote will result from using the method presented in Appendix G. Since the resistance to an applied pressure continuously decreases with increasing  $\theta$ , the peak value for the cumulative mean resistance between the interval  $0 \leq \theta \leq \alpha$  occurs at  $\theta = 0$ , and is exactly equal to the initial resistant pressure. Thus the critical ideal step pressure is equal to the initial resistant pressure. This is a special case in comparison with other structures which typically offer greater resistance in response to increased deflection or deformation.

To calculate the time history of response of the model to different pressure-time histories, the non-linear governing equation of motion, Eq. (5.9), was coded in Visual Basic using the Runge–Kutta technique in solving a non-linear equation. A time step of 0.01 *ms* was selected for the program based on the convergence of time histories of rotation achieved at time steps of 0.01 *ms* or smaller.

## 5.2 A Rigid-Body Hybrid model

This model was derived to provide an efficient analytical model which improves upon the previous Rigid-Body Rotation model. In formulating a more accurate model, additional observations were made concerning the modes of deformation incurred by the HB walls. Since excess dust and debris raised by the blasts in the experiments hindered the ability to

obtain visual stills of the deformation through high-speed video, the deformation of the FE model was used to study the mechanisms of response and to gain insight so that a suitable analytical model could be proposed.

### 5.2.1 Response mechanism from the FE model

The deformation from the FE model is shown in Figure 5.2. The primary mechanism of deformation is the Rigid-Body Rotation of the HB wall. The corner shear and compression are also important because they decrease the horizontal distance between the centre of gravity ( $cg$ ) and the point of rotation. The distribution of base pressure with an equivalent force  $F_n$  and the base friction  $F_s$  are shown in the figure.

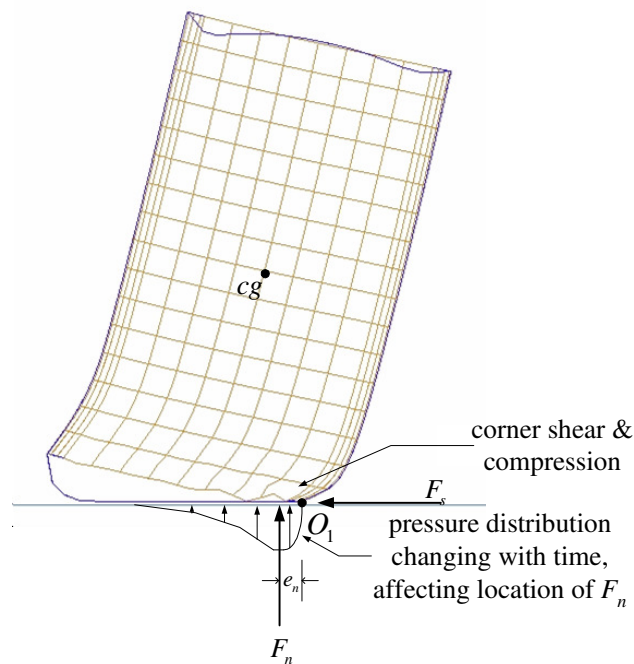


**Figure 5.2 Deformed shape of finite element model and basic formulation of analytical model**

The compressibility of the soil influences the magnitude of the resulting equivalent force  $F_n$  and its location  $e_n$ . The density and the slope of the yield relationship are influential soil parameters contributing to the response of soil-filled walls.

### 5.2.2 Assumptions in the formulation of the model

Based on the deformation from the FE model, the following assumptions were made in formulating the proposed model:

1. The wall can be modelled adequately using the following three mechanisms: rigid-body rotation, compression and shear near the corner.
2. The ground is assumed to be rigid.
3. Only two-dimensional behaviour is considered, where a simple free standing wall is loaded uniformly along the length and height of the wall. The bulges in the walls that occur after filling are accounted for in the calculation of the overall mass and rotational inertia, but their effect in adding strength to the shear deformation is ignored. The model is formulated from the point of reference of the unexpanded width or inner corner for the deformation. This assumption is based on the fact that the geotextile folds underneath each unit and at the bottom the wall is constrained from expanding when filled due to the geotextile.
4. The effect of any local inertia arising from local deformations and accelerations, either from the shear or compression at the base, is assumed to be negligible. Only the forces arising from the resistance to local deformation at the bottom are calculated.



5. The change in shape due to the local deformations of shear and compression at the base and corner is not great enough to sufficiently change the rotary inertial properties of the wall.
6. The compression, pressure distribution and the location of the resulting force normal to the ground can be modelled by assuming the bottom of the wall acts as Winkler foundation resting on rigid ground, with plastic compressive properties governed by the soil Equation of State.
7. The shear yield stress is a function of the normal or compressive stress at the base, and can be calculated using the Mohr-Coulomb relationship. The shear stress-strain relationship is assumed to be perfectly plastic.
8. For the range of interest of the rotation, the normal compression of the Winkler base of the wall is assumed to act independently of the shear displacement. The normal pressure distribution at the base is calculated by considering the compression of the Winkler base, and the distribution of compression is only affected by the vertical force and rotation angle of the wall and not the shear deformation.
9. Although it is possible for the entire wall to slide, shearing to take place within the wall or a combination of both, due to the high resistance against sliding because the welded wire mesh digs into the ground at the corner of the wall it is assumed that no sliding takes place. Thus point  $O_1$  shown in Figure 5.2 is assumed to be fixed.

To gain a better understanding of the local deformation model proposed, consider a soil wall subjected to a corner deformation at any time  $t$  as shown in Figure 5.3 (a). The dis-

placement coordinates are in the rotated position of the wall. Assume that the  $cg$  is fixed from both the translations and rotations about the  $cg$ . The body is considered rigid, with the exception of the area near the compressed corner. Point  $O$  translates to  $O_1$ . The resulting components of the normal pressures and traction pressures (shear pressures) in the rotated coordinates are  $F_u$  and  $F_v$ , located at the distances  $e_v$  and  $e_u$  from the corner  $O_1$ , respectively. Here the corner undergoes displacements  $u$  and  $v$ . Assume that the deformation around the corner measured by displacements  $u$  and  $v$  is not subjected to large inertial forces that would otherwise be stated as functions of the second time derivative of these displacements. Only static resistance of the localized corner deformation is considered.

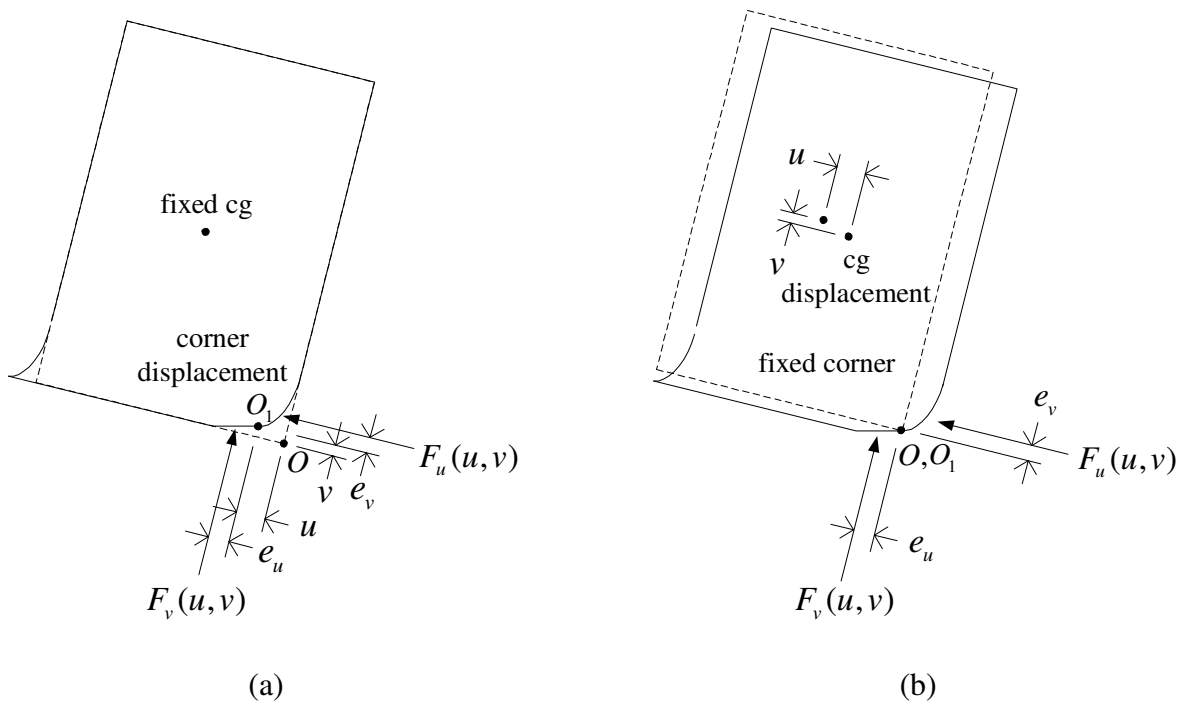


**Figure 5.3** Diagrams illustrating analytical model formulation: (a) assuming fixed  $cg$  and corner displacements, (b) assuming fixed corner and  $cg$  displacements

Alternatively, for the proposed analytical model, instead of considering that the body being fixed with respect to the  $cg$ , assume that the corner is fixed at location  $O_1$ , as shown in Figure 5.3 (b). Under the same reaction forces  $F_u$  and  $F_v$ , the entire body moves equal and opposite to the deformations incurred at the corner. The  $cg$  translation from the corresponding position in an undeformed body, shown in the dotted line in the figure, is a direct translation of the corner deformations. Assume that the inertial resistance to displacements  $u$  and  $v$  is approximately equal to the inertial resistance of the undeformed body. Also assume that any interaction of the corner with an arbitrarily shaped rigid surface can be resolved into and sufficiently modelled by using these equivalent forces and locations.

### 5.2.3 Derivation of equations of motion

A free-body diagram of the model in Figures 5.3 (a) and (b) is shown in Figure 5.4 and is used to derive the equations of motion for the free standing wall subjected to a uniformly applied time history of blast pressure  $p(t)$ . In the figure, thick solid arrows denote all forces and pressures acting on the body, while double-headed arrows denote distances and arrows mark displacements from the point of reference indicated. The wall has a height  $H$  and a width  $w$ . The wall in its initial configuration is outlined in the dashed-dotted line. The centre of gravity of the wall is at  $cg_0$  in its initial position. The centre of the applied blast pressure will be assumed to travel directly through the  $cg$  at all times. Despite the change in height from the deformation  $v$ , it is assumed that the total force of the pressure distribution at the base will be conserved and act vertically. After the wall is

loaded, it undergoes a rotation  $\theta$ . The light dotted line represents the equivalent position of the rotated undeformed wall. The centre of gravity of the wall at this position is at  $cg_1$ . The corner at point  $O_1$  is fixed; however, the body undergoes local deformations,  $u$  and  $v$ , which are measured parallel to the width and height, respectively. These corner deformations result in a direct translation of the location of the centre of gravity from  $cg_1$  to  $cg$ , shown in the figure. The displacement of the centre of gravity from  $cg_0$  to  $cg$  is represented by the displacement components  $U$  and  $V$  in the horizontal and vertical directions, respectively. The parameters  $\ddot{U}$  and  $\ddot{V}$  represent the second time derivatives of  $U$  and  $V$ , respectively.  $m$  denotes the averaged planar mass per unit length of the wall along a single column and  $g$  the gravitational acceleration. The density of the wall is  $\rho$  and the rotational second moment of area about the centre of gravity is  $I_{cg}$ .

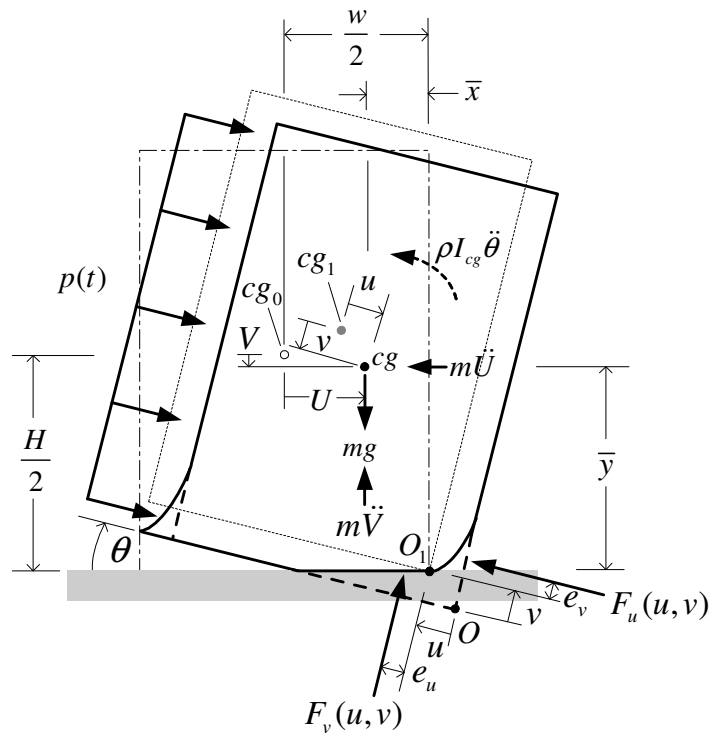


Figure 5.4 Free-body diagram for derivation of the equations of motion

The translational equations of motion in the horizontal and vertical directions and the rotational equation of motion about the  $cg$  are, respectively

$$p(t)H \cos \theta - F_u(u, v) \cos \theta - m\ddot{U} + F_v(u, v) \sin \theta = 0, \quad (5.20)$$

$$p(t)H \sin \theta - F_u(u, v) \sin \theta - m\ddot{V} - F_v(u, v) \cos \theta + mg = 0, \text{ and} \quad (5.21)$$

$$\rho I_{cg} \ddot{\theta} - F_u(u, v) \left( \frac{H}{2} - v - e_v \right) + F_v(u, v) \left( \frac{w}{2} - u - e_u \right) = 0. \quad (5.22)$$

To obtain the equations of motion in terms of the localised corner displacements  $u$  and  $v$ , it is first necessary to relate these to centre of gravity horizontal and vertical displacements,  $U$  and  $V$ .

$$U = \frac{w}{2} - \bar{x}, \text{ and} \quad (5.23)$$

$$V = \frac{H}{2} - \bar{y}; \quad (5.24)$$

where  $\bar{x}$  and  $\bar{y}$  are given as

$$\bar{x} = \left( \frac{w}{2} - u \right) \cos \theta - \left( \frac{H}{2} - v \right) \sin \theta, \text{ and} \quad (5.25)$$

$$\bar{y} = \left( \frac{w}{2} - u \right) \sin \theta + \left( \frac{H}{2} - v \right) \cos \theta. \quad (5.26)$$

Substituting Eqs. (5.25) and (5.26) into Eqs. (5.23) and (5.24) and taking the second derivative of  $U$  and  $V$  with respect to time yields

$$\ddot{U} = \ddot{\theta} \bar{y} + (\dot{\theta})^2 \bar{x} + \ddot{u} \cos \theta - \ddot{v} \sin \theta - 2\dot{\theta}(\dot{u} \sin \theta + \dot{v} \cos \theta), \text{ and} \quad (5.27)$$

$$\ddot{V} = -\ddot{\theta} \bar{x} + (\dot{\theta})^2 \bar{y} + \ddot{u} \sin \theta + \ddot{v} \cos \theta + 2\dot{\theta}(\dot{u} \cos \theta - \dot{v} \sin \theta). \quad (5.28)$$

Substitution of Eqs. (5.27) and (5.28) in the equations of motion, Eqs. (5.20) to (5.22), gives

$$m\bar{y}\ddot{\theta} + m\ddot{u} \cos \theta - m\ddot{v} \sin \theta = RHS_u, \quad (5.29)$$

$$m\bar{x}\ddot{\theta} - m\ddot{u} \sin \theta - m\ddot{v} \cos \theta = RHS_v, \text{ and} \quad (5.30)$$

$$\rho I_{cg} \ddot{\theta} = RHS_\theta; \quad (5.31)$$

where  $RHS_u$ ,  $RHS_v$ , and  $RHS_\theta$  are defined by

$$RHS_u = -m\bar{x}(\dot{\theta})^2 + 2m\dot{\theta}(\dot{u} \sin \theta + \dot{v} \cos \theta) + (p(t)H - F_u(u, v)) \cos \theta + F_v(u, v) \sin \theta, \quad (5.32)$$

$$RHS_v = m\bar{y}(\dot{\theta})^2 + 2m\dot{\theta}(\dot{u} \cos \theta - \dot{v} \sin \theta) - (p(t)H - F_u(u, v)) \sin \theta + F_v(u, v) \cos \theta - mg, \text{ and} \quad (5.33)$$

$$RHS_\theta = F_u(u, v) \left( \frac{H}{2} - v - e_v \right) - F_v(u, v) \left( \frac{w}{2} - u - e_u \right). \quad (5.34)$$

For convenience in applying the Runge-Kutta numerical integration technique for the above non-linear differential equations, the accelerations can be isolated from the system of equations as

$$\ddot{u} = \frac{RHS_u \cos \theta}{m} - \frac{RHS_v \sin \theta}{m} + \frac{RHS_\theta}{\rho I_{cg}} (\bar{x} \sin \theta - \bar{y} \cos \theta), \quad (5.35)$$

$$\ddot{v} = -\frac{RHS_u \sin \theta}{m} - \frac{RHS_v \cos \theta}{m} + \frac{RHS_\theta}{\rho I_{cg}} (\bar{x} \cos \theta + \bar{y} \sin \theta), \text{ and} \quad (5.36)$$

$$\ddot{\theta} = \frac{RHS_\theta}{\rho I_{cg}}. \quad (5.37)$$

Note that all parameters within the equations of motion can be calculated thus far, except for  $F_u(u, v)$  and  $F_v(u, v)$  and corresponding locations  $e_u$  and  $e_v$ , which are to be calculated for given deformations  $u$  and  $v$  using the local deformation model as discussed in the following section.

## 5.2.4 Reverse Winkler formulation

### 5.2.4.1. Plastic and elastic spring properties

In order to incorporate the base compression into the model, the base of the wall with continuous soil compression properties in Figure 5.5 (a) is modelled by Winkler springs having the discrete spring constants as shown in Figure 5.5 (b). Since the base of the wall is modelled with Winkler continuous springs, while the ground is assumed rigid, the formulation in the title of this section is termed *reverse* Winkler. Note that these springs are constrained to compressive stresses only and tensile stresses are set to zero if tensile strains occur. The idealized relationship between pressure and volumetric strain of the soil in compression is shown in Figure 5.5 (c). The compressive strains are assumed not to be large enough for the relationship to become non-linear. Any loading to higher than previously encountered levels of loading occurs along the slope designated by  $K_v$  while any unloading and reloading that is lower than previously encountered levels occurs along the slope designated by  $K$ . The equivalent Winkler spring constants  $k_v$  and  $k$ , shown in Figure 5.5 (d), must be obtained from the EOS of the bulk modulus of the soil.

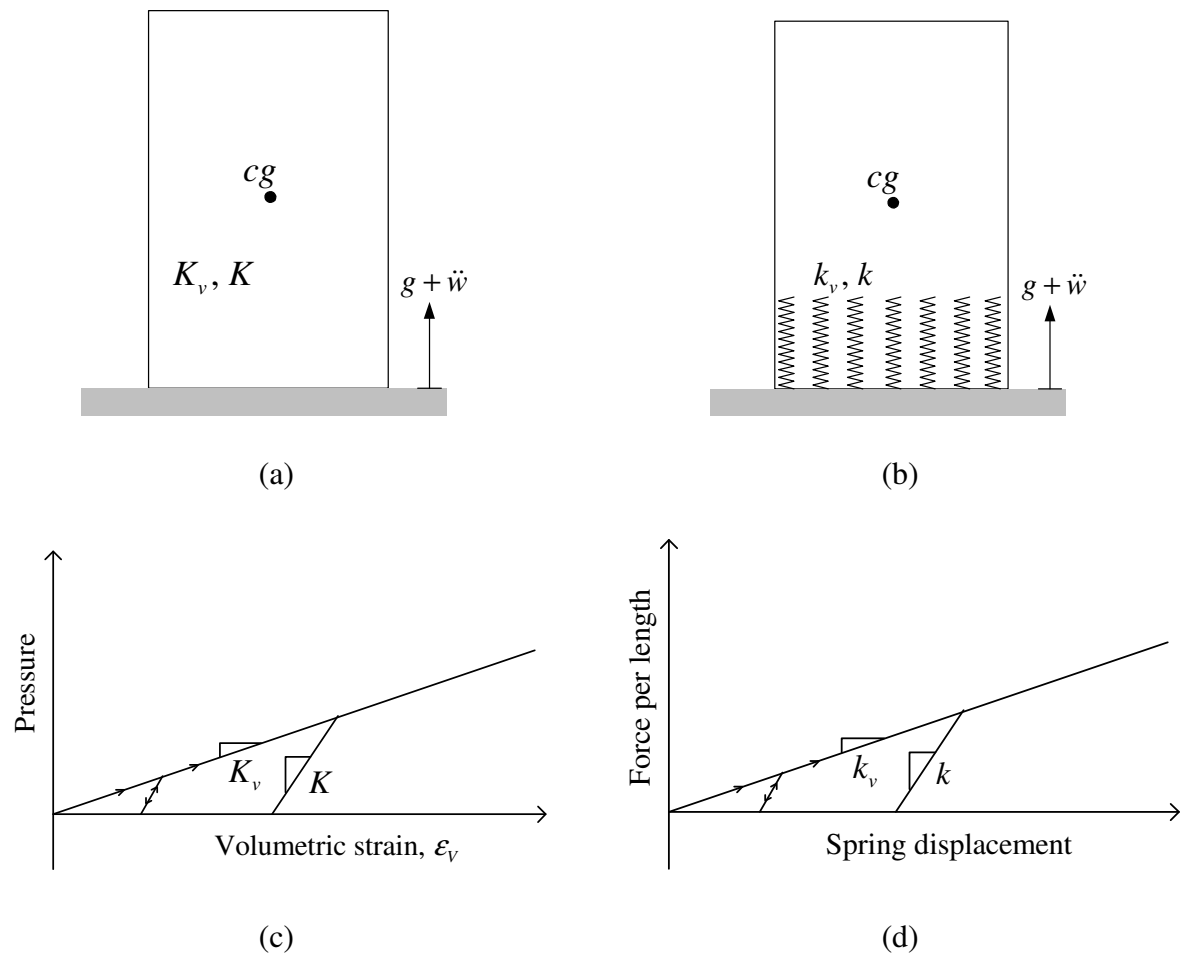


**Figure 5.5 Reverse Winkler foundation: (a) wall with soil having continuous compression properties, (b) wall with soil having equivalent spring displacement properties, (c) relationship for pressure as a function of volumetric strain, and (d) relationship for distributed force as a function of spring displacement**

To calculate  $k_v$  from  $K_v$  and  $k$  from  $K$ , consider a wall with continuous soil properties resting on a rigid foundation in Figure 5.6 (a). Under the application of the gravitational acceleration and an arbitrary ground acceleration  $g + \ddot{w}$ , the top of the wall undergoes a vertical displacement  $\delta_{tot}$  calculated from the static application of  $g + \ddot{w}$  as shown in Figure 5.6 (b). The overall height of the wall changes from  $H$  to  $H'$ . The centre of grav-



ity is displaced from its initial position  $cg$  by an amount  $\Delta_{cg}$  to its new position at  $cg'$ , which results from both the decrease in height and the increase in density. The distribution of vertical stress, vertical strain, and density along the height of the wall are shown in Figures 5.6 (c), (d) and (e), respectively. Note that the vertical stress and strain are functions related to its undeformed configuration, while the density function relates to the deformed configuration. Variables  $p_b$ ,  $\varepsilon_b$ , and  $\rho_b$  represent the pressure, strain, and density at the base of the wall, respectively. Parameter  $\rho$  is the density at the top of the wall, which is equal to the density of the soil in its unloaded state. Assuming that wall is thick enough that the volumetric strain deformation due to the vertical stresses only takes place in the vertical direction, and horizontal strains are negligible, the pressure and strain along the height can be given as

$$p(s) = \rho(g + \ddot{w})s, \text{ and} \quad (5.38)$$

$$\varepsilon(s) = \frac{\rho(g + \ddot{w})s}{K_v}; \quad (5.39)$$

where  $s$  is measured from the top of the undeformed wall. The strain distribution can be integrated along the height to calculate the total displacement  $\delta_{tot}$  as

$$\delta_{tot} = \int_0^H \varepsilon(s) ds = \int_0^H \frac{\rho(g + \ddot{w})s}{K_v} ds = \frac{\rho(g + \ddot{w})H^2}{2K_v}. \quad (5.40)$$

The resulting height  $H'$  can be calculated as

$$H' = H - \delta_{tot}. \quad (5.41)$$

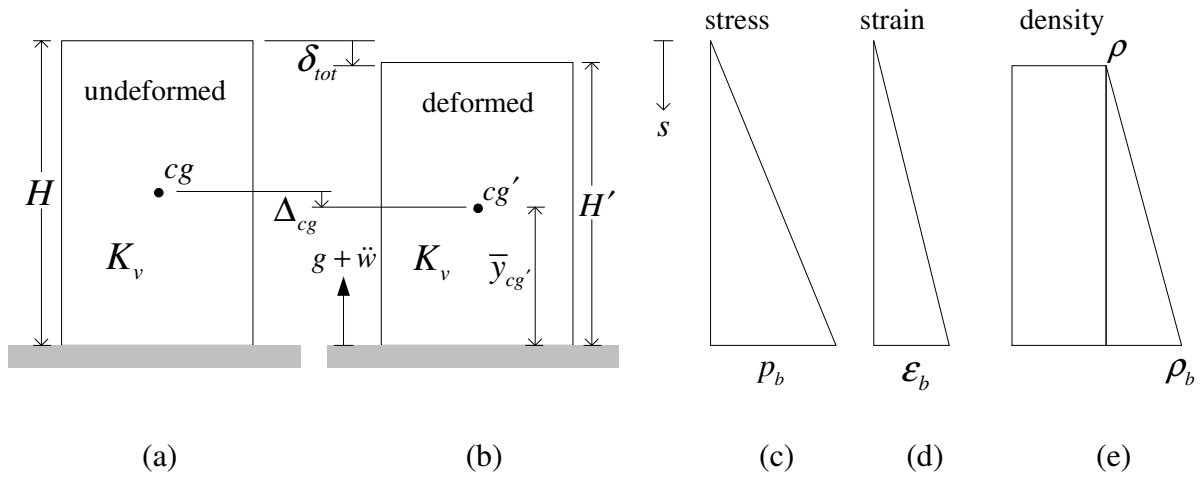


Figure 5.6 Calculation setup for equating  $K_v$  to  $k_v$

The pressure  $p_b$  and strain  $\epsilon_b$  at the base of the wall can be given as

$$p_b = \rho(g + \ddot{w})H, \text{ and} \quad (5.42)$$

$$\epsilon_b = \frac{\rho(g + \ddot{w})H}{K_v}. \quad (5.43)$$

The density at the base of the wall  $\rho_b$  can be calculated based on the strain at the base as

$$\rho_b = \frac{\rho}{1 - \epsilon_b}. \quad (5.44)$$

The change in position of the centre of gravity can be expressed by

$$\Delta_{cg} = \frac{H}{2} - \bar{y}_{cg'}, \quad (5.45)$$

where  $\bar{y}_{cg'}$  can be calculated from the density distribution as

$$\bar{y}_{cg'} = \frac{\frac{(H')^2}{2}\rho + \frac{(H')^2}{6}(\rho_b - \rho)}{H'\rho + \frac{H'}{2}(\rho_b - \rho)}. \quad (5.46)$$

Substituting Eqs. (5.41) and (5.44) into the above equation and simplifying the result yields

$$\bar{y}_{cg'} = \frac{(H - \delta_{tot})}{3} \frac{3 - 2\varepsilon_b}{2 - \varepsilon_b}. \quad (5.47)$$

With the use of Eqs. (5.40) and (5.43), Eq. (5.47) becomes

$$\bar{y}_{cg'} = \frac{H}{6} \left[ 3 - \frac{2\rho(g + \ddot{w})H}{K_v} \right]. \quad (5.48)$$

Therefore, Eq. (5.45) gives

$$\Delta_{cg} = \frac{H^2 \rho(g + \ddot{w})}{3K_v}. \quad (5.49)$$

Given that  $k_v$  relates pressure at the base to displacement of the  $cg$ ,  $k_v$  can be found as

$$k_v = \frac{p_b}{\Delta_{cg}} = \frac{3K_v H \rho(g + \ddot{w})}{H^2 \rho(g + \ddot{w})} = \frac{3K_v}{H}. \quad (5.50)$$

Under the same assumption,

$$k = \frac{3K}{H}. \quad (5.51)$$

Note that no loading rate effects are included in the calculation of stresses from strains in the soil.

#### 5.2.4.2. Deformed configuration of lower portion of wall

Figure 5.7 (a) shows the lower portion of the wall in its deformed configuration. As previously defined, point  $O$  represents location of the corner in the corresponding undeformed shape, while point  $O_1$  represents the corner in its fixed position. Displacement  $u$

and  $v$  in the rotate coordinates relate  $O$  to  $O_1$ . Interaction of the Winkler spring with the rigid ground results in a nominal contact distance  $O_1C$ . The displacement of the distributed spring in the reverse Winkler foundation is given by triangle  $PO_1C$ . A normal stress distribution  $f_n$  results from this displacement. The resultant force of this distributed normal force is  $F_n$  and its location is  $e_n$  referenced from point  $O_1$ . The shear stress  $f_s$  acting along the width of the portion of the wall near the ground at the contact interface at ground level can be calculated from  $f_n$  using the Mohr-Coulomb relationship for the soil. The resultant of  $f_s$  over the distance  $O_1C$  is  $F_s$ . Note that  $F_n$  and  $F_s$  intersect at point  $D$ , which can be transformed at this location to forces  $F_v$  and  $F_u$  in the rotated coordinates, shown in Figures 5.3. The side of the wall to the right of point  $O_1$ , which was initially vertical but has since undergone significant shear, is assumed to maintain an angle that is greater than zero when measured from horizontal reference and thus does not interact with the ground. This assumption is valid in the initial time history of movement, but as the wall undergoes very large rotations in excess of its critical amount of rotation for overturning, this assumption may begin to lose its validity. However, this assumption is considered reasonable for the portion of movement up to critical overturning. Consider at this instant in time that the hatched portion of the triangle to the right of point  $E$  is undergoing displacement that is higher in magnitude than previously encountered and is therefore in a state of loading. The area of the triangle to the left of point  $E$  is undergoing displacement that is less than the highest previously encountered and is therefore in a state of unloading. Assume that the area between point  $E$  and  $F$  is in a state of unload-

The graph shows a linear relationship between distributed spring force and vertical spring displacement. The vertical axis is labeled 'distributed spring force' and the horizontal axis is labeled 'vertical spring displacement'. A line with a positive slope starts from the origin. Points C, F, E, and D are marked on the line. The vertical displacement from the origin to point E is labeled  $n_0$ , and the total vertical displacement to point D is labeled  $n_{\max}$ . The slope of the line is indicated by a triangle with sides  $k$  and  $k_v$ . The points are labeled  $C$ ,  $F$ ,  $E, \hat{E}$ , and  $D, \hat{D}$ .

(b)

These points of interest listed in Figure 5.7 (a) are plotted on the distributed spring force-displacement plot in Figure 5.7 (b). Note that compressive spring force is assumed positive. The point  $F$  shows the current spring displacement, while point  $\hat{F}$  denotes the highest displacement experienced with reference to the vertical direction. This notation is

used for all other points of interest listed. As the wall rotates, point  $C$  is compressed from the origin along slope  $k_v$  until it reaches point  $\hat{C}$ . When the wall rotates more, this point is unloaded along slope  $k$ . Due to the zero tension admissible at the interface, this point is lifted off the ground. Note that these highest points are always referenced to the vertical direction, and directly referenced to the displacement plane surpassing all previous displacement planes at a given location.

To calculate the stress distribution at the base, it is necessary to solve for the locations of points  $C$ ,  $E$ , and  $F$  from the time-dependent variables defining the deformed configuration ( $u$ ,  $v$ , and  $\theta$ ) for each time step. As shown in Figure 5.8, for a given rotation  $\theta$  and a given displacement  $v$ , point  $C$  along  $r$  can be calculated as

$$r_C = \min \left\{ \frac{v}{\tan \theta}, w \right\}. \quad (5.52)$$

The locations of points  $E$  and  $F$  can be determined analytically and the analytical solutions are presented in Appendix I. The analytical solution for point  $E$  is simple to implement in the computer code but the analytical solution for point  $F$  is very cumbersome. Both analytical solutions require the rotation to be positive and increasing and cause critical errors if the wall begins to rotate backwards after reaching maximum rotation. Therefore the numerical solutions elaborated in the following subsections are used instead to locate points  $E$  and  $F$ . These numerical solutions are proven to provide the same results but are stable when rotation decreases after reaching maximum.

### 5.2.4.3. Locating point $E$

In Figure 5.8, thin dotted lines represent previous planes of displacement encountered at lesser magnitudes and at earlier times, assuming that the wall positively rotates up until its maximum rotation. Note that as explained earlier, the shear deformation is assumed not to affect the compression of the Winkler foundation at the base, and therefore the diagram was drawn without showing shear deformation. Each of these dotted lines represents a previous displacement plane at an instant of time. In the case of continuous time, there is an infinite number of past displacement planes. The dashed line represents the highest previous displacement encountered at any point on the base along the thickness. This dashed line is a collection of the upper most segments of all previous displacement planes, and is defined along  $r$  by line  $q_{\max}(r)$ . Line  $O_1C$  represents the present displacement plane and is defined by  $q(r)$ , given by

$$q(r, t) = v(t) - r \tan \theta. \quad (5.53)$$

Point  $E$  represents the point of intersection between the maximum previous displacements and the present displacement plane. In order to locate point  $E$ , an approximate method is used in this study. The step-by-step procedure is as follows:

1. Check the present displacement plane  $q(r)$  with the maximum displacements

$q_{\max}(r)$ , incrementing along  $r$  to find the point of crossover.

2. Linearly interpolate between the two discrete points on either side of the crossover, (i.e.  $r_{i-1}$  and  $r_i$ ) to find a more precise intersection of the two lines, where the intersection in terms of coordinate  $r$  is defined as  $r_E$  as follows:

$$r_E = r_{i-1} + \frac{[q_{\max}(r_{i-1}) - q(r_{i-1})]}{[q(r_i) - q(r_{i-1}) - q_{\max}(r_i) + q_{\max}(r_{i-1})]} [r_i - r_{i-1}]. \quad (5.54)$$

3. Update the maximum displacement  $q_{\max}(r_i)$  to be used in the next time step by replacing  $q_{\max}(r_i)$  where it was exceeded by the present displacement plane  $q(r_i)$ .

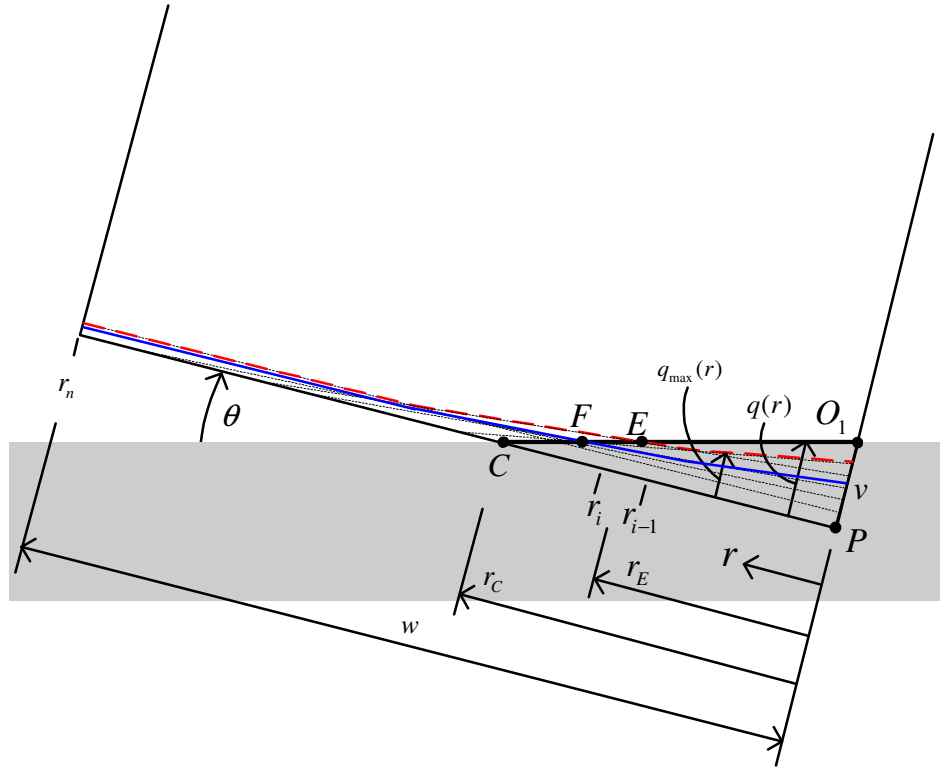


**Figure 5.8** Locating points  $C$ ,  $E$ , and  $F$  by finding intersection of present displacement plane (line  $O_1C$ ) with line of maximum displacement (dashed line), and line of zero stress (solid line)

#### 5.2.4.4. Locating point $F$

It is useful for upcoming analyses to define a coefficient  $\lambda$  which gives the ratio of zero stress displacement to maximum experienced displacement based on the slopes of the loading and unloading constants of the spring.



$$\lambda = \frac{n_0}{n_{\max}} = \frac{k - k_v}{k}. \quad (5.55)$$

Note that the displacements  $n_0$  and  $n_{\max}$ , shown in Figure 5.7 (b), can be taken for any point, and because of the linear relationship of the spring force-displacement relationship assumed,  $\lambda$  remains constant. In the case of  $\lambda = 1$ , the soil is perfectly plastic and all deformation is permanent. In this case, variable  $k$  would be assumed as infinity. In the case of  $\lambda = 0$ , the soil is perfectly elastic, where the unloading and loading spring coefficients are equal to one another.

In Figure 5.8, the solid line represents the location of where the present displacement plane would have to be for zero stress to occur due to unloading. This line can be calculated by multiplying the vertical distance  $n$  shown from the bottom to the solid line,  $q_{\max}(r)$ , by  $\lambda$ . Point  $F$  represents the intersection of this line with the present displacement plane,  $q(r)$ . The physical meaning of this point is that it is the division between the portion of the base to the right of point  $F$ , which is compressed and is in a state of unloading, and the portion to the left of point  $F$ , which is at zero stress, where contact with the ground is not made any more due to the plastic compression at a previous time period. For the diagram in Figure 5.8, the solid line is drawn for approximately  $\lambda = 2/3$ . The methodology that was used in the previous section to locate point  $E$  was also used to locate point  $F$ , but owing to the assumption that the unloading distance is measured vertically, the interpolation formula for the intersection was adjusted for the given angle  $\theta$  as follows:

$$r_F = \hat{r}_{i-1} + \frac{[\lambda q_{\max}(r_{i-1}) - q(\hat{r}_{i-1})]}{\{[q(\hat{r}_i) - \lambda q_{\max}(r_i)] - [q(\hat{r}_{i-1}) - \lambda q_{\max}(r_{i-1})]\}} [\hat{r}_i - \hat{r}_{i-1}], \quad (5.56)$$

where

$$\hat{r}_i = r_i - [1 - \lambda] q_{\max}(r_i) \tan \theta, \text{ and} \quad (5.57)$$

$$\hat{r}_{i-1} = r_{i-1} - [1 - \lambda] q_{\max}(r_{i-1}) \tan \theta. \quad (5.58)$$

#### 5.2.4.5. Calculation of stresses and forces

Once the distances  $r_C$ ,  $r_E$  and  $r_F$  have been derived, the base pressure, total reaction force  $F_n$  and its location  $e_n$  can be calculated. Consider the diagram in Figure 5.9.

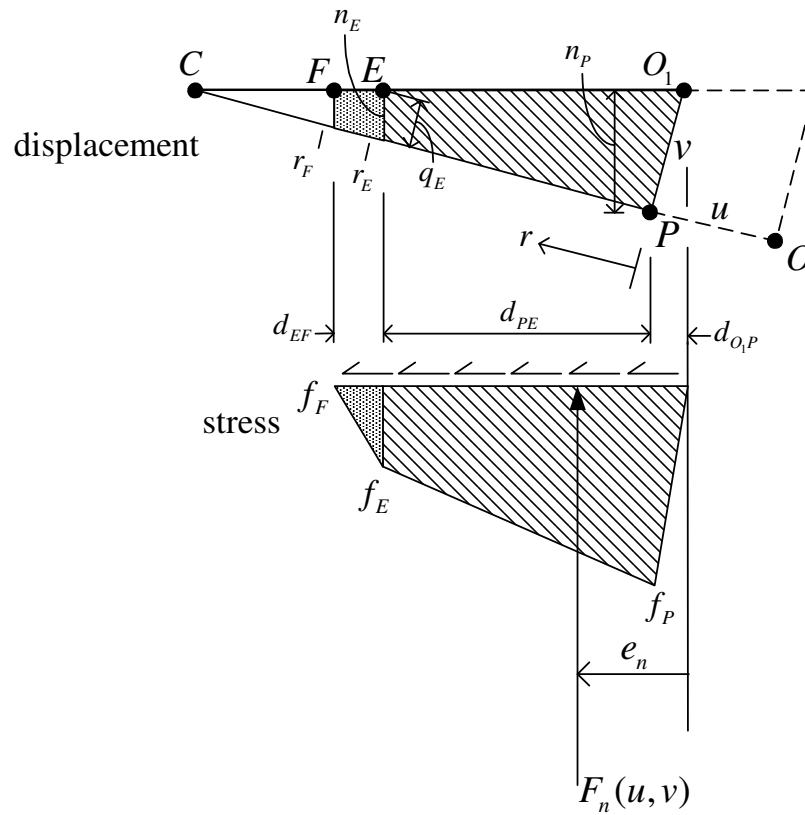


Figure 5.9 Calculation of base pressure, equivalent reaction force, and location

The distances  $d_{O_1P}$ ,  $d_{PE}$ , and  $d_{EF}$  between  $O_1$  and  $P$ ,  $P$  and  $E$ , and  $E$  and  $F$  can be calculated, respectively, as

$$d_{O_1P} = v \sin \theta, \quad (5.59)$$

$$d_{PE} = \frac{r_E}{\cos \theta} - v \sin \theta, \text{ and} \quad (5.60)$$

$$d_{EF} = \frac{r_F - r_E}{\cos \theta}. \quad (5.61)$$

The normal spring displacements,  $n_P$ ,  $n_E$ , and  $n_F$ , at points  $P$ ,  $E$ , and  $F$  can be calculated, respectively, as

$$n_P = v \cos \theta, \quad (5.62)$$

$$n_E = \frac{q_E}{\cos \theta} = \frac{v - r_E \tan \theta}{\cos \theta}, \text{ and} \quad (5.63)$$

$$n_F = \frac{q_F}{\cos \theta} = \frac{v - r_F \tan \theta}{\cos \theta}. \quad (5.64)$$

The normal force per unit length  $f_n$  at locations  $P$ ,  $E$ , and  $F$  are, respectively,

$$f_P = k_v n_P, \quad (5.65)$$

$$f_E = k_v n_E, \text{ and} \quad (5.66)$$

$$f_F = k_v n_F. \quad (5.67)$$

The total normal force  $F_n$  can be calculated as

$$F_n = \frac{1}{2} f_P d_{O_1P} + \frac{1}{2} (f_P + f_E) d_{PE} + \frac{1}{2} (f_E + f_F) d_{EF}. \quad (5.68)$$

The location of the normal force with respect to point  $O_1$ , namely  $e_n$ , can be calculated as

$$e_n = \frac{1}{F_n} \left\{ \frac{1}{2} f_P d_{O_1P} \left[ \frac{2}{3} d_{O_1P} \right] + f_E d_{PE} \left[ d_{O_1P} + \frac{1}{2} d_{PE} \right] + \frac{1}{2} (f_P - f_E) d_{PE} \left[ d_{O_1P} + \frac{1}{3} d_{PE} \right] \right. \\ \left. + f_F d_{EF} \left[ d_{O_1P} + d_{PE} + \frac{1}{2} d_{EF} \right] + \frac{1}{2} (f_E - f_F) d_{EF} \left[ d_{O_1P} + d_{PE} + \frac{1}{3} d_{EF} \right] \right\} \quad (5.69)$$

#### 5.2.4.6. Derivation of shear displacement relationship

Using the Mohr-Coulomb relationship

$$\tau = c + \sigma_n \tan \phi. \quad (5.70)$$

Integration of Eq. (5.70) over the contact length,  $O_1F$ , yields the relationship between the normal force and the shear force as

$$\int_{O_1}^F \tau(x) dx = \int_{O_1}^F c dx + \tan \phi \int_{O_1}^F \sigma_n(x) dx, \quad (5.71)$$

The integral of the normal stress is equal to the total normal force  $F_n$ . The effect of the cohesion can be evaluated by multiplying the cohesion over the contact length  $O_1F$ .

Thus the above expression can be simplified to calculate the shear force as

$$F_s = c (d_{O_1P} + d_{PE} + d_{EF}) + \tan \phi F_n. \quad (5.72)$$

Once the normal force is calculated, the shear force is evaluated using the above equation. Note that it is assumed that no sliding occurs at the ground surface. Shear is assumed to occur in the portion of the soil in the wall over a very narrow zone near the ground. The direction of the shear force depends on the velocity of the wall at the shear interface. This velocity is calculated using the rigid-body velocity and rotation at the location of  $e_n$ . If the velocity is positive, then it is assumed that shearing takes place and

the shear force  $F_s$  is applied. Consider Figure 5.10, in which the base velocity  $\dot{\chi}$  can be obtained from

$$\dot{\chi} = \dot{U} - \hat{R} \dot{\theta} \cos \left( \tan^{-1} \left( \frac{\bar{x} - e_n}{\bar{y}} \right) \right), \quad (5.73)$$

where the horizontal velocity of the  $cg$ ,  $\dot{U}$ , can be found by taking the first derivative of Eq. (5.23) with respect to time as

$$\dot{U} = \dot{\theta} \bar{y} + \dot{u} \cos \theta - \dot{v} \sin \theta. \quad (5.74)$$

Measurement  $\hat{R}$ , which is the distance from point  $D$  to the  $cg$ , can be found from

$$\hat{R} = \sqrt{(\bar{x} - e_n)^2 + \bar{y}^2}, \quad (5.75)$$

where  $\bar{x}$  and  $\bar{y}$  are given in Eqs. (5.25) and (5.26), respectively. Evaluation of  $\dot{\chi}$  whether positive or negative determines the direction of shear. If the derivative is zero, the shear force is zero.

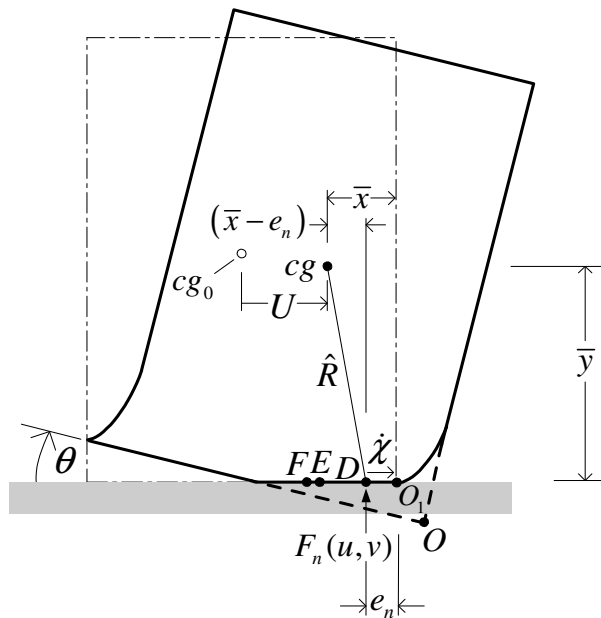


Figure 5.10 Evaluating direction of shear force from horizontal rigid-body velocity at base



### 5.2.5 Calculation of inertial properties about the c.g.

To use the equations of motion presented in subsection 5.2.3, it is necessary to calculate the second moment of area about the centre of gravity  $I_{cg}$  as shown in the diagram in Figure 5.12. The  $cg$  and the origin of the axis are assumed to lie in the geometric centre of a cell. Since  $I_{Oz}$  has already been derived in Section 5.1, the parallel axis theorem can be used to calculate  $I_{cg}$  as

$$I_{cg} = I_{Oz} - \bar{V}R^2, \quad (5.80)$$

where  $I_{Oz}$ ,  $\bar{V}$ , and  $R$  are given in Eqs. (5.6), (5.8), and (5.1), respectively. Substitution of these equations into Eq. (5.80) results in

$$I_{cg} = \frac{w_a H}{12} (w_a^2 + H^2) + \frac{8Hb^3}{9\pi} + \frac{w_a Hb^2}{2} + \frac{Hb}{\pi} (w_a^2 + \frac{H^2}{3}). \quad (5.81)$$

where  $b$  represents the thickness of the bulge in a single sidewall and is given as

$$b = \frac{(w_b - w_a)}{2}, \quad (5.82)$$

One of the assumptions in subsection 5.2.2 was that the local deformations  $u$  and  $v$  are not sufficient enough to sufficiently change the rotational inertial properties of the wall from its initial shape. Therefore it is permissible to use  $I_{Oz}$  derived within the Rigid-Body Rotation model to obtain  $I_{cg}$  to use within the rigid-body hybrid model since the calculation for  $I_{cg}$  is based on a rigid-body assumption, which assumes no changes with corner deformations  $u$  and  $v$ . The change in rotary inertia about the  $cg$  from the largest

of local shear and compressive deformations was investigated in Appendix J and found to be within 1 % of the value for the undeformed shape, hence the affect of these deformations on the rotary inertia were ignored.

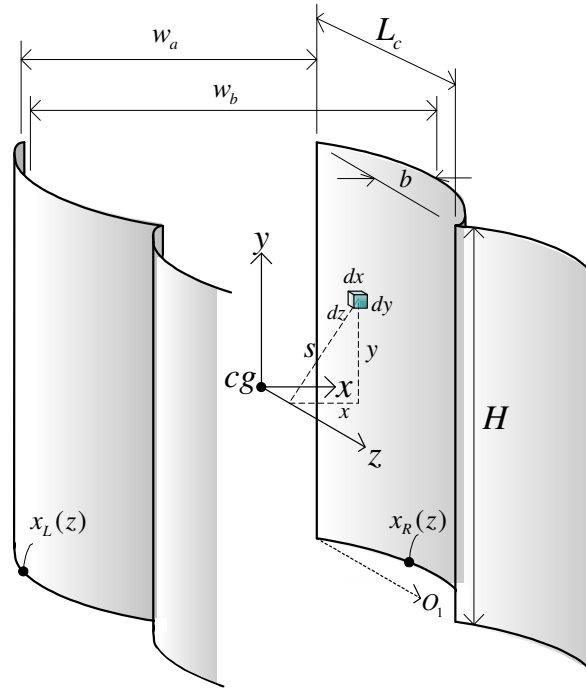


Figure 5.12 Diagram illustrating calculation of inertial properties

### 5.2.6 Discretization

Figure 5.13 (a) shows the vertical displacement-time histories using different time step sizes from Runge-Kutta integration of the Rigid-Body Hybrid model. The same results were achieved using a time step of 0.1 ms and 0.05 ms, and therefore a 0.1 ms time step was used. To determine the appropriate discretization along the thickness in the determination of  $r_E$  and  $r_F$ , the HB wall size and loading in Trial 7 were used. Note that the Mil 1 wall was selected for this investigation because it is thicker than the Mil 3 wall. The



discretization along the  $r$ -axis was chosen to be 5, 10, 20, 50, and 100. Vertical displacement–time histories of the upper monitoring point are shown in Figure 5.13 (b). It can be seen from the figure that the convergence was achieved when the number of discretizations was 50 or more. Using 100 discretizations resulted in less than 0.1 % difference in the displacements in comparison to using 50 discretizations. Thinner walls were also tested and found to converge similarly. Therefore, 50 discretizations along the thickness were selected.

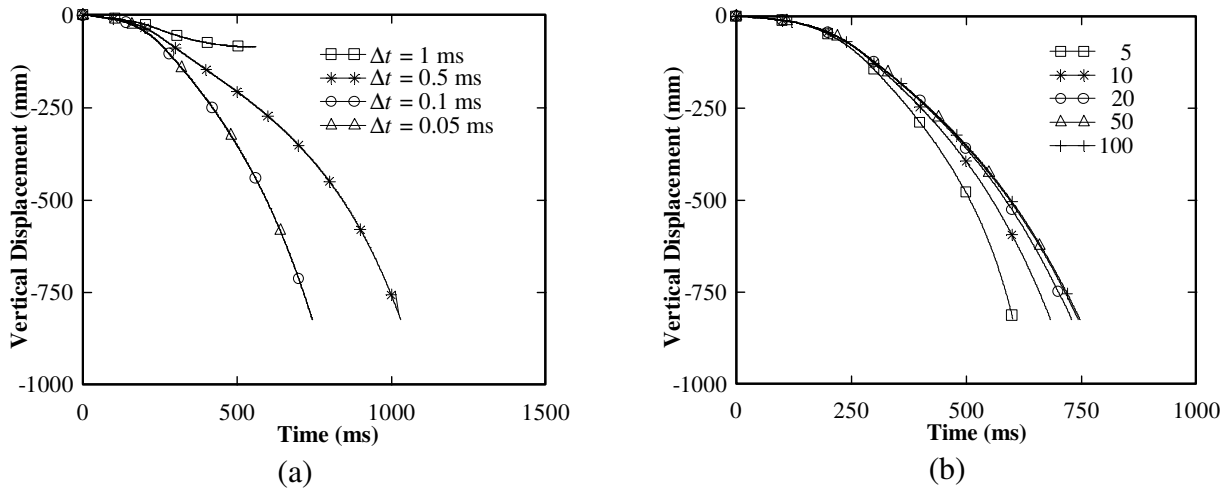


**Figure 5.13** Vertical displacement–time histories; (a) convergence study for time step size, (b) convergence study for number of discretizations along thickness using  $\Delta t = 0.1$  ms

# Chapter 6

## Results and Discussion

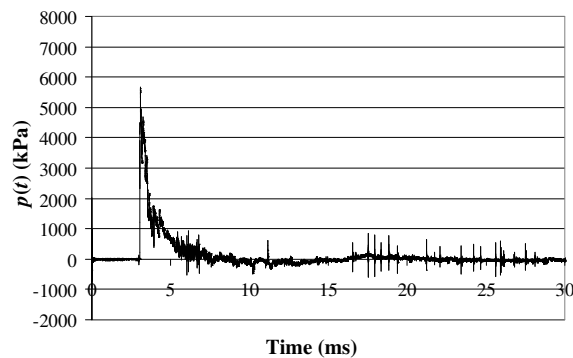
The experiment results, the accuracy assessment of the FE analysis, Rigid-Body Rotation model, and Rigid-Body Hybrid model will be presented in the first four sections of this chapter. The last two sections of the chapter is a comparison of the pressure impulse ( $P-I$ ) curves generated using the analytical models and FE model for the different wall configurations studied.

### 6.1 Experiment results and validations

All HB walls tested consisted of five-column, simple, straight, free-standing walls. In Trials 1 through 3, pressure measurements were taken from a single gauge at the centre span of the wall at approximately mid-height. Only the post-experiment response is available from post-experiment position measurements and photos. In Trials 4 through 7, three pressure gauges, one at mid height at the centre of each of the centre three columns, were used, and displacement–time histories were recorded as detailed in Chapter 3.

### 6.1.1 Trial 1

A two-course Mil 3 wall was tested in Trial 1. The recorded reflected pressure–time history is shown in Figure 6.1 (a), while the post-experiment position of the wall is shown in Figure 6.1 (b). The painted wooden marker was attached to the wall as a visual aid to help observe the time history of rotation of the wall in the high speed video. Unfortunately the rotation–time history in the high speed video could not be observed due to the fireball, dust, and debris raised by the blast. This remained a deficiency for all experiments.



(a)



(b)

**Figure 6.1 Results of Trial 1: (a) recorded pressure–time history, (b) post-experiment photograph of the end of the five-column wall**

The measured post-experimental rotation was approximately  $15^\circ$  at the centre span of the wall and  $13^\circ$  at the end column. The geometric and material properties considered for the wall tested in Trial 1, from Set 1 were

$$\begin{aligned}
 w_a &= 0.975 \text{ m}, & w_b &= 1.2 \text{ m}, & H &= 1.95 \text{ m}, \\
 \rho &= 1850 \text{ kg/m}^3, & K_v &= 14680 \text{ kPa}, & c &= 63.5 \text{ kPa}, \\
 \phi &= 27.77^\circ, & K &= 187.6 \text{ MPa}, & G &= 15.4 \text{ MPa}
 \end{aligned}
 \tag{6.1}$$

These parameters were used along with the recorded reflected pressure–time history in Figure 6.1 (a) to simulate the experiment using the FE and analytical models. The FE-simulated wall reached a peak rotation of  $18^\circ$  before retracting to  $15^\circ$  in its final position due to the cohesion of the soil. The peak and final position are shown by Figure 6.2 (a) and (b), respectively.

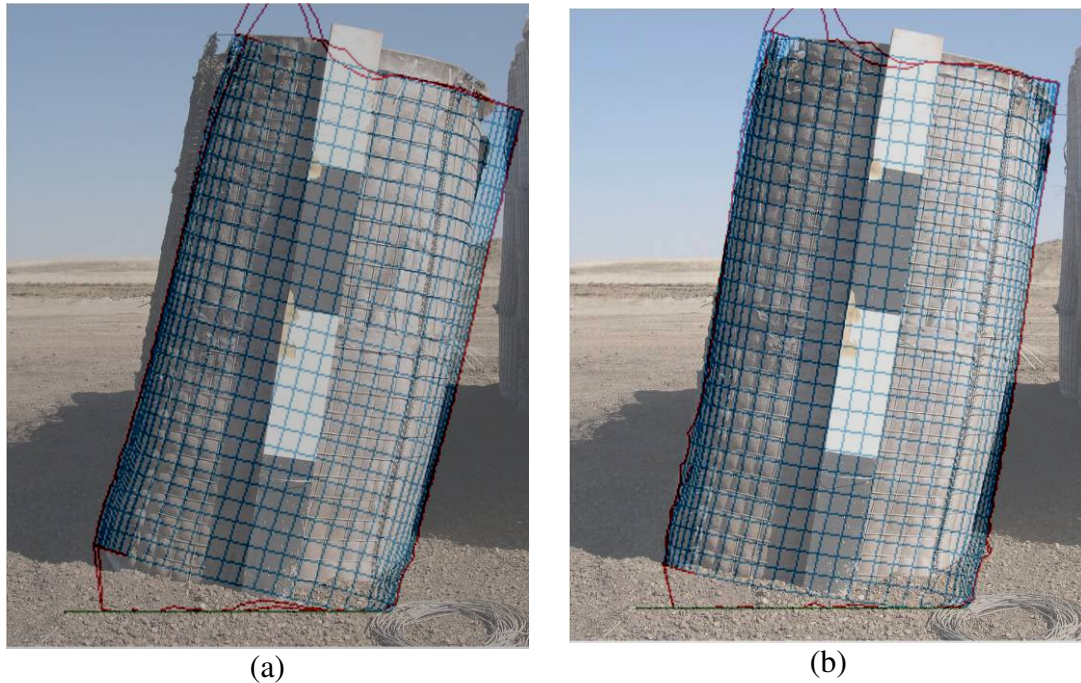


**Figure 6.2 Results of FE model for Trial 1: (a) overlay of maximum FE model response, (b) overlay of final FE model response with the photo of the end column of the wall**

Although the aim of the analysis is to compare the FE model results with the centre column, in the photo overlays the end cell is compared because it is only possible to take a photo of the end column of the wall. The final rotation of the FE model was in excellent agreement with the centre column of the wall in the experiment, (both final rotations

were approximately  $15^\circ$ ). Note that the peak rotation of the wall in the experiment is unknown due to the difficulty in observing the rotation of the wall in the high speed video as earlier stated.

The governing equation of motion for the Rigid-Body Rotation model Eq. (5.9) and governing equations for the Rigid-Body Hybrid model Eqs. (5.35) through (5.37), were coded in Visual Basic using the Runge-Kutta technique in solving a non-linear equation. The time step was selected to be 1 microsecond, which was equal to the time interval used in the experiment to sample and record the reflected pressures. This selected time step was within the size of time step required for convergence of the results (0.1 ms for the Rigid Body Rotation model in as discussed in Section 5.1, and 1 ms for the Rigid-Body Hybrid model as discussed in Subsection 5.2.6). The results of the analytical models are shown in Figures 6.3 (a) and (b), respectively.

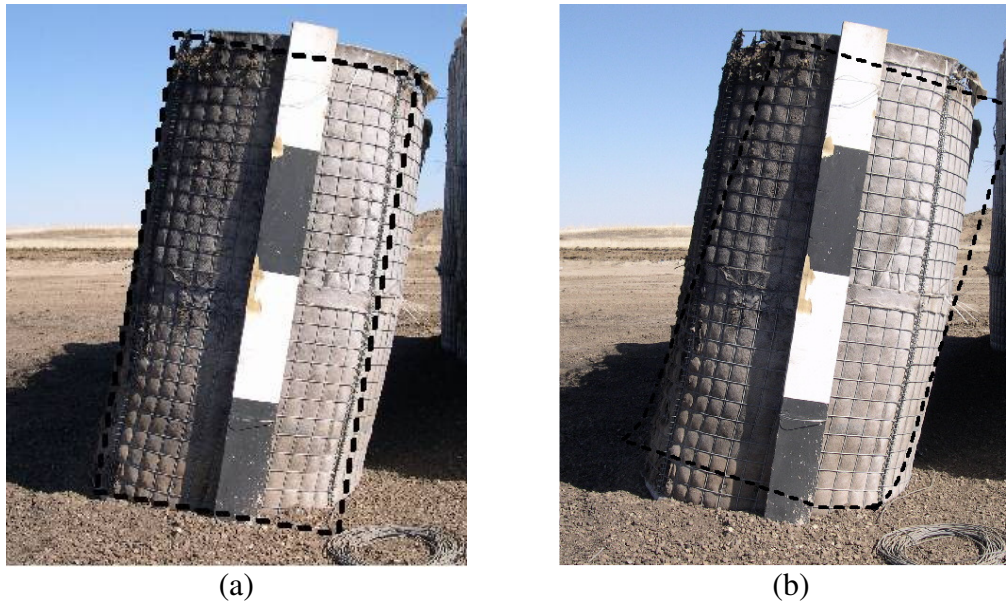


**Figure 6.3 Results of analytical models for Trial 1: (a) overlay of maximum response of Rigid-Body Rotation model, (b) overlay of maximum Rigid-Body Hybrid model response**

The Rigid-Body Rotation model reached a peak rotation of  $13^\circ$ , which was slightly less than the rotation of  $15^\circ$  recorded at the centre span of the wall in the experiment. The Rigid-Body Hybrid model offered too little resistance in comparison to the experimental wall and reached a peak rotation of  $20^\circ$ .

### 6.1.2 Trial 2

An additional two-course Mil 3 wall constructed under the same conditions as Trial 1 with a decrease in the stand-off to increase the loading. The reflected pressure–time history measured for Trial 2 is shown in Figure 6.4. The same geometrical and soil parameters listed for Trial 1 are assumed.

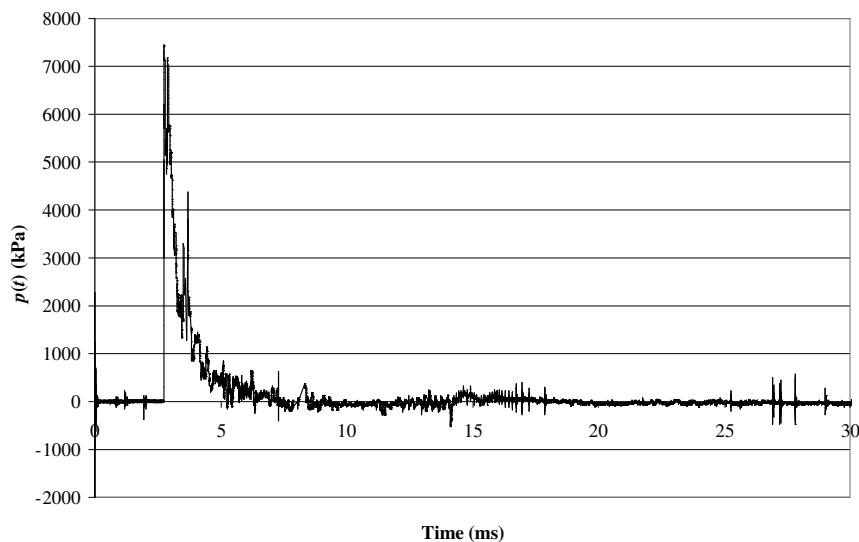


**Figure 6.4** Reflected pressure–time history measured from Trial 2

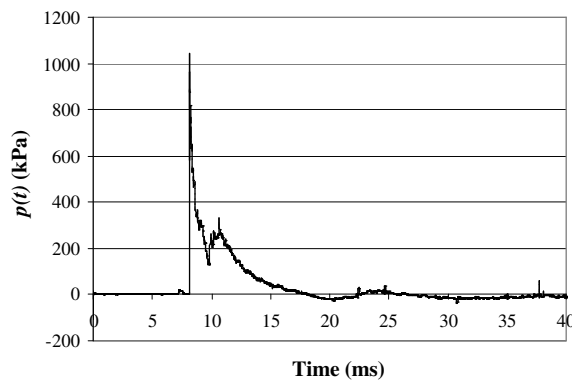
The wall overturned completely in the experiment. Using the loading in Figure 6.4 as input; the FE, Rigid-Body Rotation, and Rigid-Body Hybrid models all calculated the wall to overturn, and thus were in agreement with the experimental result.

### 6.1.3 Trial 3

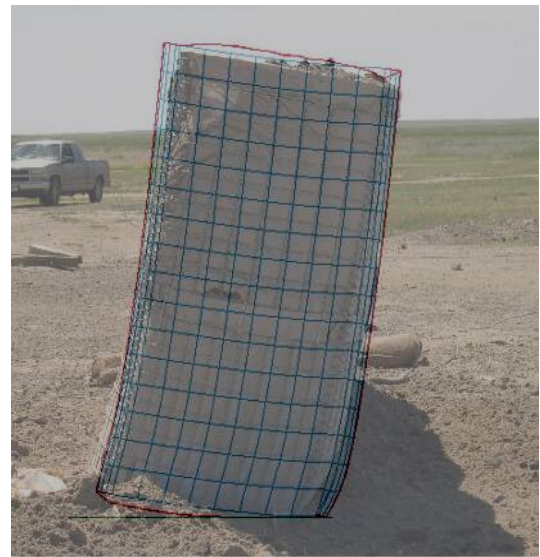
A two-course Mil 2 wall was tested in Trial 3. The following parameters were recorded in this experiment and used for calculating the response of the wall with the FE and analytical models.

$$\begin{aligned} w_a &= 0.6 \text{ m}, & w_b &= 0.74 \text{ m}, & H &= 1.2 \text{ m}, \\ \rho &= 1646 \text{ kg/m}^3, & K_v &= 20740 \text{ kPa}, & c &= 1.797 \text{ kPa}, \\ \phi &= 26.15^\circ, & K &= 163.3 \text{ MPa}, & G &= 8.3 \text{ MPa} \end{aligned} \quad (6.2)$$

Figures 6.5 (a) and (b) show the recorded pressure–time history and post-experiment photograph, respectively. The result from the FE analysis is overlaying the post-experiment photo.



(a)



(b)

**Figure 6.5 Results of Trial 3: (a) recorded pressure–time history, (b) post-experiment photograph with overlay of FE model response**

The measured rotation of the centre column of the HB wall in the experiment was approximately  $12^\circ$ . Since the soil possessed only a very small cohesion, contrary to the re-



sult in Trial 1, there was negligible difference in the peak and final rotation of the FE model. The final rotation predicted by the FE model was approximately  $10^\circ$ . The results of the Rigid-Body Rotation model and Rigid-Body Hybrid model are shown respectively in Figures 6.6 (a) and (b). Both models were in excellent agreement with the experiment. The Rigid-Body Rotation model predicted slightly less rotation than the Rigid-Body Hybrid model ( $11^\circ$  compared with  $12^\circ$ ).

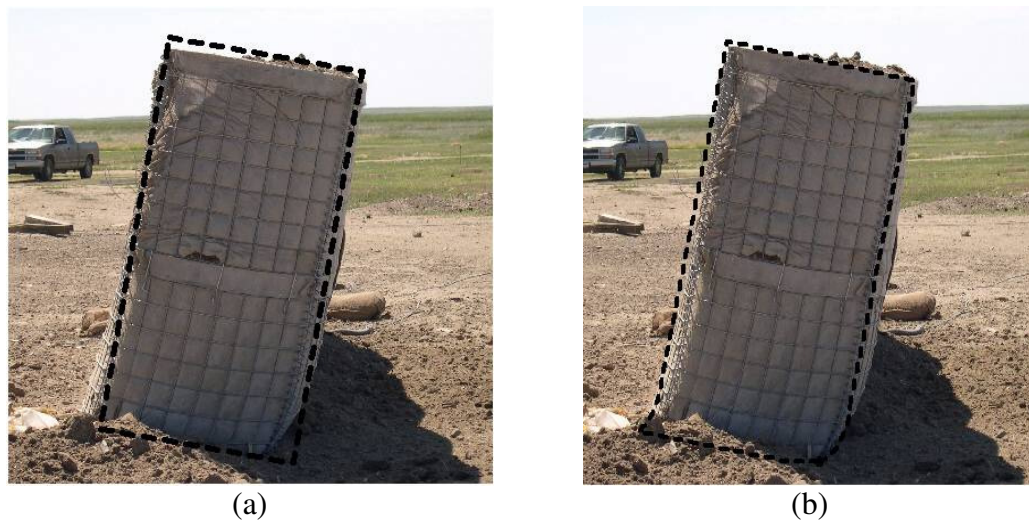


**Figure 6.6 Results of analytical models for Trial 3: (a) overlay of maximum response of Rigid-Body Rotation model, (b) overlay of maximum response of Rigid-Body Hybrid model**

#### 6.1.4 Trial 4

It should be noted that the results from Trials 1 through 3 were limited due to the difficulties in measuring the time histories of rotations or displacements. Therefore subsequent experiments included measurement of displacement–time histories as per the schematic shown in Figure 3.1. Although only 2 displacement gauges at sizable angles from each other are required to calculate horizontal and vertical displacement–time histories, a third gauge at sizable angle from the other two was also used. This was done in case that if one



of the gauges were unsuccessful, horizontal and vertical displacement could still be calculated based on the other two successful gauges. Also, owing to the possibility of soil and debris raised from the blast and striking the pressure gauge, three pressure gauges instead of one were used for Trials 4 through 7.

Figures 6.7 (a) and (b) show the recorded pressure–time history and the post-experimental position of the wall, respectively. It was desired that the wall be loaded to a level that would slightly exceed that required to cause overturning so that entire displacement–time histories up to and including overturning would be measured. One of the three pressure gauges was struck by debris part way through the trace. The two remaining gauges successfully recorded entire pressure–time histories that were nearly identical with one another. These traces were averaged and used as the loading input for both the FE and the analytical models along with the following parameters:

$$\begin{aligned} w_a &= 0.975 \text{ m}, & w_b &= 1.2 \text{ m}, & H &= 1.95 \text{ m}, \\ \rho &= 1570 \text{ kg/m}^3, & K_v &= 20740 \text{ kPa}, & c &= 1.797 \text{ kPa}, \\ \phi &= 26.15^\circ, & K &= 163.3 \text{ MPa}, & G &= 8.3 \text{ MPa} \end{aligned} \quad (6.3)$$

The FE post processing software LS Post [44] was used to obtain the horizontal and vertical displacements from the corresponding monitoring point locations within the FE model. For the Rigid-Body Hybrid model, the horizontal and vertical displacement at a monitoring point,  $u_m$  and  $v_m$ , respectively, can be computed from the height of that monitoring point  $h_m$  (shown in Figure 3.1), and the localized corner displacements  $u$  and  $v$ , the wall rotation  $\theta$  and the thickness of the bulge  $b$  (shown in Figure 5.12) as

$$u_m = (h_m - v) \sin \theta + (u + b) \cos \theta - b, \text{ and} \quad (6.4)$$

$$v_m = (h_m - v) \cos \theta - (u + b) \sin \theta - h_m. \quad (6.5)$$

Note that the thickness of the bulge  $b$  was 112.5 mm, calculated from the Eq. 5.82. Eqs. 6.4 and 6.5 were also used for the Rigid-Body Rotation model to calculate horizontal and vertical displacements of a given monitoring point by setting  $u$  and  $v$  to zero.

Figure 6.7 (c) shows the horizontal and vertical experimental displacement–time histories of the upper monitoring point  $u_{mu}$  and  $v_{mu}$ , respectively, along with those predicted by the FE analysis and the analytical models. All three cable displacement gauges performed for the duration of the wall movement in the experiment. In this case, all three solutions for horizontal and vertical displacements were obtained (i.e. that from the first and second, first and third, and second and third cable displacement gauges). Only small differences between the three solutions ( $\pm 5$  mm) occurred and the average of the three solutions was taken as the experimental displacements. Due to the wall overturning and hitting the gauge stand at 830 ms, the experimental displacement–time histories have been truncated at 830 ms as displacements measured beyond this time were no longer accurate. Since the ground that the wall toppled onto was not included in the formulation of any of the analytical models, the resulting displacement–time histories calculation for the analytical models were truncated when the vertical displacements were equal to the heights of the monitoring points. The results from the FE analysis are in excellent agreement with the experimental results (the horizontal displacement-time histories are within 5 % of each other). The Rigid-Body Rotation model possessed too much resistance and was not in good agreement with the experimental results. The Rigid-Body Hybrid model was in

very good agreement (within 10 % of the experimental displacements), but provided slightly more resistance compared with the wall in the experiment and the FE model.

A comparison of the cable displacement results at the lower monitoring point are presented in Figure 6.7 (d). At the lower monitoring point, only the change in the length of the cables can be used for comparing the models of experiments because both displacement gauges attached to the lower monitoring point were at the same angle in the experiment (Figure 3.1).

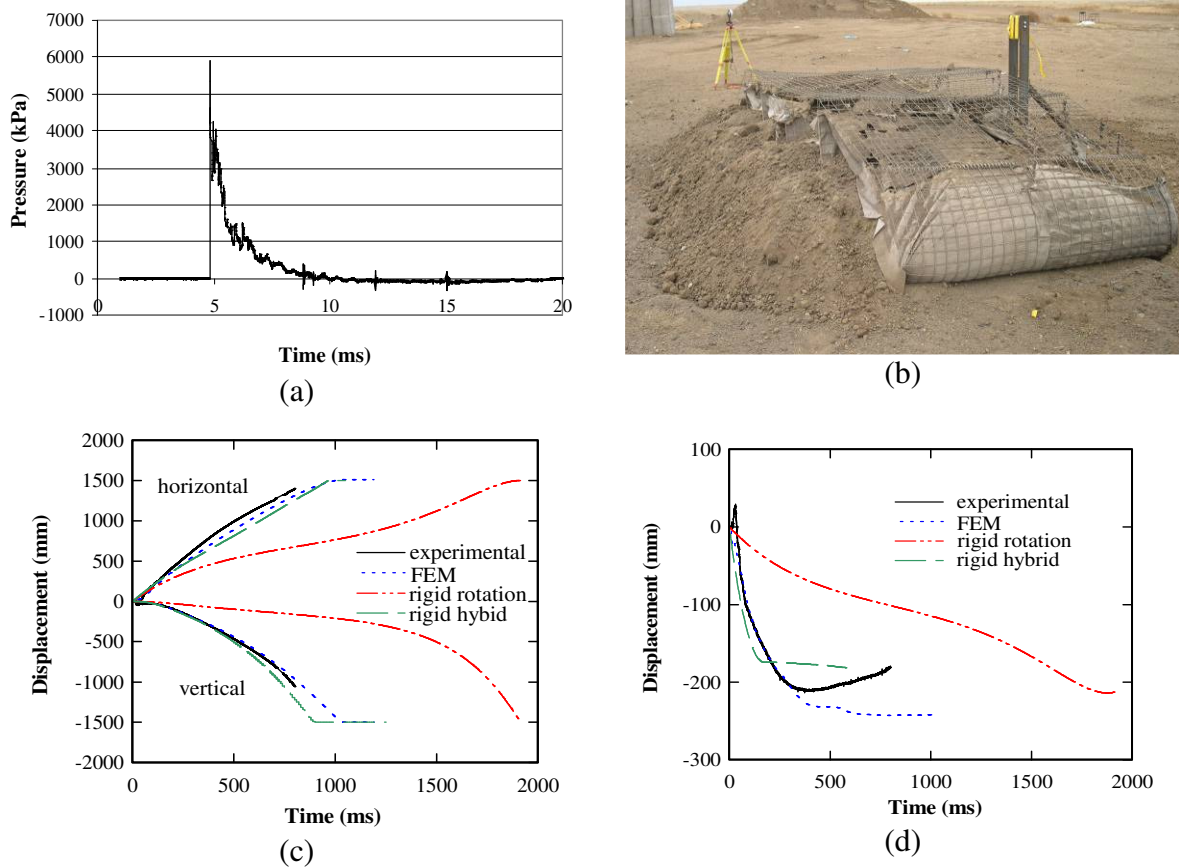


**Figure 6.7 Results of Trial 4: (a) recorded pressure–time history, (b) post-experiment photograph, (c) comparison of horizontal and vertical displacement–time histories of upper monitoring point, and (d) comparison of experimental and calculated cable displacement–time histories of lower monitoring point**

The displacement-time histories recorded by both gauges at the lower monitoring point were measured within 1 % of each other. The result presented here is the average of the two measurements taken. However it is not entirely certain in this particular experiment why the displacement at the lower monitoring point retracted at approximately 350 ms. The most likely cause was that a cover on one of the displacement gauge enclosures located directly underneath both lower displacement cables was loosened and uplifted from the blast, and may have impacted both of these lower displacement cables.

To compare the displacement–time histories at the lower monitoring point obtained from the FE and analytical models with the recorded values, it is necessary to calculate what would be recorded by imaginary displacement gauges attached to the FE and analytical models in the same configuration as the experiment. After obtaining the horizontal and vertical displacements at the lower monitoring point (by using the LS Post for the FE model, or using Eqs. (6.4) and (6.5) for the analytical models), the change in length of the cable is calculated by:

$$\Delta s = \sqrt{(A - u_{ml})^2 + v_{ml}^2} - A, \quad (6.6)$$

where distance  $A$  is shown in Figure 3.1, while  $u_{ml}$  and  $v_{ml}$  denote the horizontal and vertical displacements given in Table 3.1 at the lower displacement monitoring point, respectively.

In Figure 6.7 (d) both the FE model and Rigid-Body Hybrid model both show shear displacements of approximately 175 and 220 mm in the early time history which cease at 200 ms for the Rigid-Body Hybrid model and 400 ms for the FE model. The slight dis-

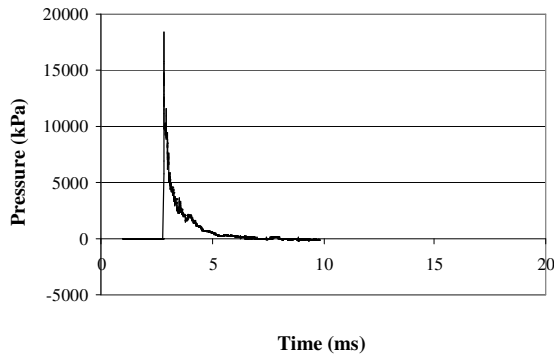
placement following the shear behaviour is mostly due to movement of the lower monitoring point caused by rotation. The lower monitoring point displacement for the Rigid-Body Hybrid model was truncated after 550 ms, which is much less than the experimental and FE extent of the displacement-time history. This is because after undergoing approximately 175 mm of shear in the initial displacement-time history, the monitoring point passes below ground elevation at much less rotation, where the displacement-time history is no longer valid. This was done for this comparison as well as following comparisons.

In general, all lower monitoring point displacements are in reasonable agreement (within 20 %) except the results from the Rigid-Body rotation model. The Rigid-Body rotation model does not include shear or sliding behaviour at the bottom of the wall, and thus its result is comparatively in poor agreement with the experiment and the FE model.

### 6.1.5 Trial 5

A one-course Mil 1 HB wall was tested in Trial 5. Only one of the three pressure gauges successfully recorded an entire pressure-time history, which was assumed as the loading for the models. The following parameters were used for the FE and analytical models:

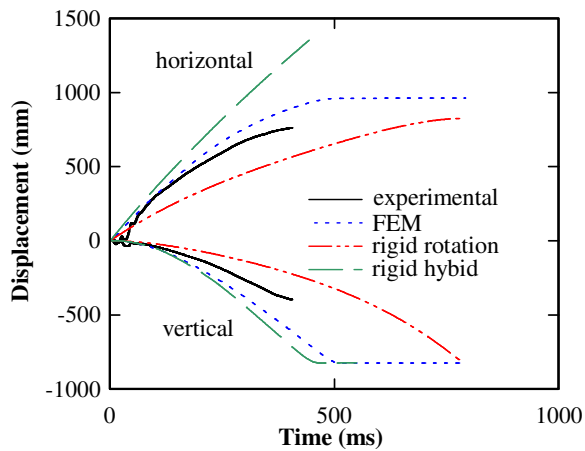
$$\begin{aligned} w_a &= 1.05 \text{ m}, & w_b &= 1.33 \text{ m}, & H &= 1.35 \text{ m}, \\ \rho &= 1570 \text{ kg/m}^3, & K_v &= 20740 \text{ kPa}, & c &= 1.797 \text{ kPa}, \\ \phi &= 26.15^\circ, & K &= 163.3 \text{ MPa}, & G &= 8.3 \text{ MPa} \end{aligned} \quad (6.7)$$



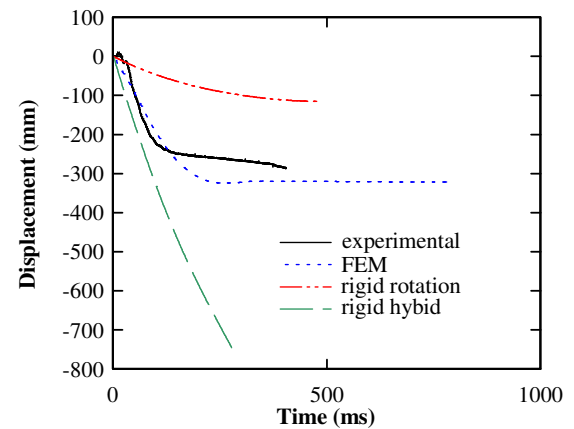
(a)



(b)



(c)



(d)

**Figure 6.8 Results of Trial 5: (a) recorded pressure–time history, (b) post-experiment photograph, (c) comparison of horizontal and vertical displacement–time histories of upper monitoring point, and (d) comparison of experimental and calculated cable displacement–time histories of lower monitoring point**

Figures 6.8 (a) and (b) show the history recorded and the post-experimental position of the wall, respectively. From Figure 6.8 (c) it is estimated that after 400 *ms* the experimental measurement became inaccurate due to interference of the top corner of the wall with the cables, and thus the experimental results are truncated at 400 *ms*. Again the Rigid-Body Rotation model substantially under-predicted the displacement at the lower monitoring point and reacted too slowly for the displacement at the upper monitoring point,

which implied that this model possessed too much resistance. The FE analysis slightly over-predicted the displacement time history near the end of the trace, while the Rigid-Body Hybrid model over-predicted the displacements. Similar observations are obtained for the displacement at the lower monitoring point, shown in Figure 6.8 (d). Note that if negative rotation does not take place, large lower monitoring point displacements will translate to large upper monitoring point displacements. The Rigid-Body Hybrid model over-predicted displacement at the lower monitoring point, and this over-prediction was responsible for the over-prediction of the horizontal displacement at the upper monitoring point. Comparison of Figures 6.8 (c) and (d) illustrates the magnitude of the over-prediction in the horizontal displacement at the upper monitoring point is approximately the same as the magnitude of the over-prediction of the displacement at the lower monitoring point.

#### 6.1.6 Trial 6

The test in Trial 4 was repeated with an increase in the standoff to reduce the loading on the wall. Only one of three pressure gauges successfully recorded the entire pressure–time history. The geometrical and soil parameters for the FE and analytical models are identical to Trial 4 except the pressure–time history.

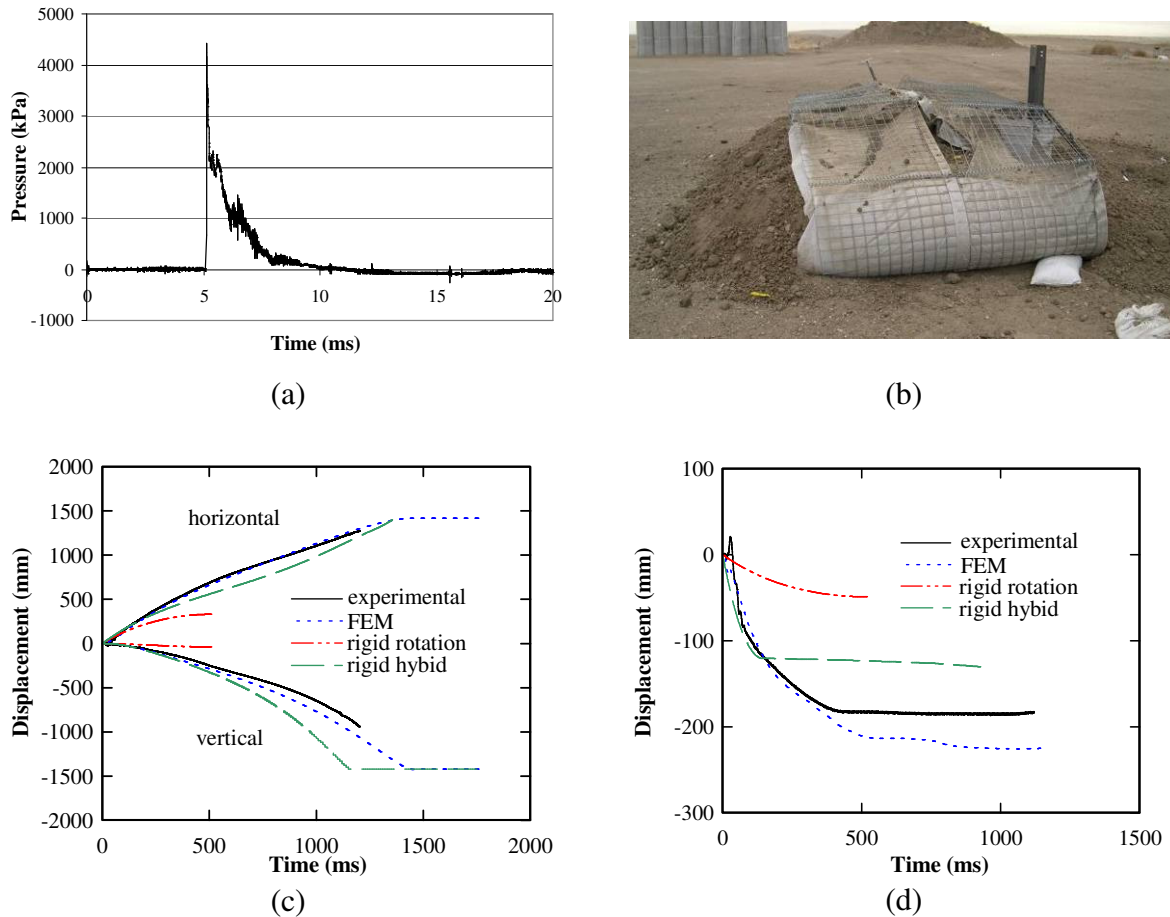


**Figure 6.9 Results of Trial 6: (a) recorded pressure–time history, (b) post-experiment photograph, (c) comparison of horizontal and vertical displacement–time histories of upper monitoring point, and (d) comparison of experimental and calculated cable displacement–time histories of lower monitoring point**

In the experiment, the wall overturned and impacted the gauge stand. As a result, the late time history of the measured displacements at the upper monitoring point in Figure 6.9 (c) was not accurate after 1200 ms. The FE model was in excellent agreement prior to 1200 ms (within 5 % of the experimental displacements). The Rigid-Body Hybrid model was in good agreement (within 15 % of the experimental displacements), but possessed slightly more resistance than both the FE model and the experimental result. The Rigid-



Body Rotation model did not overturn but predicted a maximum rotation of  $14^\circ$  and therefore was in poor agreement with the other models and the experiment result.

Comparison of the displacement–time history at the lower monitoring point is shown in Figure 6.9 (d). The result from the FE analysis is within 20 % of the experimental result. The Rigid-Body Hybrid model moderately under-predicted the displacement showing that the resistance to shear deformation at the bottom of the wall was higher than the experiment and the FE model.

#### 6.1.7 Trial 7

Trial 5 was also repeated with an increased charge standoff to reduce the loading on the wall. Two of the three pressure gauges successfully recorded pressure–time histories, and the average of these two time histories were assumed as the loading. The geometrical and soil parameters are identical to Trial 5. The wall overturned onto the gauge stand and therefore the vertical displacement–time history of the upper monitoring point after 450 ms is not considered accurate in Figure 6.10 (c). The measurement horizontal displacement may have also been affected to a lesser extent and the full time-history is included in the plot. Generally, all modelling results are within 5 % for time histories up to 450 ms, except the Rigid-Body Rotation model, which did not overturn but reached a maximum rotation of  $17.3^\circ$ . Comparing the results of the displacement at the lower monitoring point in Figure 6.10 (d), the FE model is within 10 % of the experimental results, while the Rigid-Body Hybrid model moderately over-predicted the displacement at the lower monitoring point.

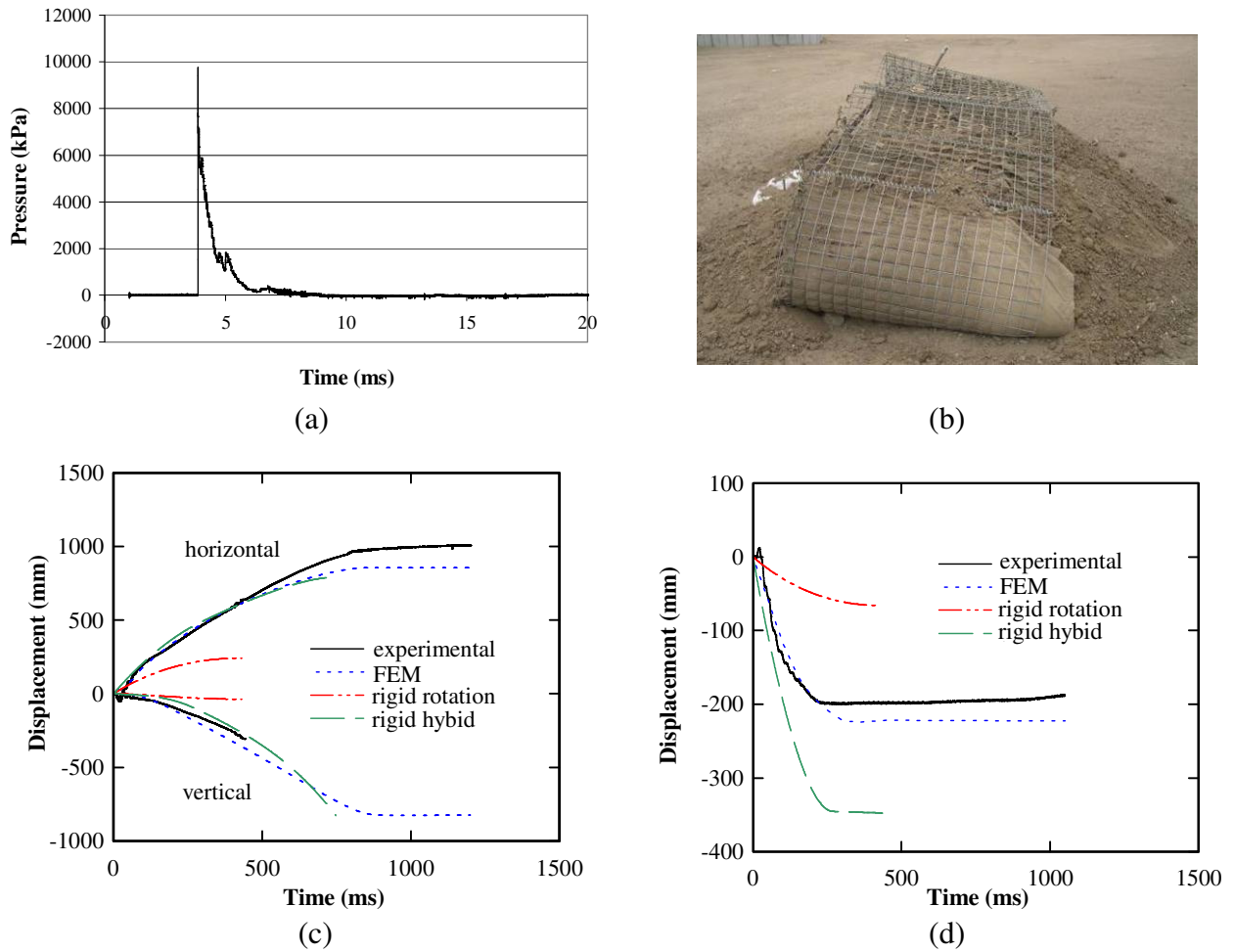


**Figure 6.10 Results of Trial 7: (a) recorded pressure–time history, (b) post-experiment photograph, (c) comparison of horizontal and vertical displacement–time histories of upper monitoring point, and (d) comparison of experimental and calculated cable displacement–time histories of lower monitoring point**

## 6.2 Discussion of FE model

Overall very good agreement was reached in the comparison of the FE model response with the experimental response of the walls for all trials (FE displacements averaged

within 10 % of the experimental displacements). Displacement–time histories of a monitoring point on the back of the wall were successfully extracted from the experiments, although in the late time histories, the cables of the displacement gauges were contacted by the top corner of the wall. In addition, the wall toppled onto one of the gauge mounting frames, causing further errors in the experimentally measured displacement–time history and further disagreements with the FE model. This was unavoidable because the precision in the displacement measurement would be lost if the angle between each gauge would have been reduced appreciably by setting the retractable gauges further back in the experiments.

In the process of accessing the validity and the accuracy of the FE model, several potential sources of error and additional behaviours that could possibly influence the response of the FE model were investigated and are discussed below.

***The difference in surface of the pressure gauge and of the HB wall:*** Theoretically, the reflected pressure will be higher when a blast wave strikes a rigid object than when a blast wave hits a deformable or movable object. This would cause the rather rigid steel mounted pressure gauges to record more load than was actually applied. However, Scherbatiuk et al. [23] found that given the extremely high shock impedance of both steel and soil compared with air, the difference in reflected pressures and impulse is negligible. Thus within engineering assumptions, both the steel and the soil can be approximated as rigid reflected surfaces. Estimations of this error through conducting fully coupled 1-D uniaxial calculations of the effect of the impact of a shock wave in air on a column of soil

showed that the aforementioned assumption would result in the loading being overestimated by less than 1.5 percent according to Scherbatiuk [23].

***The effect of a ground shock:*** The ground shock acceleration–time history from the charge was calculated using ConWep (Hyde [17]) and the calculated accelerations were applied to the rigid ground in the FE analysis. ConWep assumes the charge to be on the ground surface while in the actual experiment, each charge had a 1 m height of burst. For that reason, using the ConWep-calculated ground shock should overstate the amount of ground shock and lead to a conservative result. Since ConWep does not provide a vertical ground acceleration–time history, the vertical ground acceleration–time history was assumed to be equal to the horizontal ground acceleration, recommended by TM5-1300 (US Department of the Army [11]). It was found that adding the ground shock acceleration–time history to the FE analysis made negligible difference in the result of the FE calculation. This was because the particle displacement caused by the ground shock is very small in comparison with the overall displacement of the wall. ConWep predicted less than one centimetre of horizontal particle displacement at the ground surface below the base of the wall due to the ground shock.

***The pressure on the rear of the wall:*** Loadings only on the front face of the walls were recorded in the experiments and these loadings were applied to the front face of the FE model of the wall. The loading impinging on the rear of the wall was neglected in the analysis. A Computational Fluid Dynamics (CFD) model was constructed using AutoDyn® software [34] to model the charge and the blast wave loading the wall. The peak pressure recorded on the rear of the wall was less than 3 % of the peak pressure recorded

on the front of the wall. The net impulse of the positive and negative phases on the rear face of the wall was less than 3 % of the net impulse on the front face of the wall. Since the wall response is largely governed by the impulse of the loading (Scherbatiuk et al. [24]), it was concluded that in this case, using the pressure recorded on the front face of the wall was a sufficient approximation for the net loading on the wall. For further details please see Appendix K.

***Increase in soil strength and stiffness under dynamic loading:*** The mechanical properties of the soil in terms of compressibility and yield relationships were derived using triaxial tests. These triaxial tests were performed at a slow rate, with measurements taken at initial time increments of 30 seconds. The time to fail the specimens in the tests typically took over 30 minutes. The entire dynamic response of the walls normally occurs in the 0.5 to 1.5 second range, which is much shorter than the triaxial test conditions. Prakash [47] reported that soil strength and stiffness under forced transient loading were substantially greater than those under quasi-static loading condition. Since the increase in soil strength and stiffness contribute to the increase in the resistance of the walls, then it can be assumed that including the rate dependant increase in strength of the soil in the FE analysis would likely increase the resistance of the walls.

***Differences in soil strength and stiffness arising from differences in compaction:*** The strength and stiffness of the soil will increase with increased compaction. It is possible that the soil near the bottom of the filled HB units was more compacted than the soil near the top of the wall due to the compaction of soil layers above. This increase in the density may lead to an increase of the internal shear resistance at the bottom of the wall. How-

ever, the assumption that the soil properties were uniform throughout the height of the wall was made in this study based on that little differences were shown in the compacted densities of the tops of the upper and lower courses in the two-course walls. This was because of the results of measuring the densities. The change in the soil properties along the height is beyond the scope of this study.

***Differences between the compacted density of the soil-fill and the initial densities of the triaxial test specimens:*** For the experiments involving measurement of the displacement–time histories (Trials 4 through 7), triaxial test specimens were prepared to a density of approximately  $1700 \text{ kg/m}^3$  due to the additional compaction needed to form test specimens that would not break apart and be well-formed. The average compacted density of the soil in these four experiments was approximately  $1570 \text{ kg/m}^3$ . Thus it is likely that the mechanical properties consisting of  $K$ ,  $G$ , EOS, and yield relationship determined by the triaxial tests may be slightly too stiff compared with the soil mechanical properties in the experiment, which may have lead to more resistance in the FE model than would be otherwise. The magnitude of influence that this discrepancy has on the response of the FE model cannot be evaluated since the soil properties at a density of  $1570 \text{ kg/m}^3$  are not known.

The validation of the FE model with the experimental results provides a good understanding on the behaviour of the HB walls under blast loading. It is noted that the largest model, i.e. the walls in Trial 5 and 7, using a two half-column model with 37.5mm elements in the FE analysis, took approximately 8 hours to run on a Pentium IV® 2.2 GHz laptop computer with 1 GB of RAM.

## 6.3 Discussion of Rigid-Body Rotation model

### 6.3.1 Examination of analytical behaviour

Since the Rigid-Body Rotation is a reasonable approximation for the actual behaviour of HB walls subjected to blast loading, examination of this simple model enables one to understand some of the important and unique aspects of the response of HB walls. Eq. (5.16) implies that the impulse that the wall can sustain is proportional to the square root of the soil density. Thus compaction of the soil to higher densities will help improve the resistance of the walls slightly due to the higher densities achieved. Additional benefits may also result from increased compressive and shear resistance due to added compaction, the effect of which is not included in the Rigid-Body Rotation model. The effect of soil properties on HB wall response will be considered later in this chapter.

If a HB wall is loaded to a level where moderate rotation is attained, large changes in rotation can take place for relatively small changes in loading. This can be shown through deriving the amount of impulse required to rotate the wall to a fraction  $\lambda_\alpha$  of its critical rotation angle  $\alpha$ . Similar to the derivation of the impulse asymptote in Section 5.1, the expression for Potential Energy required to rotate the wall a fractional angle is

$$PE = mgR \int_0^{\lambda_\alpha \alpha} \sin(\alpha - \theta) d\theta = mg \left( R \cos((1 - \lambda_\alpha)\alpha) - \frac{H}{2} \right). \quad (6.8)$$

Upon equating this with the kinetic energy expression in Eq. (5.13), the amount of impulse required to rotate the wall to a fraction of the critical rotation angle can be solved as

$$I_{\lambda\alpha} = \frac{2}{H^2} \sqrt{2\rho I_o mg \left( R \cos((1-\lambda_\alpha)\alpha) - \frac{H}{2} \right)}. \quad (6.9)$$

Dividing this equation with the equation critical overturning impulse Eq. (5.16), an equation for the fraction of critical overturning impulse  $\lambda_I$  as a function of the fraction of the critical angle  $\lambda_\alpha$  is obtained as

$$\lambda_I = \frac{I_{\lambda\alpha}}{I_{crit}} = \sqrt{\frac{R \cos((1-\lambda_\alpha)\alpha) - \frac{H}{2}}{R - \frac{H}{2}}}. \quad (6.10)$$

This relationship is plotted in Figure 6.11 for a two-course Mil 3 wall and a one-course Mil 1 wall, and is only dependent on the width and height of the wall. Both lines are virtually identical. From plotting this relationship for different height-to-width ratio walls it was observed that the relationship is extremely insensitive to changes in geometry.

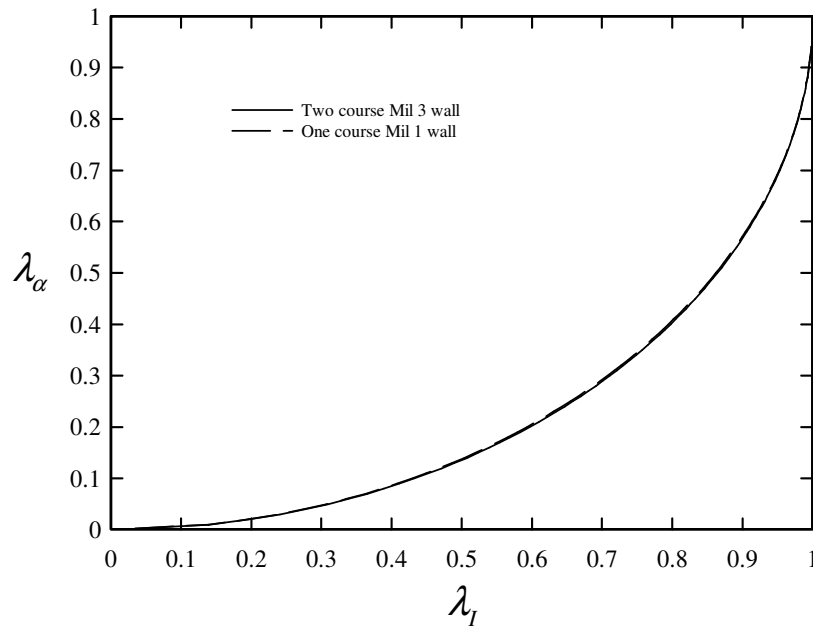


**Figure 6.11** Fraction of critical angle  $\lambda_\alpha$  as a function of fraction of critical impulse  $\lambda_I$  for Rigid-Body Rotation model



The relationship shows that the amount of rotation attained in proportion to the critical angle becomes very sensitive to small changes in impulse when the wall is loaded to significant rotations. From the graph, a wall loaded at 50 % of its critical impulse will only rotate to approximately 14 % of its critical angle. A wall loaded to 80 % of its critical overturning impulse will only rotate to 40 % of its critical angle. An additional 25 % more applied impulse on top of this amount is enough to attain the critical impulse and overturn the wall completely. The difference of results between moderate rotation and overturning occurs over a relatively small range of impulse. This behaviour makes it very difficult to plan experiments with the desired outcome of causing large rotations in free-standing HB walls without causing them to overturn. The moderate to large rotations attained without overturning in Trials 1 and 3 were fortunate results.

### 6.3.2 Comparison with experiment results

For the HB walls tested against blast that did not overturn but sustained moderate rotation angles (Trials 1 and 3), excellent agreement (rotation angles within 5 % of the experiment) was reached. The observed primary response mode, i.e. the final rotation about the base of the wall, agreed well with calculated values from the Rigid-Body Rotation model. In the experiment, the upper  $\frac{3}{4}$  of the walls maintained rigid-body behaviour showing little or no shear. But the comparison of the displacement–time histories in Trials 4 through 7 revealed that the model possessed more resistance towards overturning compared with the experimental displacement–time histories. In Trials 6 and 7, contrary to the results of the experiments, the Rigid-Body Rotation model did not predict overturning.

The Rigid-Body Rotation model performed well in some comparisons and not others. To help explain the source of this discrepancy, the results of Trial 3 are reconsidered.

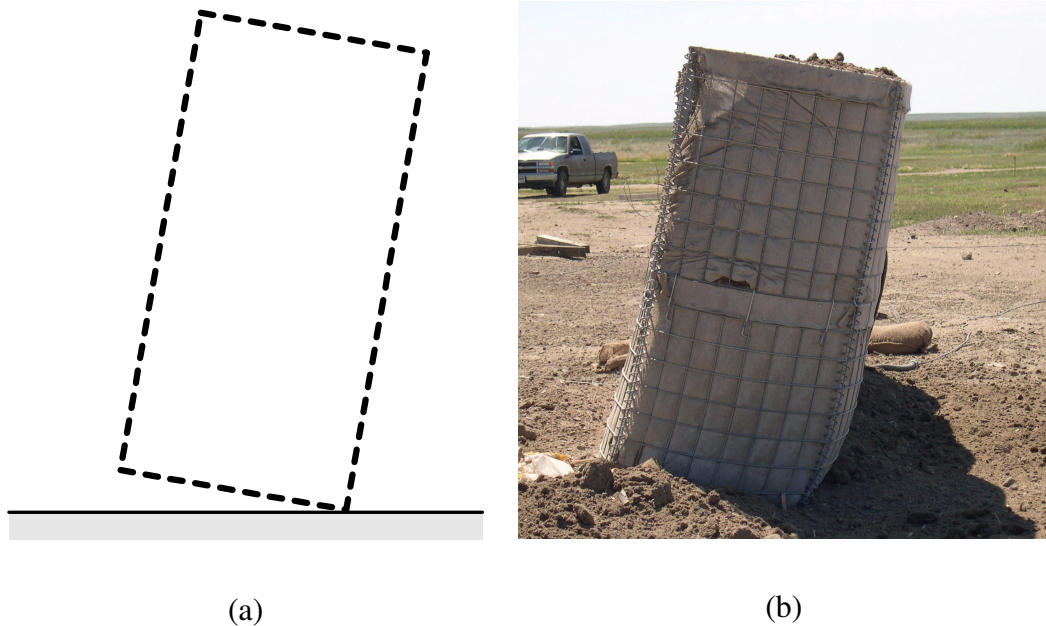


**Figure 6.12 Comparison of Rigid-Body Rotation model with post-experiment photo in Trial 3: (a) maximum response of Rigid-Body Rotation model, (b) post-experiment photo**

To overturn the rigid shape in Figure 6.12 (a) in its rotated state would still take a significant amount of impulse. The experimental wall in Figure 6.12 (b) has undergone significant shear at the bottom, and the centre of gravity has laterally shifted and is closer to being directly overtop of the resultant of the vertical stress distribution at the base of the wall. Therefore, the wall in the experiment would not need much more impulse for it to overturn. Had the loading been increased, the wall in the experiment may have overturned while the Rigid-Body Rotation model would have only achieved higher rotation without overturning. Despite this discrepancy, the predictions by the Rigid-Body Rotation model are reasonable for slight to moderate rotations. Deficiencies of the Rigid-Body

Rotation model for differing angles of rotation will be examined more formally later on in this chapter and the limitations of the model will be established.

The behaviour of the Rigid-Body Rotation model helps provide understanding of the behaviour of HB walls under blast loading and their primary response mode of rigid-body rotation. It is noted that on average each experimental simulation using the Rigid-Body Rotation model took approximately 20 seconds to run on an Intel Pentium™ IV 2.2 GHz laptop computer with 1 GB of RAM using a 0.001 ms time step (the time interval used for recording the pressure–time histories). If the pressure–time histories are approximated using a 0.1 ms time interval and if a 0.1 ms time step is used, each calculation takes less than one second.

## 6.4 Discussion of Rigid-Body Hybrid model

### 6.4.1 Comparison with post-experiment deformation

The Rigid-Body Hybrid model was in excellent agreement with the experiments for Trial 2 (predicted overturning) and 3 (predicted rotation within 5 % of the experiment), but over-predicted the rotation in Trial 1. In Trial 1 the Rigid-Body Hybrid model rotated to 20°, while the wall in the experiment rotated 15°. Note that reducing the impulse of the loading by 6 % (through scaling down the time scale in the pressure trace) would cause the result of the model to match the experiment. This shows that despite a 33 % over-prediction in rotation angle, the model only deviated by 6 % for the impulse. In view of the discussion in Subsection 6.3.1, it was expected that the Rigid-Body Hybrid Model

would also show large changes in rotations for small changes in impulse. Therefore the model is not as inaccurate as originally appeared, but discrepancies are increased by the sensitivity of rotation to small changes in impulse when loadings corresponding to sizable rotations occur.

#### 6.4.2 Effect of cohesive soil-fill

Despite that the accuracy may be better from the perspective of applied impulse rather than rotation, there is a reason why the Rigid-Body Hybrid model for Trial 1 particularly, over-predicted the rotation. Consider the illustration in Figure 6.13.

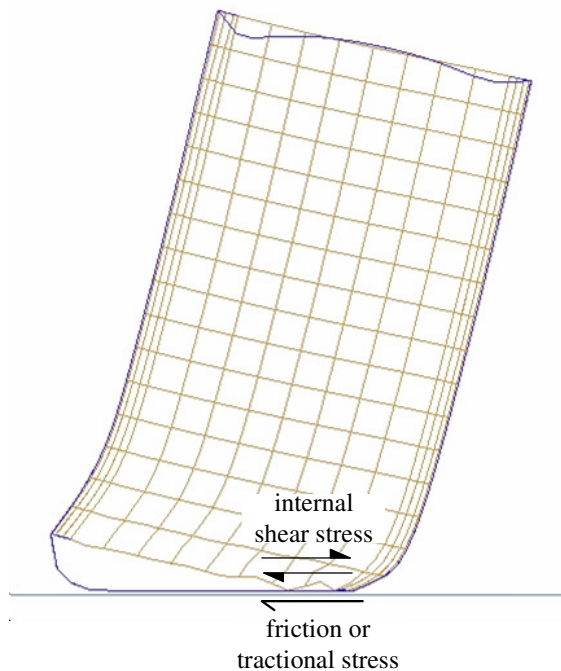


**Figure 6.13 Interaction of friction and internal shear stress**

The resistance to sliding and the resistance to internal shear act in series with one another due to the transfer of friction stress to internal soil stress. If two elastic springs of differ-

ent properties are in series, more deformation in the spring of least stiffness will occur. However both sliding and the resistance to internal shear act as elastic perfectly plastic systems, and since the plastic deformation in this problem is many times larger than the elastic deformation, both of these relationships could be approximated as rigid plastic. If two springs of rigid plastic material properties are in series with one another, only the spring with the lower plastic resistance will deform and the other one will not. Thus depending on which mechanism has less plastic resistance, either internal shear or sliding will dominate, and this depends on the normal force. Referring to Figure 6.13, the applied normal force or stress at the base of the wall at the ground will be slightly more than the applied normal force or stress at a point within the wall just above the base, and it is reasonable to assume that they are approximately equal with one another. Note that the soil properties for Trials 3 possess little cohesion (1.797 kPa), while in Trial 1, the soil possesses substantial cohesion (63.5 kPa). If the soil possesses cohesion, the cohesion at the base of the wall will not be continuous at the interface of hard ground and backfill. The effective coefficient of friction will be greater or equal to  $\tan \phi$  of the fill due to the effect of the wire mesh digging into the soil. As a result, the magnitude of resistance against sliding and the internal shear deformation, if plotted with the applied normal stress or force, will cross over each other as shown in Figure 6.14 (a). For lower applied normal stresses, the resistance to sliding is less than the resistance to internal shear, and sliding will dominate. For higher applied normal stresses beyond the crossover, the resistance to soil internal shear will be less than the resistance to sliding, and internal shear will dominate. This last statement is also true for cohesionless soils, shown in Figure 6.14 (b).

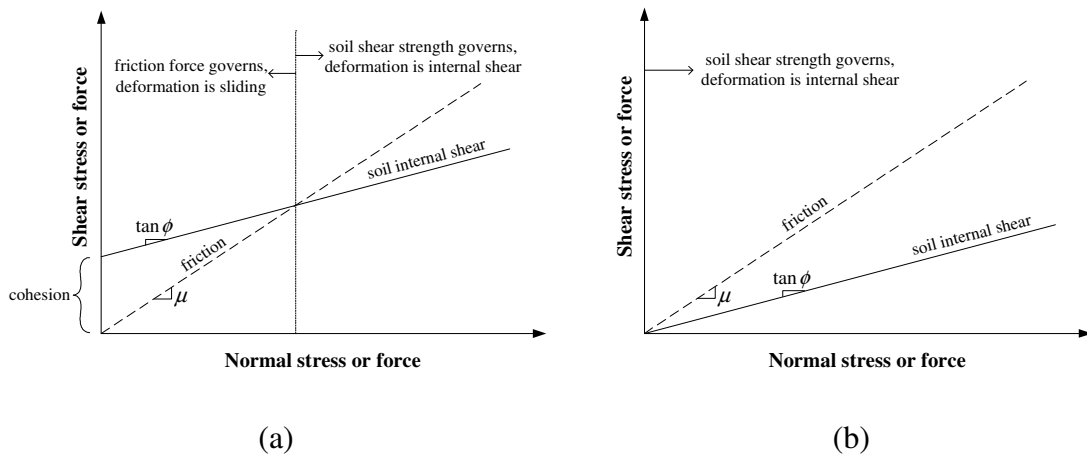


**Figure 6.14** Illustration of determination of shear or sliding behaviour for different soil types: (a) cohesive soil, (b) cohesionless soil

Due to the cohesion of the soil-fill for Trial 1, significant sliding took place which was not accounted for by the Rigid-Body Hybrid model (approximately 7 cm in the FE model, which was nearly equal to 6 cm recorded for the experiment). One of the assumptions in the derivation of the Rigid-Body Hybrid model was that while cohesion was considered in calculating the shear resistance of the soil, only internal shear took place because point  $O_I$  in Figure 5.4 is fixed to the ground. To test the effect that sliding had on the FE model, the corner of the wall in the FE model was constrained not to slide and the model was recalculated. The FE model over-predicted the rotation in comparison with the experiment by approximately the same amount as the Rigid-Body Hybrid model. Thus over-prediction of the rotation by the Rigid-Body Hybrid model was caused by not considering sliding within the model, and it is likely that reasonable results would be achieved if sliding was considered. Therefore the existing Rigid-Body Hybrid model in this thesis is only applicable to soils of little or no cohesion. It is recommended for future models to consider sliding of point  $O_I$  so that the effect of cohesive fills could be cap-

tured accurately. However since the difference in terms of the applied impulse was only 6 % between the Rigid-Body Hybrid model and FE model in Trial 1, it can be inferred that the accuracy of the model is only moderately affected.

### 6.4.3 Comparison of displacement–time histories

Table 6.1 summarizes the overall comparisons of results between the Rigid-Body Hybrid model and the experimental results for the experiments involving measurement of displacement–time histories (Trials 4 through 7).

**Table 6.1 Summary of the comparison of the results from the Rigid-Body Hybrid model with the results from the experiments for displacement–time histories in Trials 4 through 7**

HB Wall Type	Agreement of Upper Point Upper point Results	Agreement of Lower Point Lower point Results
<b>Trial 4 - Two-course Mil 3</b>	Within 5 % for early time history, under predicted by 10 % for late time history	Within 5 % for early time history, under predicted by 15 % for late time history
<b>Trial 5 - One-course Mil 1</b>	Within 5 % for early time history, horizontal and vertical displacements are over predicted by 50 % for late time history	Within 10 % for early time history, over predicted by 70 % for late time history
<b>Trial 6 - Two-course Mil 3</b>	Within 5 % for early time history, horizontal displacements under predicted by 10 %, while vertical displacements over predicted by 20 % for late time history	Excellent for early time history, under predicted by 35 % for late time history
<b>Trial 7 - One-course Mil 1</b>	Excellent for early time history, under predicted by 5 % for late time history	Excellent for early time history, over predicted by 65 % for late time history

For all experiments the Rigid-Body Hybrid model was within 5 % of experimental results in the early displacement–time histories, but not as close of agreement for the late time histories. It is important to note that the walls in Trials 4 and 5 were loaded with significantly more loading than the walls in Trials 6 and 7. This is evident from comparison of the pressure trace from Trial 4 with Trial 6, (Figure 6.7 (a) with Figure 6.9 (a), respectively), and comparing the pressure trace from Trial 5 with Trial 7, (Figure 6.8 (a) with Figure 6.10 (a), respectively). In Trials 4, 6, and 7 the Rigid-Body Hybrid model was in reasonable agreement with the experiments (within 20 %) for the late time histories. However the model was in poor agreement with the experiment for the late time history in Trial 5. In terms of impulse, Trial 4 was loaded with approximately 21 % more specific impulse compared with Trial 6, and Trial 5 was loaded with approximately 50 % more specific impulse compared with Trial 7. Since all walls overturned, it can be concluded that the wall in Trial 4 was loaded over its critical overturning loading by at least 21 %, while the wall in Trial 5 was loaded over its critical overturning loading by at least 50 %. Since the walls in Trials 4 and 5 were overloaded somewhat beyond the critical loading, this may have altered the behaviour of the model to some extent. A number of observations can be deduced from Table 6.1. However, one should keep in mind that only a limited number of experiments were conducted and thus there is inherent uncertainty associated with any observations. These observations can only provide some evidence that may be worth investigating more thoroughly. Notwithstanding, the interpretation of the results in Table 6.1 by the author is as follows:



1. Generally the Rigid-Body Hybrid model under-predicts displacement of the lower monitoring point and shearing near the bottom for walls of higher height-to-width ratios and over-predicts shearing at the bottom for walls of lower height-to-width ratios.
2. When the walls are overloaded well beyond their critical overturning capacity, the model over-predicts both the horizontal displacement at the upper monitoring point and the shearing at the lower monitoring point. The over-prediction of the lower monitoring point displacement is mostly responsible for the over-prediction of the upper monitoring point displacement.
3. Generally the Rigid-Body Hybrid model is in better agreement for walls of higher height-to-width ratios.

#### 6.4.4 Examination of corner deformation

One of the likely causes of disagreements between the Rigid-Body Hybrid model and experimental or FE model results is the assumption that the lower portion of the sidewall above point  $O_1$  in Figure 6.15 (a) does not make contact with the ground in the Rigid-Body Hybrid model. The FE analysis result shows that the lower portion of the sidewall above point  $O_1$  touched the ground for the later part of the movement, as shown in Figure 6.15 (b). Furthermore, this sidewall folding is more extensive for the one-course Mil 1 walls. For taller walls such as the Mil 3 two-course wall, the transition from shear to corner folding is not as influential up to critical rotation because rotations before overturning are less, so the Rigid-Body Hybrid model predicts the response that is in better agreement

for taller walls. Therefore, for the purpose of predicting maximum rotation up to the point of overturning, the Rigid-Body Hybrid model is sufficient for taller walls.

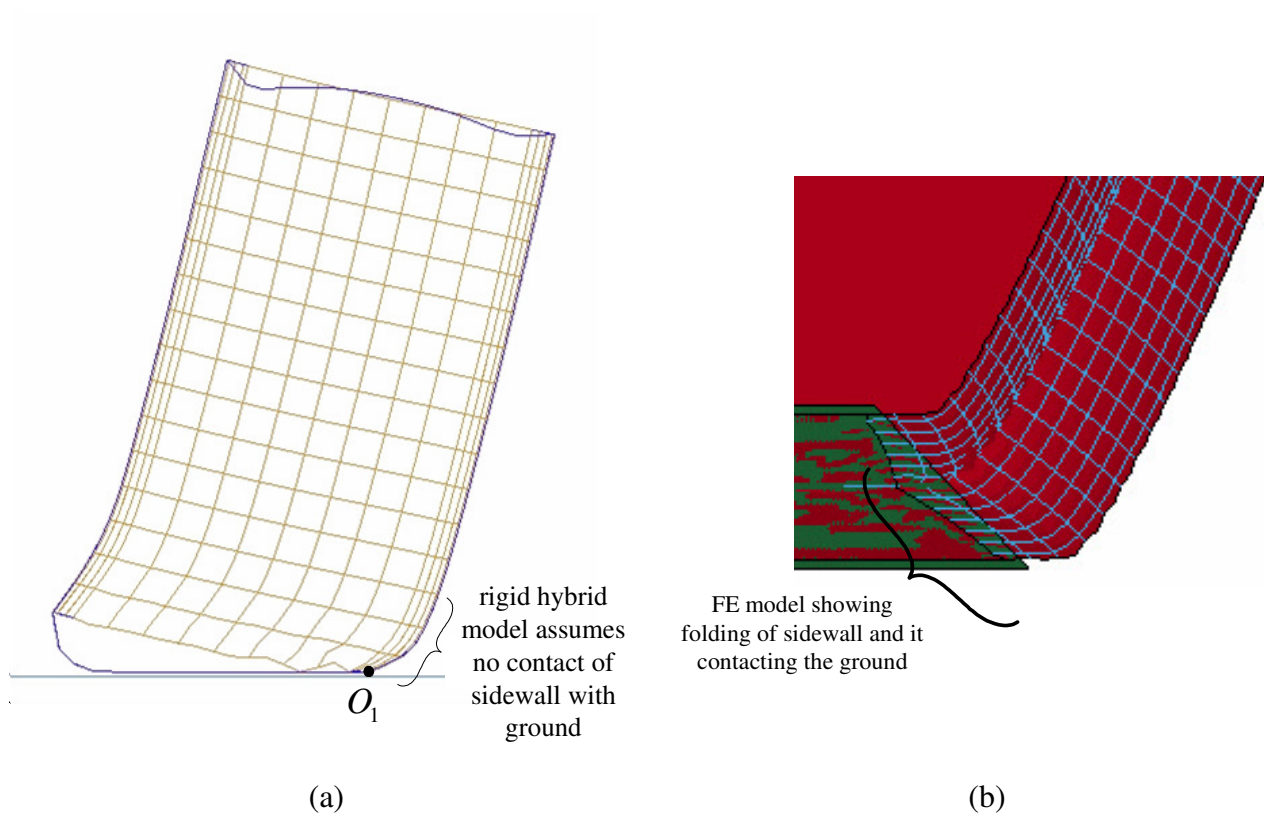


**Figure 6.15 Comparison between assumption of Rigid-Body Hybrid model and result of FE model:**

**(a) Rigid-Body Hybrid model showing no contact of sidewall right of point  $O_1$ , (b) FE model showing contact of sidewall with ground through folding**

A more detailed look at the trends encountered for different height-to-width ratios of walls will be discussed in Section 6.6.

#### 6.4.5 Soil sensitivity comparison

Unlike the Rigid-Body Rotation model where only soil density is considered, the Rigid-Body Hybrid model incorporates soil properties in the prediction of the wall response. This section investigates the effect of the soil properties on the calculated displacement–time history of an HB wall subjected to blast loading and compares the results of the Rigid-Body Hybrid model with the FE model. Trial 6 was selected as an example for this investigation because the results of the Rigid-Body Hybrid model and the FE model, and the experimental results were in good agreement with one another for this experiment (within 10 % for the horizontal displacement-time histories), and that this experiment consisted of a taller height-to-width ratio of wall with a fill of little cohesion. Figure 6.16 (a) illustrates the effects that the change in the bulk modulus  $K$  used in the calculation has on the displacement–time history of the HB wall. It can be seen from the figure that, by varying the values of  $K$  to  $0.5K$  and  $2K$ ; the displacement–time history of the HB wall remains almost the same in both the FE model and Rigid-Body Hybrid (RBH) model. The magnitude of change in the Rigid-Body Hybrid model agrees with the FE model. Figure 6.16 (b) shows the effects that the change in the slope of the EOS has on the displacement–time history of the HB wall. The variation of the slope of the EOS does not contribute to the HB wall response in the FE model, but affects the response of the Rigid-Body Hybrid model by  $\pm 5$  %. In Figure 6.16 (c) the change in the slope of the yield relationship alters the response of the HB wall in the FE model and Rigid-Body Hybrid model to a similar magnitude. The reduction of the slope of the yield relation by half increases the displacement up to 20 % while the increase of the slope of the yield relation

to double reduces the displacement up to 20 % in both the FE and Rigid-Body Hybrid model results. The effects that the change in density has on the HB wall response are shown in Figure 6.16 (d).

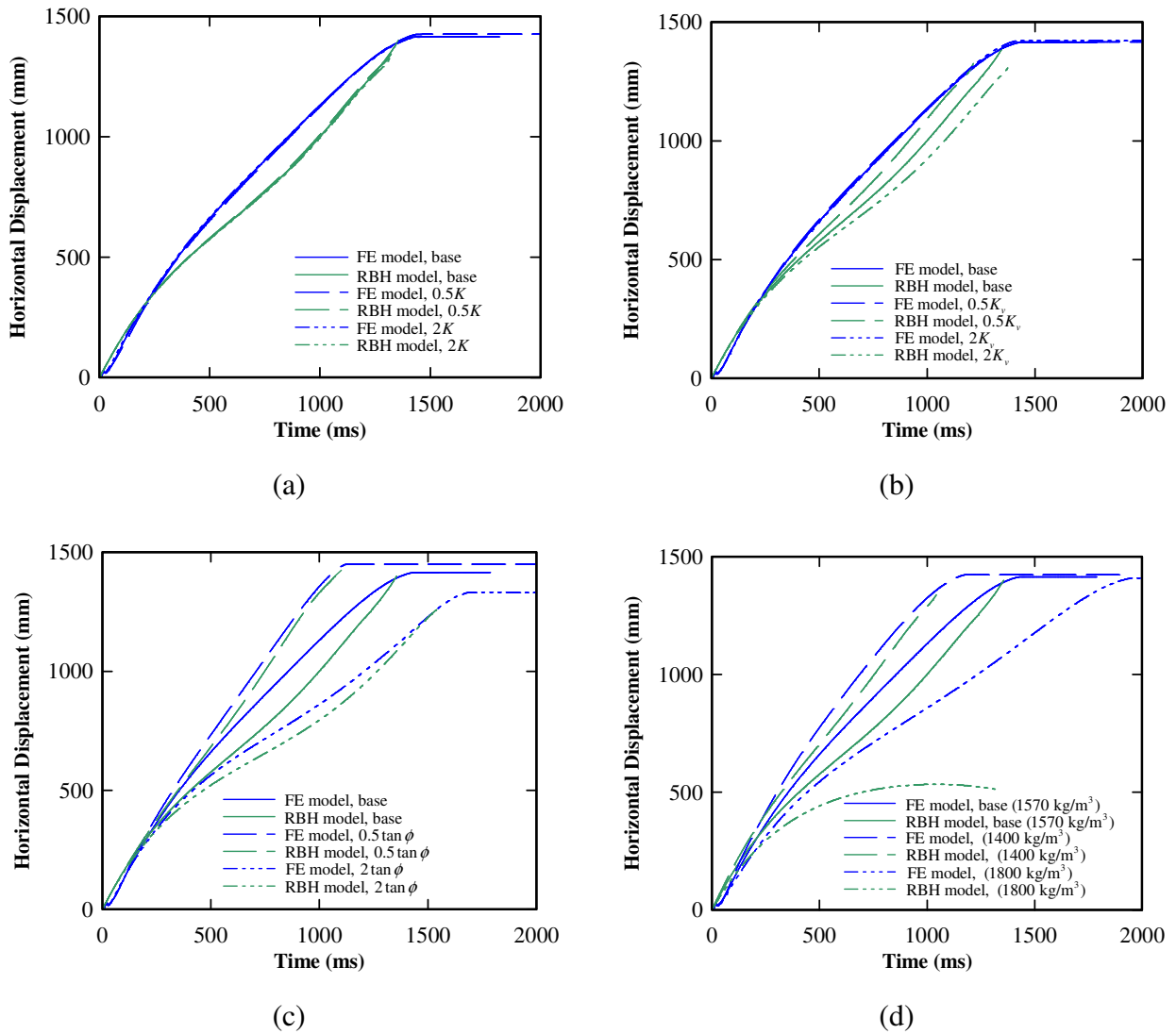


**Figure 6.16 Comparison of Rigid-Body Hybrid (RBH) model to FE model in capturing changes in response to different soil parameters: (a) for  $K$ , (b) for EOS slope  $K_v$ , (c) for slope of yield relation  $\tan \phi$ , and (d) for density**

The increase in the density of the soil decreases the displacement of the HB wall. This is because the increase in the density of the soil increases the rotational inertia of the wall. Both the FE and the Rigid-Body Hybrid models show approximately the same changes in response from changes in density. However for a density of  $1800 \text{ kg/m}^3$ , the Rigid-Body Hybrid model did not overturn the wall while the FE model did. This is to be expected as the Rigid-Body Hybrid model overall has slightly more resistance than the FE model.

From the above discussion, the response of the HB wall depends mostly on the density of soil and the slope of the yield relationship. Except for Figure 6.16 (b), the Rigid-Body Hybrid model agrees with the FE model in capturing the magnitude of changes in displacement–time histories from changes in soil properties, and the discrepancy in Figure 6.16 (c) is only moderate ( $\pm 5\%$ ). The proposed Rigid-Body Hybrid model using a 0.1 ms time step took approximately 2.2 seconds to calculate on an Intel Pentium™ IV 2.2 GHz processor with 1 GB RAM while the FE analysis of a single column model using the same computer took approximately 8 hours to calculate.

## 6.5 Calculation and comparison of $P$ – $I$ curves

To compare the analytical models with the FE model for a range of combinations of peak pressures and impulses,  $P$ – $I$  curves were calculated assuming the damage criteria of overturning. The soil properties for Set 2 were considered, which are:

$$\begin{aligned} \rho &= 1570 \text{ kg/m}^3, & K_v &= 20740 \text{ kPa}, & c &= 1.797 \text{ kPa}, \\ \phi &= 26.15^\circ, & K &= 163.3 \text{ MPa}, & G &= 8.3 \text{ MPa} \end{aligned} \quad (6.11)$$

$P-I$  curves were constructed for the three configurations of walls presented in the experimental section: a Mil 3 two-course wall, a Mil 2 two-course wall, and a Mil 1 one-course wall, which have the following geometrical parameters.

$$\text{Two-course Mil 3 wall: } w_a = 0.975 \text{ m, } w_b = 1.2 \text{ m, and } H = 1.95 \text{ m.} \quad (6.12)$$

$$\text{Two-course Mil 2 wall: } w_a = 0.6 \text{ m, } w_b = 0.74 \text{ m, and } H = 1.2 \text{ m.} \quad (6.13)$$

$$\text{One-course Mil 1 wall: } w_a = 1.05 \text{ m, } w_b = 1.33 \text{ m, and } H = 1.35 \text{ m.} \quad (6.14)$$

The reflected wave pressure profile assumed in the model to calculate all  $P-I$  diagrams was the exponentially decayed distribution from Eq. (2.3). The time step selected was 1/20 ms for calculating the  $P-I$  diagrams for both the Rigid-Body Rotation model and Rigid-Body Hybrid model, which satisfied convergence of results. Since the exact point of overturning is a point of instability (i.e. cannot be achieved because either overturning occurs or it does not), typical root solving algorithms are difficult to employ. Therefore the motion of the wall for a given peak pressure was evaluated initially for two quantities of impulse, one quantity that overturned the wall and one that did not. The difference between these two quantities of impulse was repeatedly bisected according to the outcome of successive numerical calculations. Bisections were conducted until the difference between the two quantities of impulse, one resulting in overturning and one not, were within the desired solution tolerance of 0.01 % for the analytical models. This process was repeated for an entire range of peak pressures to solve for the respective quantities of impulse which constituted the  $P-I$  diagram. Approximately 200 points were used to generate a smooth  $P-I$  curve for both the Rigid-Body Rotation and Rigid-Body Hybrid mod-

els. An additional computer program employing the stated algorithm was coded in Visual Basic to automatically solve for the  $P-I$  diagrams for both of these models.

Since the average calculation time for the FE analysis to produce a result for one pressure-impulse combination was 8 hours, and each  $P-I$  point depending on the level of accuracy desired would take several calculations to solve, it was not feasible to generate a comprehensive  $P-I$  curve consisting of several dozens of points using the FE model. Hence the hyperbolic curve fit Eq. (2.13) was used to fit a  $P-I$  curve through four points that were comprehensively solved for using the FE model. Similar to both of the analytical models, successive bisection was used to solve for these four  $P-I$  points to obtain a result of within 1 % solution tolerance.

The  $P-I$  curves generated for a two-course Mil 3 and Mil 2 wall using all models are shown in Figures 6.17 (a) and (b), respectively. Note that the transition from the impulsive to the dynamic loading realm for this type of structure and mode of deformation occurs at relatively low blast pressures (less than one atmosphere above atmospheric pressure). In order to achieve the impulse associated with a failure at this pressure, the load would have to be applied for several hundreds of milliseconds. When considering conventional high explosives, pressures and durations of this magnitude are only achieved by the detonation of thousands of tonnes of explosive at thousands of metres stand-off from the structure. It follows, therefore, that most conventional loading cases could be dealt with by performing an impulsive analysis - equating the maximum kinetic energy taken-up by the structure to its internal energy developed during deformation (Hulton [48]). In this case there is no requirement to consider the pressure-time history acting on the struc-

ture, but this may not be true of other soil structures that undergo more complicated modes of response. The plots of  $P-I$  for different charge sizes of TNT over a range of stand-offs, generated from the ConWep Program, are also shown in the figures. These plots show that, in practice, the wall will tip over in the impulse dominated realm rather than the pressure dominated realm.

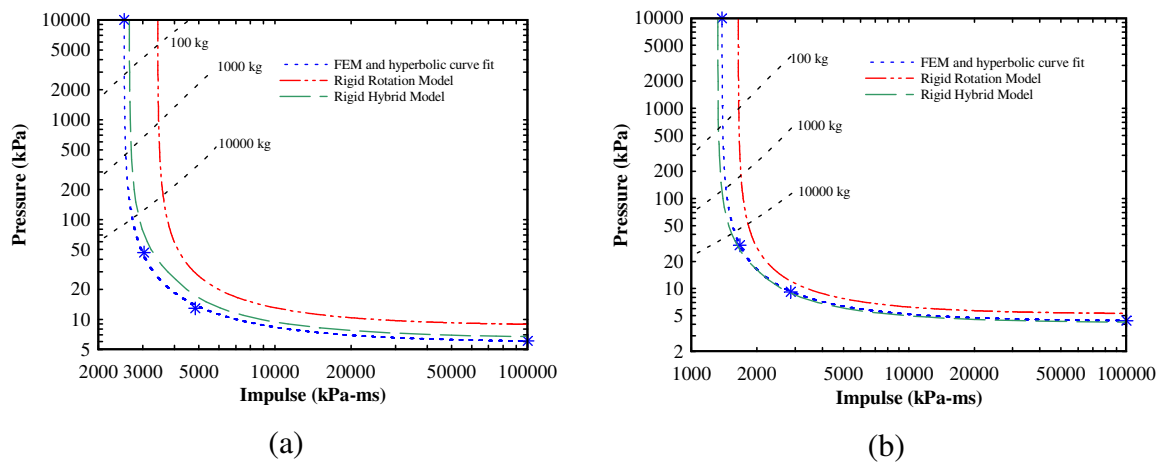


**Figure 6.17  $P-I$  curves calculated from FE and analytical models for failure defined by overturning:**  
**(a) two-course Mil 3 wall, (b) two-course Mil 2 wall**

The  $P-I$  curves for a failure criterion defined by overturning calculated using the Rigid-Body Hybrid model are in very good agreement (within 10 % for both the pressure and impulse asymptotes) with those calculated by the FE model, while the  $P-I$  curves calculated by the Rigid-Body Rotation are significantly higher and to the right. This shows that the Rigid-Body Rotation model possesses much more resistance than the other models. Note that the graph for the Mil 3 wall shows the  $P-I$  curve from the Rigid-Body Hybrid model is located slightly to the right of that from the FE model, while the graph for the Mil 2 wall shows the opposite. This is due to the fact that Mil 2 wall is much smaller than Mil 3 wall, hence greater contribution of the wire mesh towards the stiffness of the corner



lead to a more resistant  $P-I$  curve for the FE model compared to the Rigid-Body Hybrid model. The Rigid-Body Hybrid model only considers the properties of the soil and does not consider the contribution of the wire mesh, which has greater influence on the response of smaller walls. However the difference is relatively small. At the approximate intersection of the 1000 kg charge line with the  $P-I$  curves of the FE model, Figure 6.17 (a) shows approximately a + 4.8 % difference of impulse between the Rigid-Body Hybrid model and FE model  $P-I$  curve, while Figure 6.17 (b) at the 1000 kg intersection shows approximately - 4.2 % difference. These differences do not change much if the 100 kg or 10000 kg charge line intersections are considered. The spread of these differences (approximately 9 %) constitutes a measure of the differences in contribution of the wire mesh between the two-course Mil 3 wall and Mil 2 wall. Therefore it is recommended that the model be extended to consider the contribution of the wire mesh towards stiffening the corner deformation if greater accuracy is desired. Despite these small differences, overall, the Rigid-Body Hybrid model and FE model  $P-I$  curves are in very good agreement with one another (within 10 % for both the pressure and impulse asymptotes).

The generation of a  $P-I$  curve for the one-course Mil 1 wall using the FE model was not possible, specifically because the FE model of the Mil 1 wall would not overturn completely. The following Figures 6.18 (a) through (c) show the different final positions of the Mil 1 one-course wall resulting from increasing loadings. Due to the substantial deformation at the lower corner, the Mil 1 wall did not overturn completely. For increased loading, the level of sidewall contact with the ground was increased, while the upper portion of the sidewall although increasing in rotation angle, maintained a residual angle. A

concise definition of overturning is not possible and any definition proposed for these cases would be debatable.

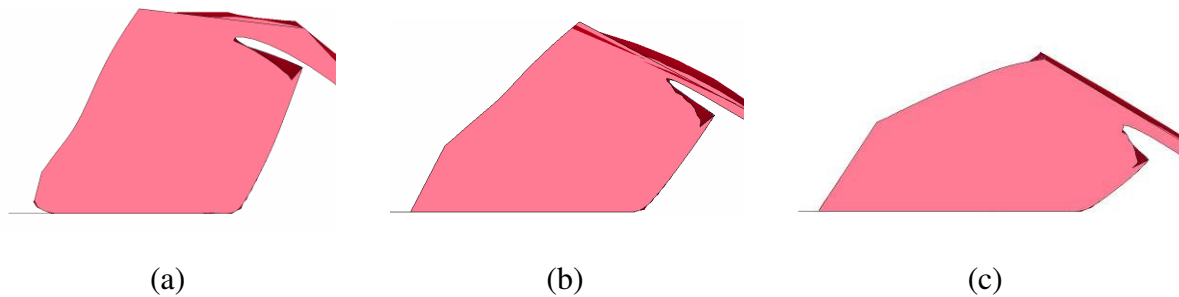


**Figure 6.18** Final positions of FE model for one-course Mil 1 wall resulting from different impulses which illustrate inability to overturn completely: (a) 21° rotation, (b) 36° rotation, (c) 50° rotation

Concerning the Rigid-Body Hybrid model, although an exact critical rotation angle does not exist for the model because it depends on the time-dependent compression and shear of the corner, for impulsive loading it was empirically found that the critical angle to produce overturning for the Mil 1 wall using the Rigid-Body Hybrid model was approximately 21° of rotation. Recall that as explained in Subsection 2.3.2, it is up to the individual to determine suitable failure criteria, which can be any type of deflection or damage. And in this case, overturning is not clearly defined in the FE model and therefore a  $P-I$  curve cannot be generated for overturning using the FE model. However, 21° of rotation is a concise definition. Thus the  $P-I$  curve for the FE model and analytical models were iteratively calculated for 21° of rotation, and the results are shown in Figure 6.19.

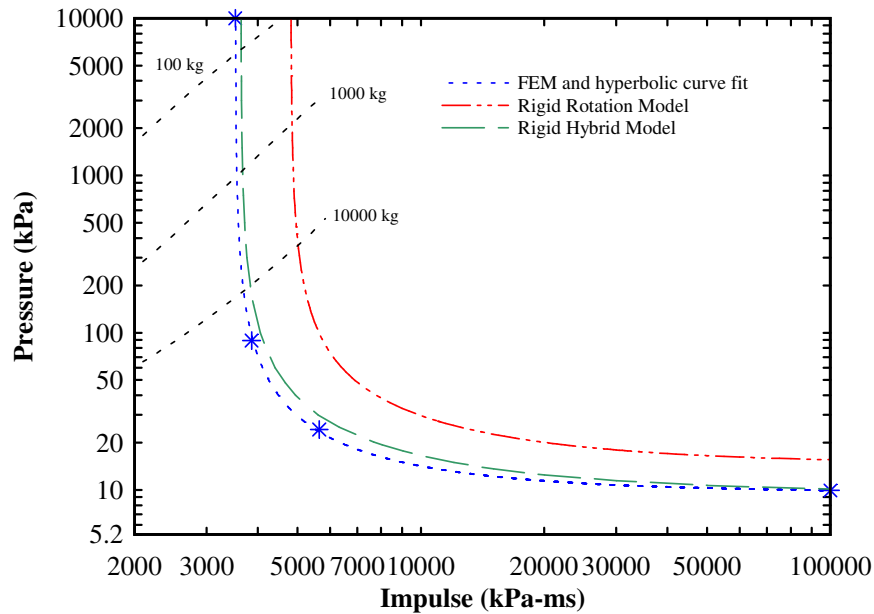


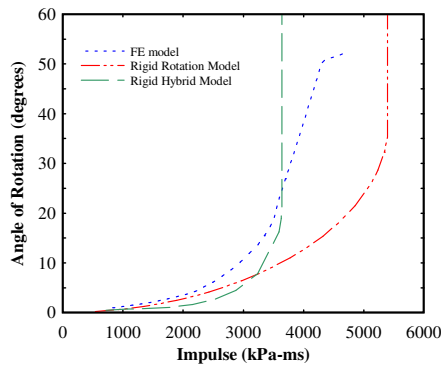
**Figure 6.19  $P$ – $I$  curve for one-course Mil 1 wall for failure defined by  $21^\circ$  rotation**

It can be seen that excellent agreement (within 5 %) was achieved between the FE model and Rigid-Body Hybrid model. Similar to the previous cases, the  $P$ – $I$  curve calculated using the Rigid-Body Rotation model was substantially higher and to the right of the others. Solving for four points on the  $P$ – $I$  curve to within 1 % tolerance using the FE model took approximately 200 hrs of computation effort on a single 2.2 GHz Intel Pentium™ processor. Each 200-point  $P$ – $I$  curve generated by the Rigid-Body Hybrid model took approximately 45 minutes of computation using the same processor, while the Rigid-Body Rotation model took approximately 15 minutes. The results demonstrated that the proposed Rigid-Body Hybrid model can be used to generate the  $P$ – $I$  diagram for a HB wall both efficiently and accurately.

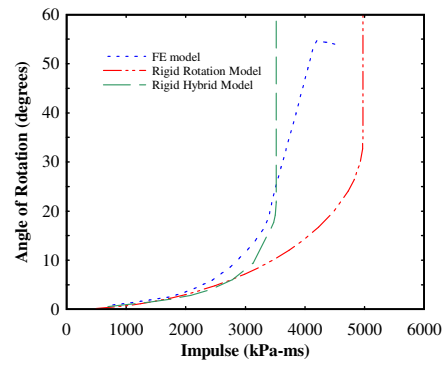
## 6.6 Aspect ratio study and analytical model limitations

To help assert the limits of application of the analytical models, a study was undertaken to examine the results of the analytical models and the FE model across a range of different height to empty-dimension width ( $H / w_a$  in Figure 5.1 (b)) or aspect ratios of walls throughout a range of impulsive loadings. The one-course Mil 1 dimensions were assumed as the basic model, which has an aspect ratio of 1.29. Six different aspect ratio walls were examined, where the 1.35 m height in the basic model was extended in 0.15 m increments up to 2.1 m high. A range of impulses from 20 % to approximately 130 % of the critical loading (predicted by the Rigid-Body Hybrid model) were used to load each model and rotation angles were recorded. Only impulsive loading was investigated because, as established previously, the HB walls tend to be impulsively loaded for charge sizes below 10000 kg. The soil properties from Trial 4 through 7 were used for the study, (the soil possessed very little cohesion). The results are shown in Figures 6.20 (a) through (f).

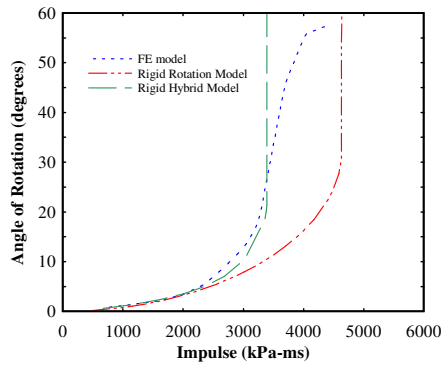
As mentioned previously, the point of critical overturning is an instability, and this results in vertical asymptotes shown for both analytical models in all the figures. But for the shorter aspect ratio walls calculated using the FE model, due to the models inability to overturn the asymptotes are not clear. This is evident in Figure 6.20 (a) and (b). The asymptotes for the FE model become clearer in Figure 6.20 (e) and (f) for the taller aspect ratio walls.



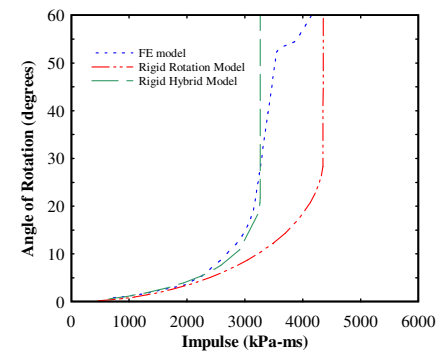
(a)



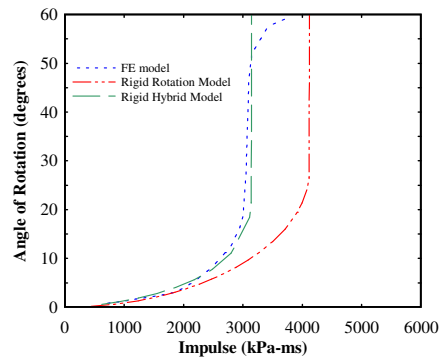
(b)



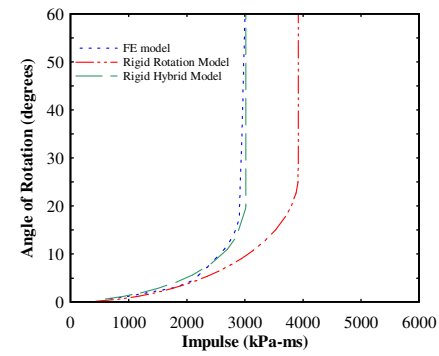
(c)



(d)



(e)



(f)

**Figure 6.20** Rotation as a function of impulse for a range of  $H/w_a$  ratios: (a)  $H/w_a = 1.29$  (b)

$H/w_a = 1.43$ , (c)  $H/w_a = 1.57$ , (d)  $H/w_a = 1.71$ , (e)  $H/w_a = 1.86$ , (f)  $H/w_a = 2.0$

In all graphs the Rigid-Body Rotation model offers predictions within 20 % up to  $8^\circ$ , but under predicts rotation angles beyond that. Furthermore it predicts larger critical angles before overturning, and over-predicts the critical overturning impulse in comparison with the Rigid-Body Hybrid and FE models by approximately 35 % for lower aspect ratio walls and 20 % for higher aspect ratio walls, shown in Figure 6.20 (a) and (e), respectively. From this study concerning different heights for the Mil 1 width ( $w_a = 1.05$  m) of walls, the Rigid-Body Rotation model is only suitable for smaller angles of rotation ( $8^\circ$  or less). Recall that the simulation of Trial 3 using the Rigid-Body Rotation model showed excellent agreement for a rotation angle of approximately  $12^\circ$ . This is in contradiction to the limitation of  $8^\circ$  established for this study. But the wall in Trial 3 used was a Mil 2 wall ( $w_a = 0.6$  m), where increased contribution of stiffness from the wire mesh occurs due to the smaller cell size (as explained previously in the comparison of Figures 6.17 (a) and (b)). This increased contribution of stiffness from the wire mesh causes the walls of smaller cell sizes to act more like rigid bodies, and is responsible for increased agreement of the Rigid-Body Rotation model in Trial 3. Thus the limitation of  $8^\circ$  is a conservative approximation for the limitation of the Rigid-Body Rotation model, and in view that it is impossible to extend this model to adjust for the stiffness of the wire mesh, it is recommended that this study be extended to walls of smaller cell sizes.

In Figure 6.20 (a) ( $H/w_a = 1.29$ ), the Rigid-Body Hybrid model under-predicts the rotation by as much as 70 % in comparison with the FE model, apart from the region near its critical rotation (between  $18^\circ$  and  $21^\circ$ ). Citing the narrow range of validity, use of the Rigid-Body Hybrid model for walls  $H/w_a \leq 1.29$  is not recommended. The predictions in

rotations from both the models: the Rigid-Body Hybrid model and the FE model; are within 20 % for Figure 6.20 (b) ( $H/w_a = 1.43$ ) and they are within 5 % for higher aspect ratio walls such as in Figure 6.20 (e) and (f) ( $H/w_a = 1.86$  and  $2.0$ ). Similarly, for the prediction of the amount of impulse producing overturning, excellent agreement (within 5 %) between the Rigid-Body Hybrid model and FE model is shown for higher aspect ratio walls. For lower aspect ratio of walls the Rigid-Body Hybrid model is within 10 % of the FE model (Figure 6.20 (b) ( $H/w_a = 1.43$ )), with the exception that the Rigid-Body Hybrid model predicts critical overturning while the FE model does not. This is the only substantial disagreement in these model results.

However there is no experimental evidence to verify that the FE model of the Mil 1 wall does not overturn but only increases in rotation as shown in Figure 6.18 (b) and (c). Figure 6.21 (a) shows the result of Trial 7, while Figure 6.21 (b) shows the modelled result. The modelled result upon coming to rest has a residual angle of approximately  $60^\circ$  at the upper sidewall. Although difficult to distinguish in from the post-experiment photo in Figure 6.21 (a), the experimental wall did not have any residual angle. This was verified by a post-experiment investigation of the wall, where the wire mesh of the wall was found to be lying flat on the ground. The difficulties of the FE models of shorter aspect ratio walls to overturn may not be realistic.



**Figure 6.21 Comparison of post-experimental wall positions for Trial 7: (a) experiment result, (b) final FE model result showing residual angle of top of sidewall at approximately  $60^\circ$**

In view of this experimental evidence, deficiencies in the FE model are likely responsible for the disagreement of the Rigid-Body Hybrid model with the FE model in predicting overturning. Therefore an acceptable valid range for use of the Rigid-Body Hybrid model for the Mil 1 thickness is  $H/w_a \geq 1.43$ . Although an additional study could be conducted for HB walls of cell thicknesses smaller than the Mil 1 thickness to determine the valid limits of the model, considering that the results presented in Figures 6.20 (a) through (f) consisted more than 100 FE calculations, it may be more productive to first attempt to improve the model by considering the contribution of stiffness from the wire mesh. But this modification to the model would likely only improve its accuracy for smaller HB cell sizes but not improve its accuracy for  $H/w_a$  ratios of 1.29 and lower. The consideration of folding of the sidewall at the corner of rotation would have to be considered in the model for increasing accuracy for lower  $H/w_a$  ratios of HB walls.



# Chapter 7

## Conclusions and Recommendations

The aims of the thesis were to study the response of HB walls both experimentally and numerically, and to develop an efficient and accurate analytical or semi-analytical model to predict 2-*D* planar response from blast loading and which can be used to efficiently calculate a *P-I* curve. To gain understanding of blast loading, an introduction to blast phenomenology was provided. Seven full-scale experiments consisting of blast loading simple free-standing soil-filled HB walls were presented. Soil densities and moisture contents were measured in the field, and soil properties were obtained from triaxial tests of the samples collected and prepared to match field conditions.

An explicit FE formulation was constructed using LS-Dyna. Two analytical models were also derived and presented: a Rigid-Body Rotation model as a preliminary model, and the Rigid-Body Hybrid model as the proposed model of this thesis. The Rigid-Body Rotation model was derived based on observation of the primary response mode of the walls from FE models, rigid-body rotation. The Rigid-Body Hybrid model was derived based on considering rigid-body rotation as well as local compression and shear at the base of the wall. The deformation and forces at the base were modelled using distributed springs at

the base of the wall, where the bottom of the wall was assumed as deformable and resting on rigid ground. Properties for the distributed springs were derived from the EOS and bulk modulus of the filled soil. The shear force was calculated from the base reaction force using the Mohr-Coulomb yield relationship derived from soils tests, and the shear stress-strain relationship was assumed to be perfectly plastic.

Both analytical models as well as the FE model were compared with the experimental results and with one another in additional analytical studies. All models used some or all of the derived soil properties pertinent to the experiments as input, and assumed the recorded pressure-time histories in the experiments as the loadings. Following the comparison of all three models with the experimental final rotations and displacement–time histories, the results of the FE model, Rigid-Body Rotation model and Rigid-Body Hybrid model were discussed. Additional comparisons between the models were conducted such as examining the sensitivity to soil properties, comparing the  $P$ – $I$  curves calculated, and comparing the model performance for different height-to-width ratios of walls. Limitations of both analytical models were established and recommendations were provided to improve the proposed Rigid-Body Hybrid model.

Examination of the FE model led to the following conclusions:

- The results of the FE models were compared to the results of the seven experiments and were found to be in very good agreement (within 10 %) in both the post-experiment deformation and the displacement–time histories.

- Several sources of error were examined and found to have insignificant effects on the model performance.
- The effect of varying soil properties was examined and the FE model was found to be most sensitive to changes in the slope of the yield relationship and moderately sensitive to changes in density. The other parameters examined (Bulk and shear modulus, slope of the Equation of State) were found to have little effect on the results.
- For single course Mil 1 walls that are loaded enough to cause large rotations, the walls do not show overturning but only increased rotation with excessive corner deformation. However limited experimental evidence shows overturning which contradicts the behaviour of the FE model.

Overall the FE model was in very good agreement with the experiments and was valuable in providing insight into the behaviour of the HB walls to help formulate the analytical models.

The following conclusions and recommendations were postulated based on the results of the Rigid-Body Rotation model:

- It was found that the rotation response predicted by the Rigid-Body Rotation model was in reasonable agreement for the post-experimental deformation in cases where the wall did not critically overturn but sustained moderate rotation angles.

- The displacement–time histories calculated by the Rigid-Body Rotation model were underestimated in comparison with the experiment results for soils of little cohesion, which implied that the model possessed too much resistance. This was because the model did not account for compression and shear behaviour at the base of the wall, which becomes increasingly influential for large rotations.
- Investigating the analytical solution for impulsive loading showed that the response of the wall was very sensitive to small changes in impulse if the rotation approached critical rotation angles. This behaviour presents difficulties in planning experiments where moderate to large rotation angles are desired without overturning.
- Investigating the analytical solution also showed that increases in compacted fill density can increase the resistance of HB walls to overturning, but the increases in the resistance are not comparatively large.
- Comparison of the  $P-I$  curves calculated using the Rigid-Body Rotation and FE model showed that the Rigid-Body Rotation model possessed too much resistance, and for charge sizes below 10000 kg overestimate the critical overturning impulse by 20 to 35 % depending on the height-to-width ratio of wall.
- Using the Rigid-Body Rotation model a 200 point  $P-I$  curve was solved in 15 minutes, where each point was solved to a tolerance of 0.01 %. To solve for four points within 1 % tolerance using the FE model took several days of calculation time using the same Intel Pentium™ IV 2.2 GHz processor.

- The Rigid-Body Rotation model is in better agreement with experiments for walls of smaller cell sizes, where the added contribution of stiffness from the wire mesh causes the experimental walls to behave more like rigid-bodies.
- Comparison with the FE model for different height-to-width ratios of walls showed that the Rigid-Body Rotation model was in reasonable agreement (within 20 %) up to rotation angles of 8 °. For rotations beyond 8 ° it overestimated resistance to rotation and overturning because of failure to consider corner deformations. Note that the recommendation of 8 ° was based on the Mil 1 wall thickness, and an additional study would have to be conducted for a wall of a smaller cell size. Due to increased contribution of stiffness from wire mesh for smaller cell sizes, it is expected that the model would be valid for higher rotation angles. A separate study would have to be conducted to determine the limit, however, an experimental comparison in Trial 3 for a Mil 2 wall showed validity at 12 ° rotation.

The addition of local corner deformations resulted in the Rigid-Body Hybrid model. The following conclusions and recommendations were drawn from examination of the Rigid-Body Hybrid model:

- The response of the proposed Rigid-Body Hybrid model was compared with the post-experimental position of the walls and overall very good agreement (averaging within 10 %) was achieved with the exception that modest disagreement (30

%) was reached in comparison to an experiment where a cohesive soil-fill was used.

- Cohesion causes sliding to become the dominating behaviour instead of internal shear. Note that the present model only considers internal shear and not sliding. A general recommendation for future model development follows that a sliding interface should be included in the model to capture behaviour arising from use of soil-fills with substantial cohesion.
- The response calculated from the Rigid-Body Hybrid model was in good agreement with the experimentally recorded displacement–time histories for three out of four experiments, only slightly under-predicting the rates of displacement. The experiment that the Rigid-Body Hybrid model was not in good agreement with sustained loading that was far beyond the critical overturning loading, which had influenced the behaviour of the model.
- Displacement–time histories for the model were in better agreement with experiments in the early time histories compared with the later time histories. Also better agreement was shown for taller height-to-width ratio walls than shorter height-to-width ratio walls. The likely source of disagreement was that considering the walls overturned, sidewall folding and contact with the ground in the late time history became increasingly influential. Consideration of this behaviour in the model would help to further improve the results.

- Excellent agreement was reached between the Rigid-Body Hybrid model and the FE model in its ability to capture differences in displacement–time histories from differences in the yield slope, soil-fill density, and bulk modulus. The only discrepancy was that the slope of the EOS led to slight to moderate differences in the responses of the Rigid-Body Hybrid model but correspondingly little differences in the response of the FE model. Overall, the Rigid-Body Hybrid model was able to capture the changes in response from changes in soil properties in very good agreement with the FE model.
- Comparison of  $P$ – $I$  curves generated using the Rigid-Body Hybrid model compared to the FE model showed excellent agreement. For charge sizes below 10000 kg which defines the region that is largely independent of peak pressure, the difference in critical overturning impulse between both models differed by less than 5 %.
- Comparison of the locations of the Rigid-Body Hybrid Model  $P$ – $I$  curve for the two-course Mil 3 wall and Mil 2 wall showed that the curve for the Mil 2 wall showed slightly too little resistance while the Mil 3 wall showed slightly too much resistance. This was due to the greater contribution of stiffness from the wire mesh for the smaller cell size of the Mil 2 wall which the FE model considers but the Rigid-Body Hybrid model does not. The stiffness of the wire mesh is more influential for the smaller HB wall cell sizes such as the Mil 2.

- The Rigid-Body Hybrid model was also very efficient (fulfilling the objective of the thesis) calculating a 200 point  $P-I$  curve in 45 minutes, where each point was solved to a tolerance of 0.01 % while to solve for four points on a  $P-I$  curve to 1 % tolerance using the FE model took several days of calculation time using the same Intel Pentium™ IV 2.2 GHz processor.
- Comparison with the FE model for different height-to-width ratios of walls showed that the Rigid-Body Hybrid model was in within 10 % for all rotation angles and predictions of critical overturning for height-to-width ratios of walls  $H/w_a \geq 1.43$ . For walls  $H/w_a = 1.29$  the Rigid-Body Hybrid model was only in agreement for rotation angles from 18 to 21 degrees. In view of this narrow range of accuracy, use of the model for walls  $H/w_a \leq 1.29$  in its existing form is not recommended. Consideration of sidewall folding and contact with the ground may help to improve its accuracy for walls  $H/w_a \leq 1.29$ . Note that these conclusions were based on the Mil 1 wall thickness, but it is expected that similar conclusions would be reached for thinner walls such as the Mil 2 thickness.

Overall, the Rigid-Body Hybrid model is in very good agreement (within 10 % on average) with experimental results and FE model results despite minor disagreements. Further investigations of the following points are recommended in order to improve the Rigid-Body Hybrid model and extend the range of its validity:

- Consideration of sliding at the base to improve results for walls with cohesive soil-fill in the model.



- Consideration of folding of the sidewall and its contact with the ground within the model.
- Consideration of the contribution of bending stiffness from the wire mesh sidewall in the calculation of resistance to shear deformation at the base of the wall.
- Further experimental investigation to resolve whether the inability of the FE model to overturn is realistic for smaller aspect ratio walls, and if so, considering additional response mechanisms within the model that may become more dominant for these small aspect ratio walls.
- Determination of why the Rigid-Body Hybrid model is more sensitive to changes in the slope of the EOS compared with the FE model.

# Bibliography

- [1] HESCO Bastion concertainer® 2009. Citing on line sources: <http://www.hescobastion.com/> [cited 5 January 2009].
- [2] Instomat. Citing on line sources: <http://www.khaleejdubai.com/Instomat.html/> [cited 5 January 2009].
- [3] Dynawall, TFL Defence Ltd. Citing on line sources: <http://www.tfldefence.com/a04-03.html/> [cited 5 January 2009].
- [4] Pope DJ, Scherbatiuk K, Fowler J. The use of finite element analysis to generate pressure-impulse diagrams for temporary soil structures. Proceedings of the 6th Asia-Pacific Conference on Shock and Impact Loads on Structures. Perth, Australia, 2005; 457-464.
- [5] Henrych J. The dynamics of explosions and its use. New York: Elsevier, 1979.
- [6] Cooper PW. Explosives engineering. New York: Wiley-VCH, 1996.
- [7] Kinney GF, Graham KJ. Explosive shocks in air. New York: Springer-Verlag, 1985.
- [8] Fickett W, Davis WC. Detonation: theory and experiment. New York: Dover: 1979.
- [9] Baker WE. Explosions in air. Austin, TX: University of Texas Press, 1973.

- [10] Gelfand BE, and Silnikov MV. Explosions and blast control. St. Petersburg, Russia: NPF Asterion, 2004.
- [11] US Department of the Army Technical Manual. TM5-1300. Design of Structures to Resist the Effects of Accidental Explosions. Washington, D.C., 1990.
- [12] Watson AJ. In: Kappos AJ, editor. Dynamic Loading and Design of Structures. New York: Spon Press, 2002.
- [13] Hopkinson B. British Ordnance Board Minutes 13565, 1915.
- [14] Sachs RG. The dependence of blast on ambient pressure and temperature. BRL Report No. 466, Aberdeen Proving Ground, Maryland, USA, 1944.
- [15] Kingery CN, Bulmash G. Air blast parameters from TNT spherical air bursts and Hemispherical surface bursts. USARDC, Aberdeen proving ground, technical report ARBRL-TR-02555, 1984.
- [16] Remennikov AM. The state of the art of explosive loads characterisation. Proceedings of the Australian Earthquake Engineering Society (AEES). Wollongong, Australia, 2007.
- [17] Hyde DW. Conventional weapons program (ConWep). US Army Waterways Experimental Station. Vicksburg, USA, 1991.
- [18] Tedesco JW, McDougal WG, Ross CA. Structural Dynamics: Theory and Applications. Menlo-Park, California: Addison-Wesley, 1999.
- [19] Biggs JM. Introduction to structural dynamics. London, UK: McGraw-Hill, 1964.
- [20] Baker WE, Cox PA, Westine PS, Kulesz JJ, Strehlow RA. Explosion hazards and evaluation. New York: Elsevier; 1983.

- [21] Li QM, Meng H. Pressure–impulse diagram based on dimensional analysis and single-degree-of-freedom model. *ASCE J Eng Mech* 2002; 128(1): 87–92.
- [22] Oswald CJ, Skerhut D. FACEDAP theory manual Version 1.2. Omaha, Nebraska: US Corps of Engineers Omaha District; 1994.
- [23] Scherbatiuk K, Pope D, Fowler J, Fang J. Effect of silty-sand compressibility on transferred velocity from impulsive blast loading. In: *Structures under shock and impact IX*, New Forest, UK. 2006; 73–83.
- [24] Scherbatiuk K, Rattanawangcharoen N, Pope DJ, Fowler J. Generation of a pressure-impulse diagram for a temporary soil wall using an analytical rigid-body rotation model. *Int J Impact Eng* 2008; 35(6): 530–9.
- [25] Scherbatiuk K, Rattanawangcharoen N. Experimental testing and numerical modeling of soil-filled concertainer walls. *Engineering Structures* 2008; 30(12): 3545–54.
- [26] Scherbatiuk K, Rattanawangcharoen N. A hybrid rigid-body rotation model for predicting a response of a temporary soil-filled wall subjected to blast loading. *Int J Impact Eng* 2010; 37(1): 11–26.
- [27] Zhang J, Makris N. Rocking response of free-standing blocks under cycloidal pulses. *ASCE J Eng Mech* 2001; 127(5): 473–83.
- [28] Van Leeuwen MJJ. The Domino effect. *arXiv:physics/0408018v1*, 2004.
- [29] Houlsby GT, Cassidy MJ, Einav I. A generalised Winkler model for the behaviour of shallow foundations. *Géotechnique* 2005; 55(6): 449–60.

- [30] Rose TA, Smith PD, Mays GC. Protection of structures against airblast using barriers of limited robustness. *Proc Inst Civil Eng Struct Buildings* 1998; 128(2): 58–167–76.
- [31] Wang Z, Yong L, Hong H. Numerical investigation of effects of water saturation on blast wave propagation in soil mass. *ASCE J Eng Mech* 2004; 130(5): 551–61.
- [32] Laine L, Sandvik A. Derivation of mechanical properties for sand. In: *Proceedings of the fourth Asia-Pacific conference on shock and impact loads on structures*, 2001; 361–8.
- [33] Fišerová D, Hameed A, Rose T, Hetherington J, Hlady S. The use of numerical simulations to analyse soil behaviour and the contribution made to target effects by soil, following the explosion of buried mines. In: *Proceedings of the sixth Asia-Pacific conference on shock and impact loads on structures*, Perth, Australia; 2005.
- [34] Century Dynamics Incorporated. *AutoDyn v6.1*, Concord, CA, USA. 2005.
- [35] Leica Geosystems® 2009. Citing on line sources: <http://www.leica-geosystems.com> [cited 15 January 2009].
- [36] ASTM International. Standard test method for particle-size analysis of soils. (Standard D 422 – 63). In: *Annual Book of ASTM Standards (Vol. 04.08): Soil and Rock (I)*: West Conshohocken, PA (American Society of Testing and Materials); 2002.
- [37] ASTM International. Standard classification of soils for engineering purposes (unified soil classification system). (Standard D 2487 – 90). In: *Annual Book of*

- ASTM Standards (Vol. 04.08): Soil and Rock (I): West Conshohocken, PA (American Society of Testing and Materials); 2000.
- [38] Humboldt Scientific Incorporated. 5001 Series compaction control gauges – Additional instruction manual for the HS-5001C & HS-5001B, Raleigh, NC, USA, 1991.
- [39] ASTM International. Standard test method for standard penetration test (SPT) and split-barrel sampling of soils (Standard D1586 – 08a). In: Annual Book of ASTM Standards (Vol. 04.08): Soil and Rock (I): West Conshohocken, PA (American Society of Testing and Materials); 2003.
- [40] ASTM International. Standard test method for consolidated undrained triaxial compression test for cohesive soils (Standard D4767 – 95). In: Annual Book of ASTM Standards (Vol. 04.08): Soil and Rock (I): West Conshohocken, PA (American Society of Testing and Materials); 2003.
- [41] ASTM International. Standard test methods for laboratory compaction characteristics of soil using modified effort (56,000 ft-lbf/ft<sup>3</sup> (2,700 kN-m/m<sup>3</sup>)) (Standard D 1557 – 02). In: Annual Book of ASTM Standards (Vol. 04.08): Soil and Rock (I): West Conshohocken, PA (American Society of Testing and Materials); 2003.
- [42] ASTM International. Standard test method for unconsolidated undrained triaxial compression test for cohesive soils (Standard D4767 – 02). In: Annual Book of ASTM Standards (Vol. 04.08): Soil and Rock (I): West Conshohocken, PA (American Society of Testing and Materials); 2003; 911–34.

- [43] Jian-Hua YA. Double cell triaxial system for continuous measurement of volume changes of an unsaturated or saturated soil specimen in triaxial testing. *ASTM geotechnical testing journal* 2003; 26(3): 353-358.
- [44] Livermore Software Technology Corporation. *LS-Dyna keyword user's manual*, Livermore, CA, USA, 2003.
- [45] Desai CS, and Siriwardane HJ, *Constitutive laws for Engineering materials with Emphasis on Geological Materials*. New York: Prentice-Hall, 1984.
- [46] Johnson GR and Cook WH. A constitutive model and data for metals subjected to large strains, high strain rates and high temperatures. In: *Proceedings of the 7th international symposium on ballistics*, The Hague, Netherlands; 1983; 115-120.
- [47] Prakash S, *Soil dynamics*. New York: McGraw-Hill; 1981.
- [48] Hulton FG. The Use of Tripartite Protection Systems Against Explosive Attack. *Proceedings of the 7th International Symposium on Interaction of the Effects of Munitions with Structures*. Mannheim, FRG, 1995;1-4.
- [49] Rose TA, Smith PD. An approach to the problem of blast wave clearing using empirical procedures based on numerical simulations. *Proceedings of Military Aspects of Blast and Shock XVI*. Oxford, England, 2000.
- [50] Norris CH, Hansen RJ, Holley MJ, Biggs JM, Namyet S, Minami JK. *Structural design for dynamic loads*. New York : McGraw-Hill, 1959.
- [51] Ben-Dor G. *Shock wave reflection phenomena*. New York: Springer-Verlag, 1992.
- [52] Bryant EJ, Eberhard RA, and Kingery CN. *Mach reflection over hard packed dirt and dry sand*. BRL report No. 809, Aberdeen Proving Ground, 1952.

- [53] Rose TA, Smith PD, Mays GC. The effectiveness of walls designed for the protection of structures against airblast from high explosives. *Proc. Inst. Civil. Eng. Struct. Buildings* 1995; 110(2): 78-85.



# Appendix A

## Detailed Description of the Formation of a Blast Wave in Air

To aid in illustrating how a blast wave is formed in air, a sphere of TNT of a 0.25 m radius and its interaction with the surrounding air was modelled using AutoDyn® Computational Fluid Dynamics software [34]. The formation of shock wave pressure profiles and corresponding particle velocity profiles in the early time history up to a radius of 2 m are shown in Figure A.1 (a) and (b), respectively.

The initial position of the interface of the explosive with the air is labelled on the graph and is the black vertical dashed line. Subsequent vertical dashed lines in colour show the location of the interface of the detonation product gases with the surrounding air at each instance in time. Note that a logarithmic scale was selected so that large ranges in pressures and the details of their profiles could be shown. The absolute pressures are plotted so that any negative gauge pressures could be accommodated on the logarithmic scale. In Figure A.1 at 0.0381 ms, the detonation wave has reached the edge of the explosive and the gas products begin to expand against the surrounding air, labelled point *a*. A large in-

crease in particle velocity results due to the relatively low resistance and inertia of the surrounding air, *b*.

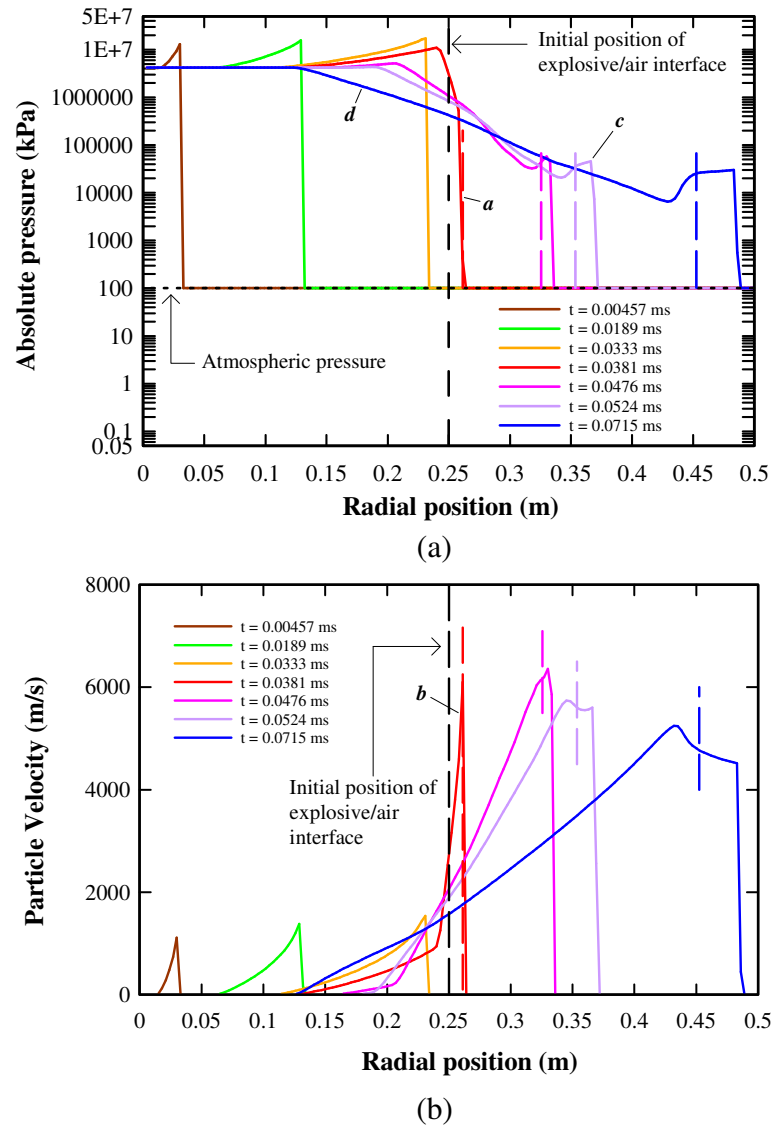


**Figure A.1. Early-time formation of a blast wave: (a) pressure profile (top), and (b) particle velocity profile (bottom)**

A shock front begins to form at 0.0476 ms, *c*, while a rarefaction wave in the detonation products originates from the interface of the detonation product gases and surrounding air resulting from the high outward particle velocity and propagates toward the origin, *d*.

Note that the pressures involved with the detonation are far higher than the pressures within the shock wave in air formed. Figures A.2 (a) and (b) show the later time history across a radial distance of 10 metres.

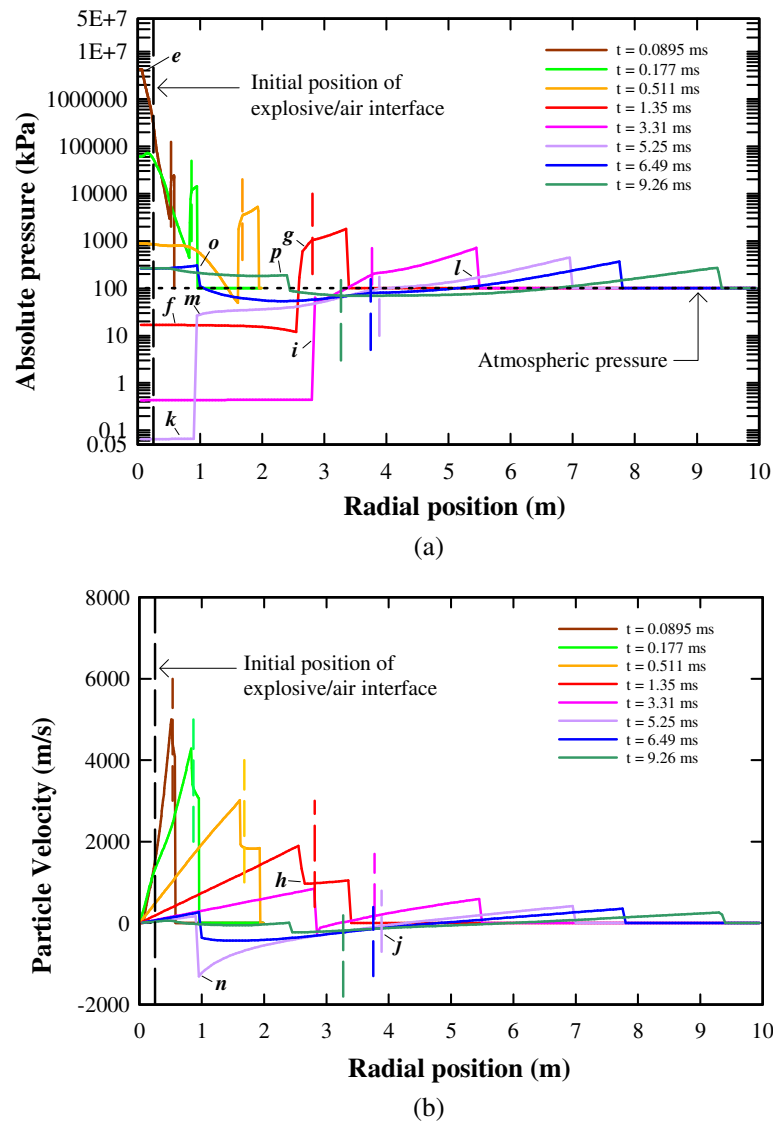


**Figure A.2. Late-time formation of a blast wave: (a) pressure profile (top), and (b) particle velocity profile (bottom)**

The rarefaction wave reaches the origin at approximately 0.0895 ms in Figure A.2 (a), *e*.

The pressure at the origin decreases, and the expansion creates a vacuum in the detona-

tion product gases at 1.35 ms, *f*. At the same time, the high pressure at the interface causes a compression wave in the detonation product gases, *g*, (of a relatively low pressure but strong opposing particle velocity component or gradient against the direction of the expansion), *h*. This wave propagates toward the origin but the propagation of the front of this wave in the inward direction is competing with the overall expansion. The front is not able to move closer to the origin, even though it achieves greater distance from the interface at 3.31 ms, *i*. The interface between the air and the detonation gas products eventually expands to a radius of 4 m at approximately 5.25 ms, *j*, and subsequently begins to contract inward. Note that the particle velocity profile at this time and location crosses the horizontal axis. Also, the detonation gas products have expanded so much at this time as to cause close to zero absolute pressure near the origin, *k*. The positive pressure built up at the interface pushes the interface inward. This causes a rarefaction wave that propagates towards the primary shock wave front, giving it the characteristic decaying shape, *l*. The compression wave originating from the interface and propagating inward within the detonation product gases which was previously unable to overcome the outward expansion, is able propagate towards the centre at 5.25 ms, *m*. Although the pressure is of a negative gauge pressure, the negative particle velocity component (negative represents movement towards the origin) is considerable, *n*. This wave reflects on itself at the origin in compression positive pressure) in the form of a secondary shock wave at 6.49 ms, *o*. The secondary shock, *p*, propagates radially following the primary shock. Figures A.3 (a) and (b) show the pressure and particle velocity time histories, respectively, recorded at 2.5 m, 5 m, 7.5 m and 10 m.

All profiles show the primary shock, followed by a negative phase, followed by a secondary shock. Note the difference between the time history at 2.5 m compared with the others. The time history at 2.5 m was within the region of the expansion of the detonation reactant gas products, (recall that limit of the outward expansion of the gas products was approximately 4 m). The pressure traces at 5 m, 7.5 m, and 10 m were outside of the detonation gas products, and these traces are a consistent shape with one another. This aspect of inconsistency within the range of the detonation gas products is important experimentally as it defines the limit at which blast waves fit a consistent profile.

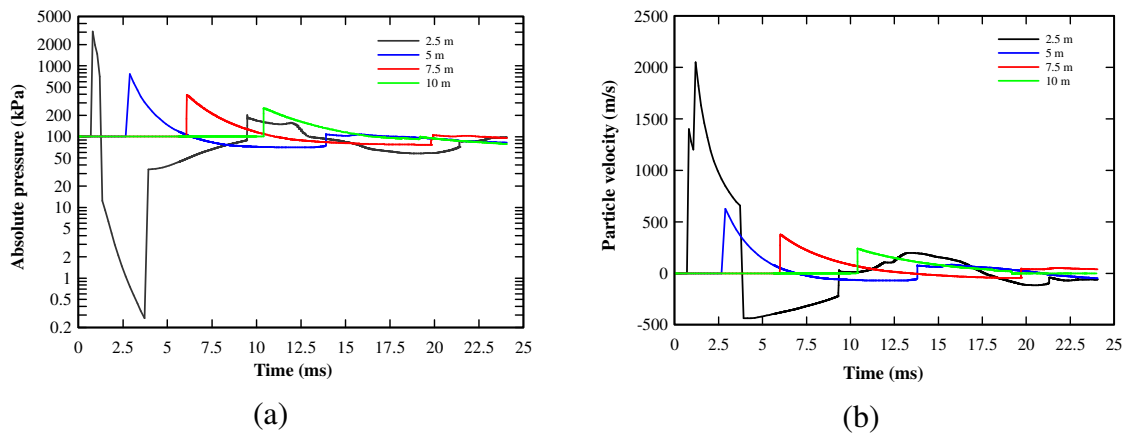


**Figure A.3. Recorded time histories at given distances: (a) pressure history, and (b) particle velocity history**

The discrepancy in the trace at 2.5 m is caused by the extent of the large negative gauge pressures that propagated outward within the detonation product gases, shown by point *f* in Figure A.2 (a), and the limit at which these negative gauge pressures met the compression wave propagating inward, shown approximately by point *i*, which was in competition with the overall outward expansion, reaching slightly beyond 3 m. Henrych [5], gives a practical limit of non ideal blast effects at approximately 10 charge radii. The

limit of non-ideal effects from this analysis was at 3.02 m, which was equivalent to 12.1 charge radii, (corresponding roughly to a spherical scaled distance of  $0.5 \text{ m/kg}^{(1/3)}$ ).

## Appendix B

### Sachs Scaling

Hopkinson-Cranz scaling [13] was extended by Sachs [14] in 1944 to account for the effects of altitude or atmospheric pressure conditions on air blast waves. From the principle of conservation of momentum, at points in distance away from two separate explosion scenarios where the energy released per unit mass of air is the same, the explosive performance parameters can be related with one other. Experimentally generated blast data are typically plotted in terms of their Sachs scaled parameters. The dimensionless Sachs scaled distance, pressure, and impulse is given as:

$$\bar{Z} = \frac{s_o P_{amb}^{1/3}}{E^{1/3}}, \quad (\text{B.1})$$

$$\bar{P} = \frac{P}{P_{amb}}, \text{ and} \quad (\text{B.2})$$

$$\bar{I} = \frac{I a_{amb}}{E^{1/3} P_{amb}^{2/3}}, \quad (\text{B.3})$$

where  $a_{amb}$  is the ambient sound speed of the material, and is calculated by

$$a_{amb} = \sqrt{\gamma \frac{p}{\rho}} = \sqrt{\gamma R T} . \quad (B.4)$$

The parameter  $\gamma$  is the ratio of specific heat capacity of a gas at constant pressure to specific heat capacity of the same gas at constant volume. For air,  $\gamma$  can be assumed as 1.4.

The constant  $R$  is the universal gas constant, and is equal to  $296.86 \text{ J/K}$ .

For a given reference experiment conducted in one set of atmospheric conditions at a standoff  $s_{o1}$ , (pressure and temperature, given by  $p_{amb1}$  and  $T_{amb1}$ , respectively), Sach's scaling principles can also be used to calculate the performance that would result in a different set of atmospheric conditions, (pressure and temperature, given by  $p_{amb2}$  and  $T_{amb2}$ , respectively), at standoff  $s_{o2}$ , where

$$s_{o2} = K_d s_{o1}; \text{ where } K_d = \left( \frac{p_{amb1}}{p_{amb2}} \right)^{1/3}, \quad (B.5)$$

$$P_2 = K_p P_1; \text{ where } K_p = \frac{p_{amb2}}{p_{amb1}}, \quad (B.6)$$

$$t_{a2} = K_t t_{a1}; \text{ where } K_t = K_d \left( \frac{T_{amb1}}{T_{amb2}} \right)^{1/2}, \quad (B.7)$$

$$t_{d2} = K_t t_{d1}, \text{ and} \quad (B.8)$$

$$I_2 = K_I I_1; \text{ where } K_I = K_p K_t = \left( \frac{p_{amb2}}{p_{amb1}} \right)^{2/3} \left( \frac{T_{amb1}}{T_{amb2}} \right)^{1/2}. \quad (B.9)$$

Note that coefficients  $K$  denote factors of scaling. Subscripts  $d$ ,  $p$ , and  $t$  represent distance, pressure, and time. Considering the principle of Sachs scaling, Hopkinson-Cranz scaling can be shown to be a special case of Sachs scaling when atmospheric conditions



between the two explosion scenarios are considered equal, as equal scaled distance in the same atmospheric condition satisfies equal energy release per unit mass of air.

## Appendix C

### Empirical Comparison of Spherical and Hemispherical Charge Performance

A hemispherical configuration is a half-space approximation that is commonly used to estimate hemispherical performance from spherical performance data. A hemispherical charge configuration is important as it may represent a more common threat scenario than a spherical configuration. Owing to symmetry, charge performance should be theoretically identical for a hemispherical configuration of an explosive weight  $W/2$  compared with a spherical configuration of an explosive weight  $W$ . However a caveat to this principle is that the ground is assumed to be perfectly rigid and unyielding, Kinney and Graham [7].

Empirical data shows a slight to moderate decline in explosive performance for the equivalent hemispherical configuration of an explosive weight  $W/2$  due to relief of the loading confinement from yielding of the ground or cratering. It has been estimated that approximately a 20 % loss in energy occurs through cratering and ground shock, Remnikov [16]. Consider the following comparison of empirical results in Table C.1 obtained

from ConWep [17], which is based the on Kingery-Bulmash [15] empirical equations for spherical and hemispherical performance.

**Table C.1: Comparison of half space approximation for sample scenario using ConWep [17]**

Performance Parameter	ConWep empirical (200 kg @ 10 m spherical)	Using half space idealization (100 kg @ 10 m hemispherical)	ConWep empirical (100 kg @ 10 m hemispherical)	Percent Difference
Peak Incident Overpressure (kPa)	276.9	276.9	239.5	-13.5
Peak Incident Positive Impulse (kPa-ms)	622.1	622.1	578.1	-7

A decline in performance takes place due to energy lost from cratering, and the decline would obviously be affected by differences in the properties of the ground or soil. Note that the author is not aware of any comprehensive studies detailing the amount of the loss for different soil types, likely for the reason that blast experimental data possess significant spreads in results and it is doubtful that the effect of soil properties could be separated from the spread in data with any significant degree of confidence. Empirical hemispherical performance was compiled where the effect of different soils on the decline in performance are averaged. The decline in performance is only moderate, and it is still a fair assumption that spherical performance data can be used with the halfspace approximation to calculate performance in hemispherical situations with the acknowledgement that a slight to moderate over-prediction of loading will result.

## Appendix D

### Blast Clearing

When a blast wave loads a structure surface reflected pressures are produced. Throughout the time history of reflected loading, the pressures do not persist because the presence of the edges of the structure allow relief waves to propagate inward from these edges, Rose [49]. This phenomenon is referred to as blast wave clearing.

Figure D.1 (a) illustrates phases of a planar shock wave impinging on a rectangular structure, while Figure D.1 (b) illustrates an idealized pressure-time history (from the perspective of pressure-time histories affected by clearing) recorded at a given monitoring point located away from one of the corners, outlined in the fine dashed line. When the incident shock  $U$  hits, a reflected wave is created,  $U_r$ . This creates a localized zone of high pressures normal to the surface. Rarefaction waves travel inward from the corners, relieving the high reflected pressures. The relief wave travels at a propagation speed  $c_R$ , which is assumed as the local sound speed in the zone of reflected pressures, and it arrives at the time  $t_\alpha$  labelled in Figure D.1 (b). The approximate time of arrival of the relief wave  $t_\alpha$  depends on how close the point of pressure measurement is to the structure boundary and

the speed of the relief wave  $c_R$ . For the case that the pressure wave is an ideal step wave, eventually after a certain time period beyond when the rarefaction wave has propagated towards the centre and back towards the corner, the pressures exerted on the structure surface decrease to a steady state condition, creating a flow field around the structure. The pressure at the surface normal to the blast wave decrease from the reflected pressure to the incident pressure plus the stagnation pressure from the particle velocity flow multiplied by an appropriate drag coefficient. This behaviour and realization of this condition also occurs for a decaying blast wave of a sufficient duration in comparison to the structure size, but with the further complication that the blast wave pressures are decreasing in time. The time when the condition where the pressure on the surface is roughly equal to the incident pressure plus the stagnation pressure is referred to as the clearing time,  $t_c$ , which is also labelled on the graph in Figure D.1 (b).

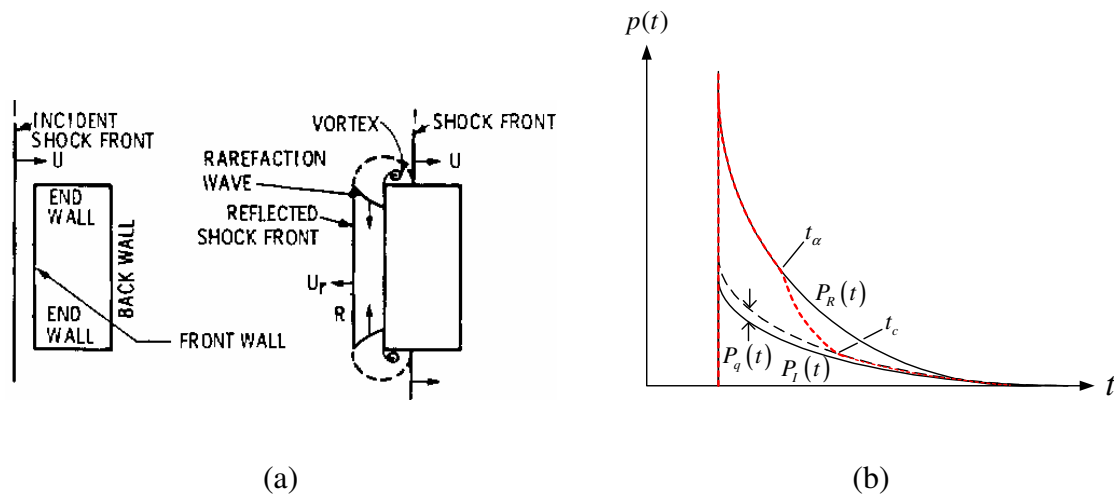


**Figure D.1: Blast wave clearing: (a) diagram of reflection on an orthogonal structure, (taken from structural design for dynamic loads by CH Norris [50]); and (b), resulting pressure–time history on a point on a structure surface affected by clearing**

Note that the change in condition from the arrival of the relief wave at  $t_\alpha$ , to where the pressure is equal to the incident pressure plus the dynamic pressure at  $t_c$ , is not an abrupt

process. One reason for this is that when a rarefaction wave propagates from the corner, instead of the front of the wave developing a sharp front as in compressive waves explained in the section on shock waves, contrarily fronts becomes less sharp with time and propagation distance for rarefaction waves. Also the realization of the cleared state to occur may take several travels of the rarefaction wave. This is a complicated process and several authors have proposed empirical equations for the clearing time. The clearing time in TM5-1300 [11] is given as

$$t_c = \frac{4S}{(1 + \bar{R})c_R}, \quad (\text{D.1})$$

where  $S$  is the smallest edge distance to the centre of the structure, and  $\bar{R}$  is the ratio of the smallest edge distance to the largest edge distances to the centre of the structure. Henrych [5], as well as Kinney and Graham [7], give the clearing time as

$$t_c = \frac{3x}{c_R}, \quad (\text{D.2})$$

where the measurement  $x$  is the shortest distance from the centre of the structure to the edge of the structure.

Both Henrych and TM5-1300 negate the arrival time of the rarefaction wave, and approximate the arrival of the relief wave as starting from the point of time of peak pressure. Citing Kinney and Graham [7], this type of approximation gives an average of the pressure–time history over the structure face, given that the clearing time is advised to be calculated for the most interior point, which is affected by clearing last. Figure D.2 (a) illustrates idealized cleared reflected pressure–time histories from gauge points of varying proximities to an edge, while Figure D.2 (b) shows the averaged pressure–time history,

resulting from making use of the approximation of the arrival of the rarefaction wave to occur at the instant of peak pressure, and approximating the overall clearing time as the clearing time at the point on the structure furthest from any edge.

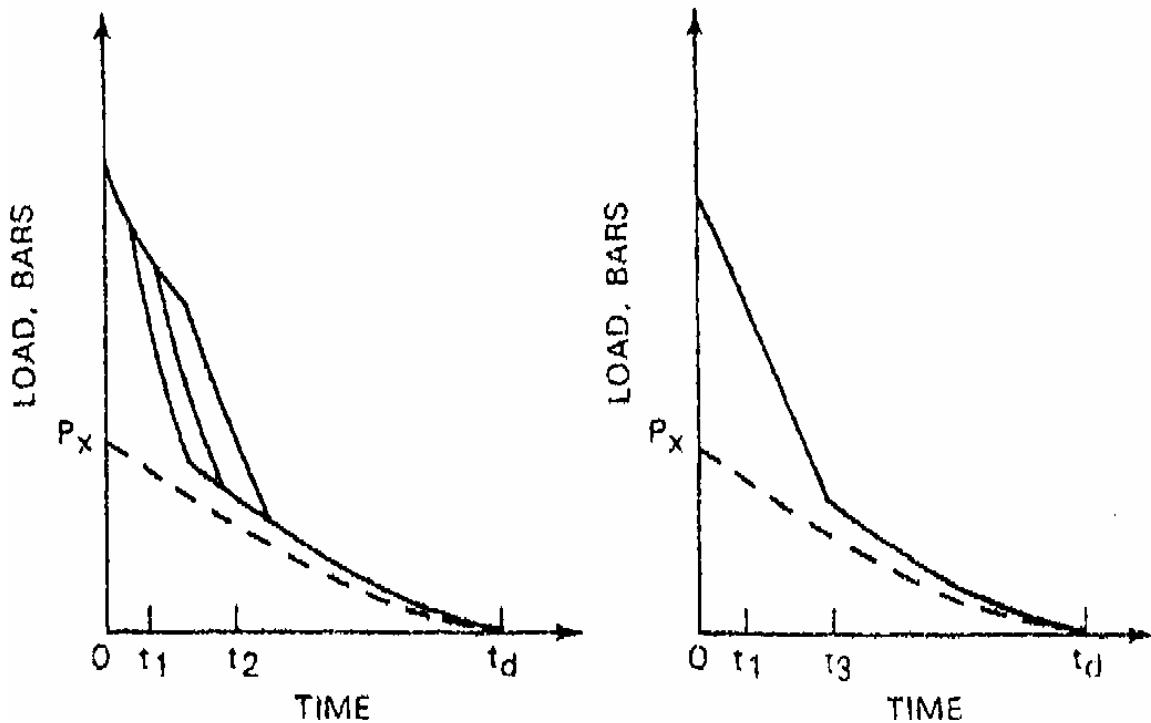


Figure D.2: Idealized clearing: (a) cleared reflected pressure-time histories from gauge points of varying proximities to an edge; and (b), averaged pressure-time history for the entire face, (both figures taken from Kinney and Graham [7])

For use in calculating the clearing time, the local sound speed, which is assumed to be equal to the speed of the rarefaction wave, is given as

$$c_R = \sqrt{\gamma RT}, \quad (\text{D.3})$$

where  $\gamma$ , is assumed as 1.4, and is the gas specific constant relating to the specific heat capacity at a constant temperature to the specific heat capacity at a constant volume for the medium. The universal gas constant,  $R$ , can be taken as 296.86 J/K. Note that this equation requires the temperature, which is not straightforward to determine within the reflected blast wave. Henrych gives equations for calculating the temperature of the inci-

dent wave from the ambient conditions and incident pressure, which can then be used within Eq. (D.3) to calculate the temperature of the reflected wave. More conveniently, the local sound speed as a function of peak incident overpressure is given in Figure D.3.

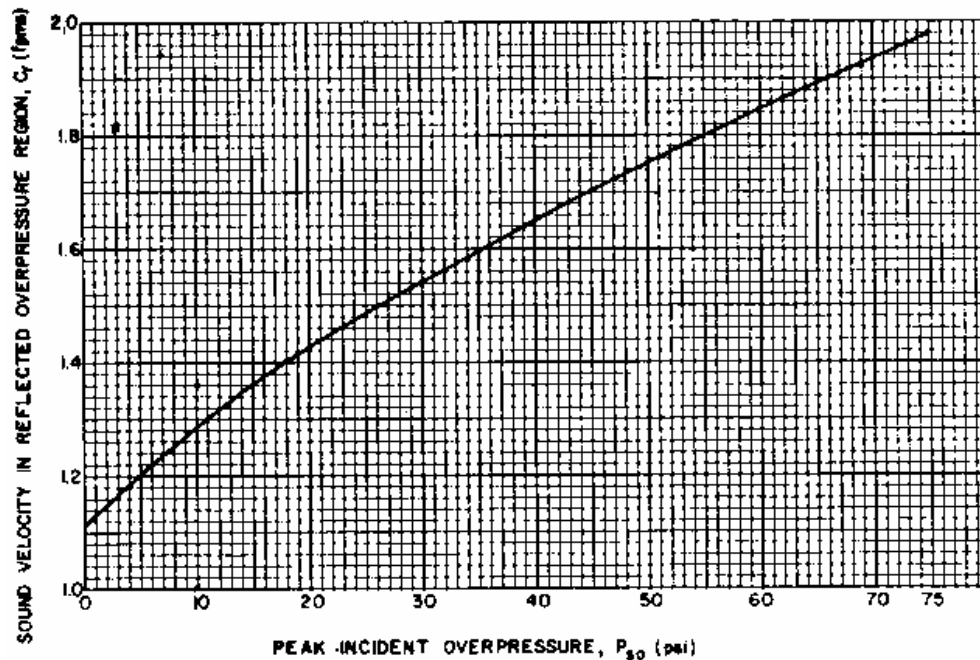
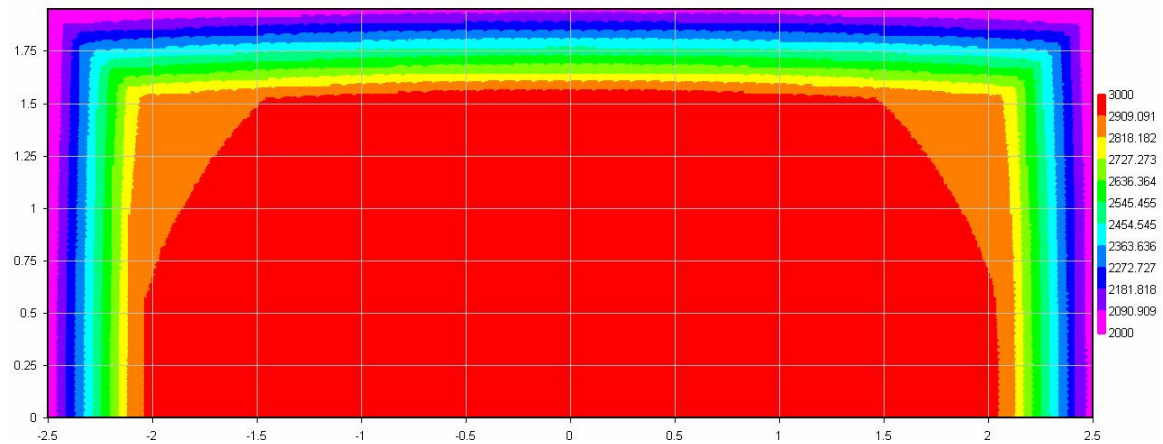


Figure D.3: Sound velocity in reflected overpressure as function of peak incident overpressure, taken from TM5-1300

ConWep [17] also employs a similar algorithm to calculate the effect of clearing on reflected impulse throughout an orthogonal reflecting surface from a hemispherical charge. Figure D.4 shows a contour plot of reflected impulse on a surface calculated from ConWep. The sharp gradient in contours around the edges show the effect of the algorithm used for considering clearing. Clearing reduces the quantity of reflected impulse around the edges of the structure. Because of this, the larger the structure with respect to the duration of the blast wave, the less the reduction in overall impulse from clearing. If the structure is small with respect to the duration of the blast wave, the reduction in reflected impulse due to clearing will be extensive and occur throughout the structure face.





**Figure D.4: Sample plot showing reflected impulse spatial distribution and effect of clearing for a large structure loaded by a blast wave of a short duration, calculated by ConWep**

Rose [49] conducted several Computational Fluid Dynamics (CFD) calculations modeling a rectangular structure of a fixed height-to-width ratio loaded by different hemispherical charges at different ranges of scaled distances. Several of his CFD calculations were validated by experiments and found to be in very good agreement. He formulated an empirical model for calculating averaged reflected impulse based on the scaled charge size and size of the structure based on the results of the CFD calculations, and compared the results of his empirical model to the algorithms outlined in TM5-1300 and ConWep. Figure D.5 (a) shows an example plot of the effect of clearing on the reflected pressure-time history from a large charge on a large structure. Note that this plot shows the difference in arrival times of the rarefaction waves given that gauges 1 through 5 are located at different distances from the structure edge. The graph in Figure D.5 (b) compares the results of his empirical model to experiments, and also compares the results of the algorithms in TM5-1300 and ConWep. Figure D.5 (b) shows greater agreement with experimental results for average reflected impulse compared with TM5-1300 and ConWep.

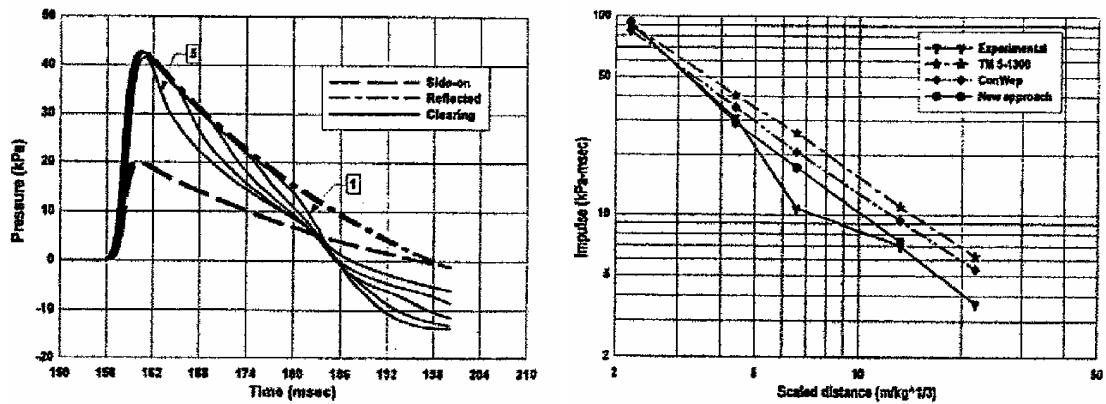


Figure D.5: Results of Rose [49]: (a) sample cleared pressure–time histories illustrating difference between reflected pressure–time histories on infinitely large surface; and (b), comparison of empirical model for calculating averaged reflected impulse on a structure with algorithms from TM5-1300 [11] and ConWep [17]

One of the shortcomings of the empirical model by Rose is that it only yields results for average reflected impulse and does not provide details regarding the spatial distribution of impulse, which may be important for some structural response problems. In addition, the charge location was restricted to be coincident with the centre of the structure.

## Appendix E

### Description of Mach Stem and Performance

In situations when a charge is elevated above ground level (termed ‘height of burst’ (HOB)), empirical loading predictions based on spherical or hemispherical charge configurations may not be accurate because of failure to consider the development of a Mach stem. A Mach stem is formed due to nonlinearities in the shock wave reflection process. Figure E.1 shows the pressure contours resulting from a 50 kg charge at a 1 m height of burst modelled using AutoDyn Computational Fluid Dynamics software [34]. The sequential slides illustrate the formation and propagation of a Mach stem.

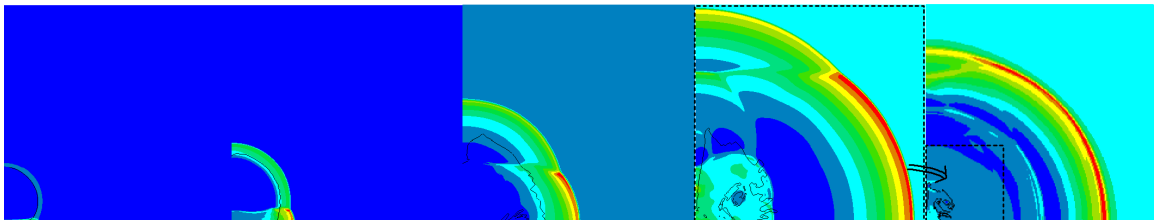


**Figure E.1: Periodic pressure contours showing development and progression of a Mach stem arising from a 50 kg charge at a 1 m height of burst**

Substantial increases in pressures result within the Mach stem upon formation. The Mach stem increases in height, and eventually encompasses the majority of the shock front. By

this time, the substantial differences in pressures inside and outside the Mach stem along the shock front present at the time of its formation have decreased dramatically.

Mach reflection is a complicated topic. The book by Ben Dor [51] presents analytically derived solutions and experimental results for Mach reflection, derived on the basis of applying continuity of mass, momentum, and energy across each of the regions of the atmosphere separated by the incident shock front, reflected shock front, and Mach stem. He also presents comprehensive analytical discussions and experimental results concerning different types of Mach reflection.

Figure E.2 (a) contains an illustration of the formation of the incident and reflected waves forming a Mach stem, and the trajectory of the triple point. Henrych [5] gives a qualitative description of the phenomena. Consider the diagram in Figure E.2 (b) of a shock wave impinging on a rigid surface at an incident angle  $\alpha$ . The point of intersection of the incident wave with the rigid surface, denoted by point  $A$ , travels at a velocity  $c_A$  along the rigid surface. The velocity  $c_A$  is equal to the incident shock speed  $U$  divided by  $\sin \alpha$ . The wave is reflected at an angle  $\beta$ , which is more than  $\alpha$  due to the particle velocities parallel to the surface and the increased sound speed within shock heated air behind the incident wave. The velocity of the reflected pressure wave is shown as  $N_r$ . The velocity of the reflected wave along the direction parallel to the ground,  $N_{r1}$ , is  $N_r \sin \beta$ . At small angles of incidence, the speed  $N_{r1}$  is less than the speed  $c_A$ . If the angle of incidence  $\alpha$  is increased, the velocity  $c_A$  will decrease while the velocity  $N_{r1}$  will increase. At a critical angle,  $\alpha_{crit}$ , which depends on the overpressure at the incident wave front,

the velocity  $N_{r1}$  will be equal to  $c_A$ . Upon further increase in  $\alpha$ , the reflected wave front will overtake the incident wave front, and the point of intersection  $A$  will move away from the barrier surface. A new wave called Mach wave, will arise as a result of the composition of the incident and reflected wave below point  $A$ , as shown in Figure E.2 (c). Point  $A$  is termed the triple point (point intersection of three waves). The front of the Mach wave moves along the barrier surface and the triple point moves away from it, increasing the height of the Mach stem.

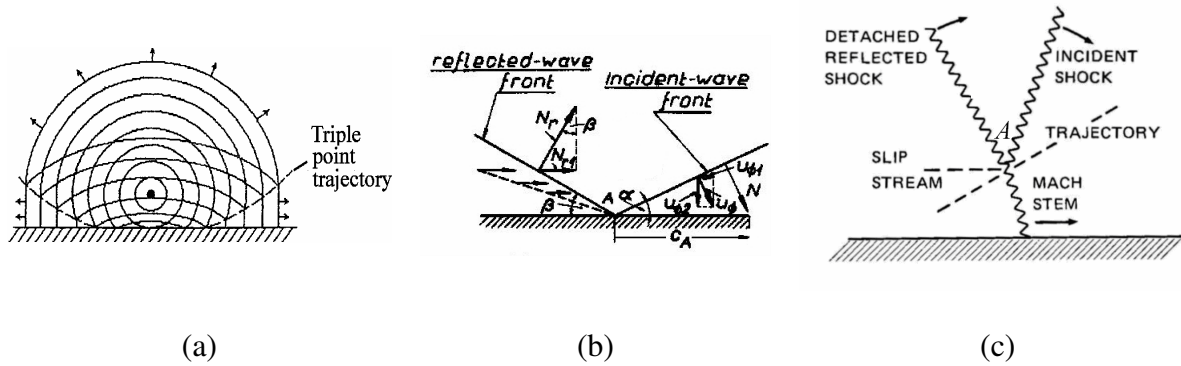


**Figure E.2: Mach reflection from height of burst charge: (a) incident, reflected, and Mach waves, (taken from Gelfand [10]); (b), incident and reflected waves before Mach stem formation, (taken from Henrych [5]); and (c), Mach stem geometry, (taken from Kinney and Graham [7])**

The critical angle at which Mach stem formation occurs depends on the shock overpressure. Kinney and Graham [7] present an analytically derived graph for the critical angle of Mach stem formation as a function of the Mach number of an incident shock wave in Figure E.3 (a). The Mach number is the ratio of the speed of the shock wave front to the ambient sound speed. Assuming an ideal gas and setting  $\gamma = 1.4$ , the Mach number of the incident shock can be calculated by the equation

$$M_x = \sqrt{\frac{6p_s}{7p_a} + 1}, \quad (\text{E.1})$$

where  $p_s$  is the incident overpressure and  $p_a$  is the atmospheric pressure. TM5-1300 [11] gives empirical relationships for the reflection coefficient (the ratio of reflected pressure to incident pressure), as a function of the strength of the incident shock wave and angle of incidence, and is presented in Figure E.3 (b). Note that the abrupt rises in reflection coefficients for strong incident pressures at approximately 40 to 50 degrees incidence angles are a result of Mach stem formation.

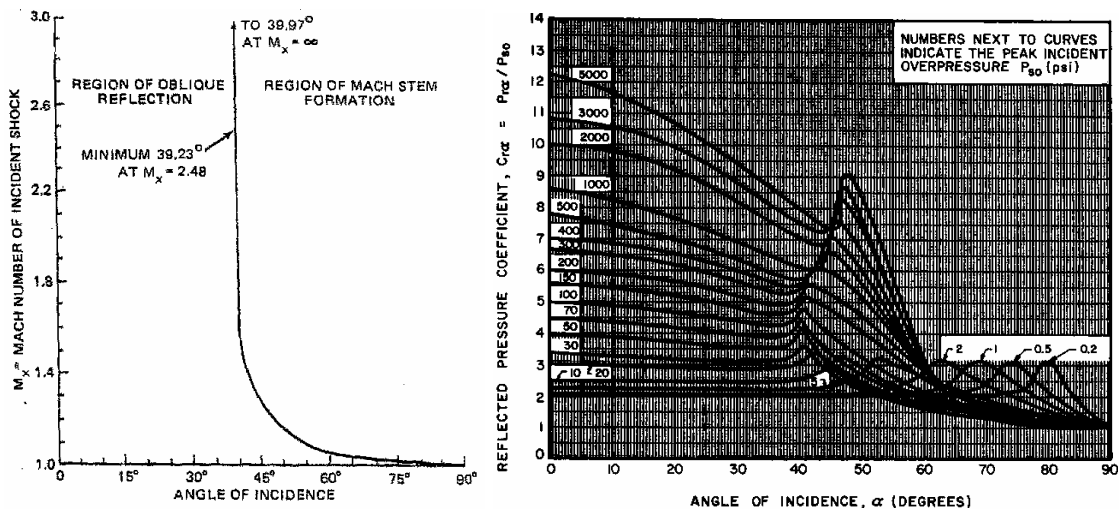
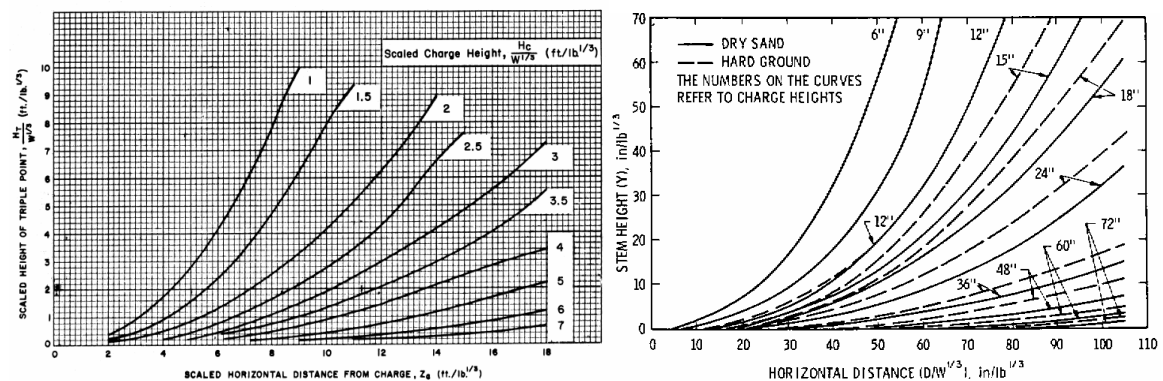


Figure E.3: Figures illustrating formation of Mach stem: (a) analytically derived relationship for formation of a Mach stem as a function of angle of incidence and strength of incident shock, (taken from Kinney and Graham [7]); and (b), Ratio of reflected pressure versus incident pressure, as a function of incident pressure and angle of incidence, (taken from TM5-1300 [11])

For weak shocks, (low Mach numbers), the Mach stem forms at much higher angles of incidence. For very strong incident shocks, the critical angle for Mach stem formation in Figure E.3 (a) remains constant, while in the Figure E.3 (b), for incident pressures above 100 psi, ( $M_x = 2.61$ ), the formation of the Mach stem seems to take place at higher angles. Thus there is some disagreement between Figure E.3 (a) and (b). This can be attributed to changes in equation of state for air.

To calculate the pressure within the Mach stem in a HOB charge scenario, TM5-1300 [11] advises to first calculate the incident pressure and impulse at the slant distance to the point of interest at ground level and assuming a spherical charge configuration. Then using the angle of incidence and the incident pressure, calculate the reflection coefficient using the graph in Figure E.3 (b). The pressure within the Mach stem can be calculated by multiplying the incident pressure with the reflection coefficient. A similar graph is available in TM5-1300 to calculate impulse as well.

TM5-1300 presents a graph for the calculation of Mach stem height, shown in Figure E.4 (a). The result from this graph can be used to determine if the target is within the regime of Mach stem loading. Figure E.4 (b) presents an empirical study illustrating differences in Mach stem trajectories between hard ground and dry sand, and shows lower Mach stem trajectories resulting from HOB scenarios involving dry sand versus hard packed ground. This mechanism may also be responsible for the increased critical angles of Mach stem formation for strong incident shocks evident in Figure E.3 (b).



**Figure E.4: Trajectory of Mach stem: (a) Mach stem trajectories for different scaled burst heights as function of horizontal scaled distance, (taken from TM5-1300 [11]); and (b), differences in Mach stem trajectory between hard ground and dry sand, (taken from Bryant et al. [52])**

To compare the differences in loadings between a HOB configuration (which produces a Mach stem) and a hemispherical configuration, a 50 kg hemispherical charge and a 50 kg charge at a 1 m height of burst were modelled individually in two-dimensional axisymmetric rigid half space using AutoDyn CFD software [34]. A gauge array at a 0.5 m height above ground (which was selected to represent identical slant and horizontal distances between the two charge scenarios), was used to compare the performance of peak incident overpressure and peak incident positive impulse at 0.25 m increments in horizontal distance, as illustrated in Figure E.5 (a). The percent difference between the HOB Calculation 'B' to the hemispherical Calculation 'A' were plotted in Figure E.5 (b).

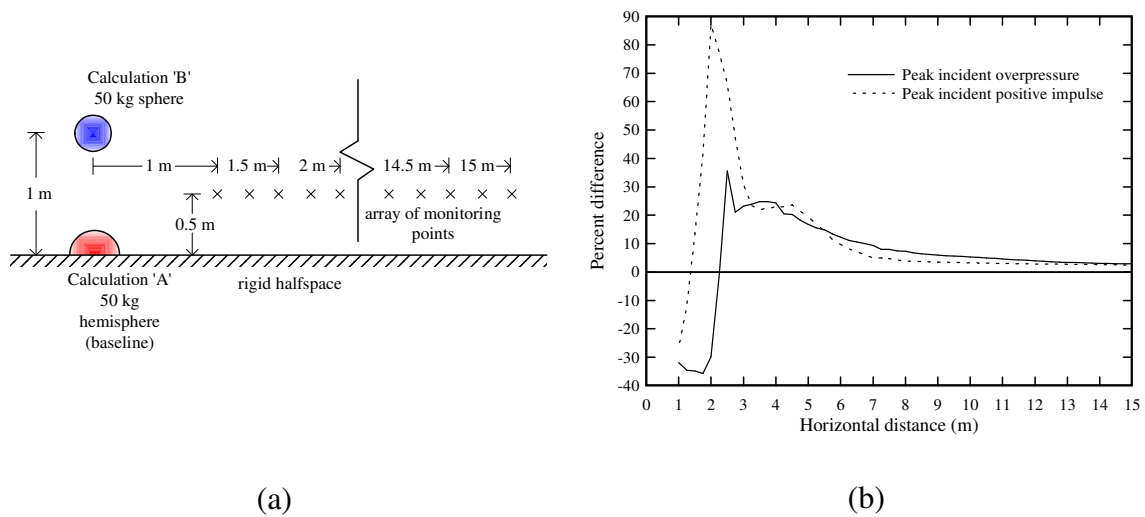


**Figure E.5: CFD calculation setup and results: (a) schematic of charge configurations and monitoring points; and (b), comparison of percent difference in performance between a 1 m HOB configuration (Calculation 'A') to a hemispherical configuration of an equivalent charge mass (Calculation 'B')**

From Figure E.5 (b), for the monitoring point located at 1 m, the loading is 30 % lower in the HOB configuration Calculation 'B' compared with the hemispherical configuration for Calculation 'A'. In Calculation 'B' the Mach stem had formed, but it propagated below the 0.5 m height of the monitoring point at 1 m. Thus the monitoring point at 1 m for



the HOB case recorded the equivalent of a 50 kg spherical charge, while the monitoring point at 1m for the hemispherical case recorded the equivalent of a 100 kg spherical charge. The monitoring point at 2.5 m shows a dramatic increase in pressure and impulse, resulting from the Mach stem passing through this monitoring point location in Calculation 'B'. Although the increase in both pressure and impulse for Calculation 'B' is substantial, with increased distance, the performance begins to converge toward the result of Calculation 'A'. The difference in performance is caused by the timing of the containment of energy. The energy contained through reflection or confinement occurs initially in the hemispherical configuration, but for the HOB configuration, occurs when the incident wave from the sphere reflects from ground. In the far field, the performance of the HOB charge will nearly equal the performance of the hemispherical charge, assuming idealized rigid unyielding ground for both configurations, which was simulated in the CFD calculations.

Recall that blast performance is decreased through loss of confinement by cratering, and less cratering will take place for a HOB charge configuration. Therefore the increase in performance for a HOB versus a hemispherical charge configuration shown by the previous example calculation is understated to an extent. The example hemispherical and spherical empirical comparison calculations presented in the section on empirical performance of TNT resulted in a 13.5 % decline in peak pressure and 7.5 % decline in peak positive impulse lost to cratering. Therefore it is likely that the height of burst performance may be additionally greater by up to these percentages if negligible cratering losses are assumed for a HOB configuration.

The author is not aware of any comprehensive studies outlining the limits of where Mach stem effects should be considered for a HOB configuration, versus when the observation distance is far enough away that the assumption of a hemispherical charge yields reasonable agreement for loading predictions. Such a distance would depend on the scaled height of burst and scaled distance from the charge. However, some general statements can be deduced upon inspection of the Mach stem trajectory graph in Figure E.3 (a). For equal sized charges, decreased heights of burst will yield sooner, (in time and distance), formation of the Mach stem and the higher Mach stem trajectories. It can be deduced that the effect on loading from the Mach stem will decay in a much shorter distance, and assuming a hemispherical configuration for load calculation purposes will be reasonable at much shorter standoffs. At equal heights of burst, increases in charge size will also yield higher Mach stem trajectories, but these increases in trajectory heights are only modest. In lieu of available detailed studies on the limitations of assuming hemispherical charge configurations for purposes of loading calculations, Gelfand's book [10] presents results from a collection of researchers on TNT equivalence for pressure and impulse for different scaled HOB scenarios.

## Appendix F

### Detailed Derivation of Impulse-Dominated Solution

The equation governing the response of a non-linear SDOF system is

$$K_M m \ddot{z} + K_L R(z) = K_L p(t) . \quad (\text{F.1})$$

If the loading is very short compared with the response time of the structure, the majority of the response immediately after the application of loading will be in the form of kinetic energy. The remainder of its response is then governed by its ability to absorb the kinetic energy through strain energy absorption. Since the loading assumed is very short, the amount of movement is negligible and negligible resistance occurs during the loading time, the following equation is valid during the course of loading:

$$K_{LM}(0)m \ddot{z} = p(t) . \quad (\text{F.2})$$

Isolating the second derivative and integrating over the time duration of the loading, which is assumed to be very short, the velocity is

$$\dot{z}_o = \frac{1}{K_{LM}(0)m} \int_0^{t_d} p(t) dt = \frac{I}{K_{LM}(0)m} , \quad (\text{F.3})$$

where  $I$  is the blast impulse, and  $\dot{z}_o$  is the initial velocity resulting from the application of the blast impulse. The loading  $p(t)$  can now be omitted in Eq. (F.1), and Eq. (F.1) can be rewritten as the following, whose solution is subject to the initial velocity  $\dot{z}_o$ .

$$\ddot{z} + \frac{R(z)}{K_{LM}(z)m} = 0. \quad (F.4)$$

It is assumed that negligible displacement has taken place over the very short time duration of the loading, but the mass of the structure has been accelerated to a velocity  $\dot{z}_o$ . Since the loading occurs over a very short time period, the time is assumed to be approximately still at zero. This equation cannot be directly solved for a time history due to the non-linearity. However if we make the substitution

$$\ddot{z} = \frac{d\dot{z}}{dt} = \frac{d\dot{z}}{dz} \frac{dz}{dt} = \dot{z} \frac{d\dot{z}}{dz}, \quad (F.5)$$

and multiply the equation by  $dz$ , the equation reduces to

$$\dot{z}d\dot{z} + \frac{R(z)}{K_{LM}(z)m} dz = 0. \quad (F.6)$$

Integrating and rearranging, we get

$$\frac{\dot{z}_o^2}{2} = - \int_0^{z_{\max}} \frac{R(z)}{K_{LM}(z)m} dz. \quad (F.7)$$

Subbing in the velocity  $\dot{z}_o$  from Eq. (F.3), we get

$$\frac{I^2}{2K_{LM}(0)^2 m^2} = - \int_0^{z_{\max}} \frac{R(z)}{K_{LM}(z)m} dz. \quad (F.8)$$

The first term represents the kinetic energy, and the second represents the strain energy.

Rearranging to isolate the impulse we obtain

$$I = K_{LM}(0) \sqrt{2m \int_0^{z_{\max}} \frac{R(z)}{K_{LM}(z)} dz} . \quad (\text{F.9})$$

Although the maximum displacement cannot be isolated to obtain a closed form expression for the maximum displacement as a function of the applied impulse, the impulse can be isolated to obtain an expression for the impulse required to attain a pre-selected maximum displacement. Therefore  $z_{\max}$  is replaced by  $z_{dmg}$ , which is defined as a pre-selected maximum displacement.  $I$  is replaced with  $I_{crit}$ , representing the critical impulse required to achieve the pre-selected maximum allowable displacement  $z_{dmg}$ , as shown in the following equation

$$I_{crit} = K_{LM}(0) \sqrt{2m \int_0^{z_{dmg}} \frac{R(z)}{K_{LM}(z)} dz} . \quad (\text{F.10})$$

Normally  $K_{LM}$  will decrease with the onset of a plastic hinge, as shown in the differences between elastic and plastic constants in Table F.1. This leads to an increase in deflection. If  $K_{LM}$  is assumed to be constant throughout the entire movement, the equation becomes

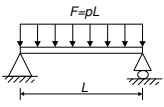
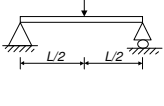
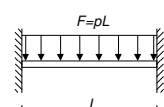
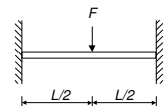
$$I_{crit} = \sqrt{2K_{LM}m \int_0^{z_{dmg}} R(z) dz} . \quad (\text{F.11})$$

From observation of the equation form, no matter the complexity of the resistance function, the amount of impulse absorption ability is proportional to the square root of the area underneath the resistance function up to the selected tolerable damage displacement. Also an increase in mass (with no increase in strength properties), leads to an increase in

impulse absorption capability that is proportional to the square root of the mass increase.

Note that these principles are only valid if impulsive loading is a valid assumption.

**Table F.1: Deformed shapes and derived transformation factors for a variety of cases, (taken from Biggs [19])**

Loading diagram	Strain range	Load Factor $K_L$	Mass Factor $K_M$		Load/mass Factor $K_{LM}$		Max. Resistance $R_m$	Spring constant $k$	Dynamic reaction $V$
			Conc. Mass	Uniform Mass	Conc. Mass	Uniform Mass			
	ELASTIC	0.64	–	0.50	–	0.78	$\frac{8M_m}{L}$	$\frac{384EI}{5L^3}$	$0.39R + 0.11F$
	PLASTIC	0.50	–	0.33	–	0.66	$\frac{8M_m}{L}$	0	$0.38R_m + 0.12F$
	ELASTIC	1.00	1.00	0.49	1.00	0.49	$\frac{4M_m}{L}$	$\frac{48EI}{L^3}$	$0.78R - 0.28F$
	PLASTIC	1.00	1.00	0.33	1.00	0.33	$\frac{4M_m}{L}$	0	$0.75R_m - 0.25F$
	ELASTIC	0.53	–	0.41	–	0.77	$\frac{12M_s}{L}$	$\frac{384EI}{L^3}$	$0.36R_m + 0.14F$
	ELASTIC/PLASTIC	0.64	–	0.50	–	0.78	$\frac{8}{L}(M_s + M_m)$	$\frac{384EI}{5L^3}$	$0.39R + 0.11F$
	PLASTIC	0.50	–	0.33	–	0.66	$\frac{8}{L}(M_s + M_m)$	0	$0.38R_m + 0.12F$
	ELASTIC	1.00	1.00	0.37	1.00	0.37	$\frac{4}{L}(M_s + M_m)$	$\frac{192EI}{L^3}$	$0.71R - 0.21F$
	PLASTIC	1.00	1.00	0.33	1.00	0.33	$\frac{4}{L}(M_s + M_m)$	0	$0.75R_m - 0.25F$

$M_s$  : Moment capacity at support       $M_m$  : Moment capacity at mid span

## Appendix G

### Detailed Derivation of Pressure-Dominated Solution

For an ideal step pressure loading, another energy balance technique can be applied as well. The equation of motion is given as

$$K_M m \ddot{z} + K_L R(z) = K_L p(t) . \quad (\text{G.1})$$

An approximate description is given in Kinney and Graham [7]. This technique is possible only because the normally transient loading is reduced to a constant loading and  $p(t) = p_{step} = p(z)$  applies. The equation of motion Eq. (G.1) becomes

$$K_{LM}(z) m \ddot{z} + R(z) = p_{step} . \quad (\text{G.2})$$

Applying the substitution in Eq. (F.5), the equation becomes

$$K_{LM}(z) m \dot{z} \frac{d\dot{z}}{dz} + R(z) = p_{step} . \quad (\text{G.3})$$

Multiplying the equation by  $dz$  and taking rearranging gives

$$m \dot{z} d\dot{z} = \left( \frac{p_{step} - R(z)}{K_{LM}(z)} \right) dz . \quad (\text{G.4})$$

Integrating both sides gives

$$m \frac{\dot{z}^2}{2} = \int_0^{z_{\max}} \left( \frac{p_{step} - R(z)}{K_{LM}(z)} \right) dz. \quad (G.5)$$

This equation gives the velocity as a function of displacement, which would not be useful normally. However, consider that the velocity increases with  $z$  when the value of  $p_{step} - R(z)$  is positive. When the value of  $p_{step} - R(z)$  is negative the velocity decreases. When velocity reaches zero, maximum displacement has been achieved. Setting the left hand side of the equation to zero we obtain

$$0 = \int_0^{z_{\max}} \left( \frac{p_{step} - R(z)}{K_{LM}(z)} \right) dz. \quad (G.6)$$

This is identical to setting the external work equal to the strain energy as done in Baker [20] for a linear resistance function, which implies a solution at zero kinetic energy. For a given ideal step loading, the maximum displacement can be solved by trial and error or any other numerical technique. Similarly, for a selected damage level  $z_{dmg}$ , the critical step loading  $p_{stepcrit}$  can be solved for by solving the following equation

$$0 = \int_0^{z_{dmg}} \left( \frac{p_{stepcrit} - R(z)}{K_{LM}(z)} \right) dz. \quad (G.7)$$

Unfortunately in this form neither  $z_{dmg}$  nor  $p_{stepcrit}$  can be isolated to give an explicit expression. However, if  $K_{LM}$  is taken as a constant, the equation becomes

$$0 = \int_0^{z_{dmg}} (p_{stepcrit} - R(z)) dz, \quad (G.8)$$

which can be solved as



$$p_{stepcrit} = \frac{1}{z_{dmg}} \int_0^{z_{dmg}} R(z) dz . \quad (G.9)$$

Note that this is equivalent to taking the average of the resistance function up to the assigned damage level  $z_{dmg}$ . However this expression assumes that the evaluation of this function will be highest at  $z_{dmg}$ . But this may not be true for a resistance function that is very complex. For instance, it would be unreasonable if a certain critical step load was calculated at  $z_{dmg}$ , yet at a lower displacement  $z$ , a higher critical step loading resulted from evaluation of this expression. The critical step loading corresponding to  $z_{dmg}$  would automatically be assumed at the higher critical step loading. Therefore the critical step loading can be stated more precisely as the maximum of the cumulative average within the interval of 0 to  $z_{dmg}$  as

$$p_{stepcrit} = \text{Max} \left\{ \frac{1}{z} \int_0^z R(z) dz \right\}; \quad 0 \leq z \leq z_{dmg} . \quad (G.10)$$

This statement has been validated using a single degree of freedom model with complicated piecewise resistance functions through comparison of this technique with values obtained from iteratively solving solutions of the pressure asymptote. Solution of the pressure asymptote through Eq. (G.10) is also graphically shown in Figure G.1.

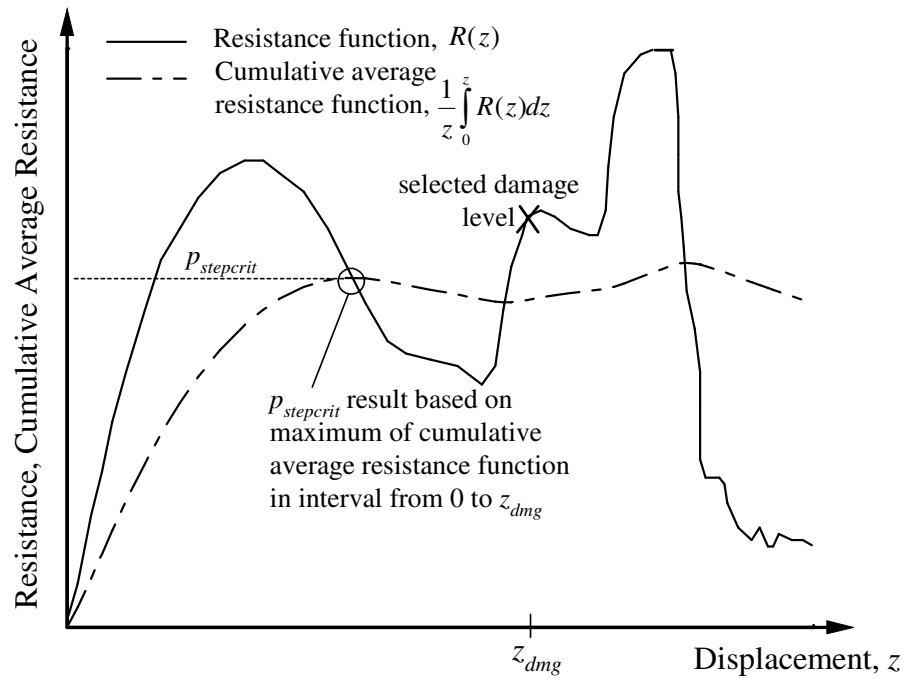


**Figure G.1: Determination of critical step pressure loading for selected damage level,  $z_{dmg}$ , using energy approach**

# Appendix H

## Effect of Including Geotextile in FE Model

The effect of including the geotextile within the FE model is investigated in this Appendix. Belytschko-Tsay membrane elements (Livermore Software Technology Corporation [44]) of a 2 mm thickness were used for the geotextile. Little or no sliding observed between the wire mesh sidewalls and geotextile in the experiments. Therefore a 37.5 mm width and length for the geotextile membrane elements was selected so that nodes could be coincident with the nodes of the wire mesh at 75 mm spacings. The soil in contact with the geotextile was modelled using the automatic surface to surface contacts within LS-Dyna, where the soil could compress and slide with friction against the geotextile and vice versa, but no tension forces could develop. Figure H.1 (a) shows the geotextile and wire mesh portion of the model. Note that the geotextile covering the wire mesh that divided adjacent HB cells was not included in the model. The geotextile covering the wire mesh dividing wall would prevent soil from migrating to adjacent cells, and this purpose was already served by the wire mesh dividing wall in the model, which also acted as a shear wall.

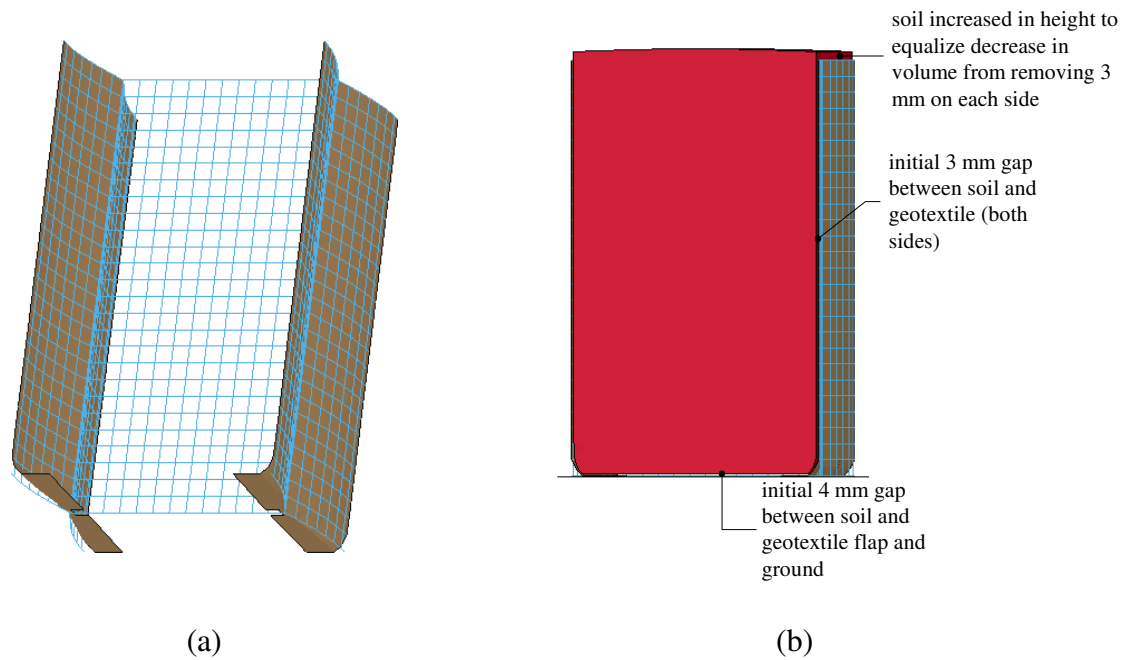


**Figure H.1: FE model with geotextile: (a) geotextile and wire mesh; and (b), FE model with geotextile showing initial gaps before settlement under gravity**

The simplified Johnson-Cook model (given by Eq. 4.7) was used for geotextile based on that its form of stress strain relationship was reasonable to approximate the stress strain relationship from obtained from geotextile tensile tests. The parameters used in the model were

$$E = 27 \text{ MPa}; \quad \nu = 0.35; \quad \text{and} \quad \rho = 400 \text{ kg/m}^3, \quad (\text{H.1})$$

where  $E$ ,  $\nu$ , and  $\rho_s$  are the Young's Modulus, Poisson's ratio, and density, respectively.

The density of the 2 mm thick Geotextile was calculated by weighing a sample of known dimensions. The Johnson-Cook parameters stated in Eq. 4.7,  $A_I$ ,  $B_I$ ,  $c_1$ , and  $n_1$ , were set at  $2.25 \times 10^3$  kPa,  $2.8 \times 10^3$  kPa,  $0.1 \times 10^{-8} \text{ s}^{-1}$ , and 0.36, respectively. Note that since

strain rate dependence has been largely omitted from the FE model, and that no strain rate dependent tensile tests were undertaken, the parameter  $c_I$  was set to be negligible small.

To progressively load the contact surfaces in the model, the width of the soil mass was reduced by 3 mm on each of the sidewalls as shown in Figure H.1 (b), so that contact forces could progressively occur under initial gravity settlement. The height of the soil mass was increased to maintain the same volume of soil within the model. The model was allowed to settle under gravity into the geotextile and wire mesh shape for 500 ms, which from observation of the normal forces at the base of the wall, was sufficient to obtain static equilibrium.

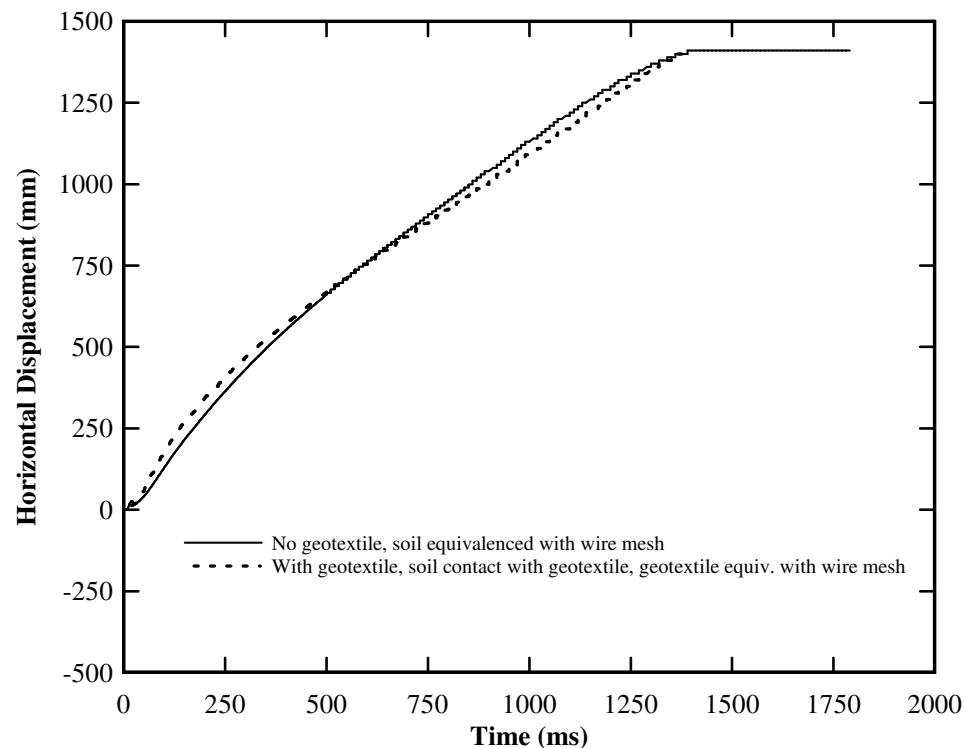


**Figure H.2: Comparison of FE model result with and without geotextile**

Figure H.2 below shows the horizontal displacement-time histories at the upper monitoring point from the model with and without the geotextile. The effect from the geotextile was small (less than three percent difference in the displacement time history). The computational time was approximately four times longer in the model with the geotextile because of the small time steps required to resolve the contacts between the soil and geotextile. Based on the added calculation time and the slight difference in the response, the geotextile was omitted in the FE model.

## Appendix I

### Analytical Solution for Locating Points $E$ and $F$

A more expedient method can be used in lieu of the approximate method if it is assumed that rotation is always increasing with time during the calculation. This is a reasonable assumption if the HB wall is impulsively dominated. Note that we will discuss this assumption shortly. To solve for point  $r_E$ , consider that at a given point  $r_i$ ,  $q(r_i, t)$  can be expressed in a point in time as

$$q(r_i, t) = v(t) - r_i \tan \theta(t) . \quad (1.1)$$

Suppose we wish to find the maximum displacement incurred during the time history of displacement  $q(r_i, t)$  at a given location  $r_i$ . The following equation could be solved for the time at which this occurred

$$\frac{d(v(t) - r_i \tan \theta(t))}{dt} = 0 . \quad (1.2)$$

Finding  $t$  which satisfies this equation would give the point in time at which the maximum displacement at  $r_i$  occurred. Alternatively, we could set the time to the present time

$t_{present}$ , and solve for  $r$  which gives the location at where maximum displacement is on the threshold of occurring, denoted by  $r_E$  as shown in the following equation:

$$\frac{d(v(t_{present}) - r_E \tan \theta(t_{present}))}{dt} = 0, \quad (1.3)$$

where isolation of  $r_E$  gives

$$r_E = \frac{\frac{d(v(t_{present}))}{dt}}{\frac{d(\tan \theta(t_{present}))}{dt}} = \frac{\dot{v}(t_{present})}{\dot{\theta}(t_{present})} \cos^2 \theta(t_{present}). \quad (1.4)$$

In the case that the base compression extends across the entire base where  $r_C$  exceeds  $w$ ,

$$r_E = \min \left\{ \frac{\dot{v}(t_{present})}{\dot{\theta}(t_{present})} \cos^2 \theta(t_{present}), w \right\}. \quad (1.5)$$

This method provides a very convenient and quick way to locate  $r_E$  rapidly without having to store the maximum incurred displacement at large numbers of points along the thickness, and thus this method is far more efficient than the approximate method described in the main body of the thesis. This method is also exact, where the method described in the main body of the thesis is only approximate. The exact method was coded and validated with the approximate method and resulted in virtually the same values calculated. This method is also particularly convenient for use with Runge-Kutta integration because, in addition to displacements, velocities are also incremented and readily available to use in the above equation. Thus this expression requires little additional computational effort to calculate.



Using a similar methodology to locate point  $r_F$ , and considering that a value of  $r_E$  at a specific point in time in the past corresponds with  $r_F$  currently, the exact solution for the point in time  $t_{past}$  in which this occurred is given as

$$\frac{v(t_{present}) - \lambda v(t_{past})}{\tan \theta(t_{present}) - \lambda \tan \theta(t_{past})} = \frac{\dot{v}(t_{past})}{\dot{\theta}(t_{past})} \cos^2 \theta(t_{past}) = r_F = r_{Epast} . \quad (1.6)$$

Finding  $t_{past}$  for which this equation is satisfied will provide an answer for  $r_F$ . However this solution is not convenient to implement, as it would require the program to search for the time at which this expression was satisfied through previous time periods within the recorded solution and interpolate between the results. In comparison the approximate method may be a more efficient alternative for calculating  $r_F$ . There is an exception however, in the case of a perfectly plastic soil in compression with an infinite unloading modulus, point  $F$  is equal to point  $E$ , and the computer program would only require point  $E$ . Therefore use of the analytical solution would be more efficient. In fact the analytical solution in this case is many times more efficient than the approximate one. But in terms of the computational time within the overall program, the location of these points of intersection only consumes a relatively small portion of the calculation effort. On average, for perfectly plastic soil with an infinitely high unloading modulus  $K$ , implementing the approximate method for locating point  $E$  took 2.2 seconds to run using a single 2.2 GHz Intel Pentium® processor, while using the exact solution reduced the run time to 1.9 seconds. Thus this method is only slightly more efficient for perfectly plastic soils in compression, but for soils that are not perfectly plastic, the exact method is cumbersome to implement and computationally expensive.

Regarding the validity of the assumption that the rotation is always positive and increasing, in this problem, we are only concerned with positive rotation up to maximum rotation or overturning, whichever occurs first. After either of these conditions is met the calculation is terminated. For impulsive loading normally rotation is positive and increasing up to the point of maximum rotation or overturning. But one type of loading that could lead to a violation of this assumption would be if there were multiple pressure waves, where the wall may rotate positively, start to rotate negatively, and then be caused to rotate positively again by an additional wave. However, since the wall is impulse dominated and the response lasts for several hundred milliseconds, multiple blast waves created by reflections off adjacent structure surfaces typically will not be spaced far enough apart in time for this to occur. Using this method is reasonable for almost all cases of loading due to the wall being impulse dominated, which is a valid assumption according to the work by Scherbatiuk [24].

## Appendix J

### Calculation of Change in c.g. Location with Local Shear Deformation

One of the assumptions made in the formulation of the Rigid-Body Hybrid model was that the location of the centre of gravity (c.g.) and the second moment of area about the centre of gravity  $I_{cg}$  only undergoes negligible changes due to the deformation at the corner. As an investigation of the magnitude, consider the diagram in Figure J.1 of an idealized HB wall that has undergone shear displacement at the base  $s$ , where the shape of the sheared portion of the wall has been idealized as a 1:1 slope. The c.g. in the undeformed shape is given by  $cg_0$ , measured from the left side as  $\bar{x}_0$ , while the centre of gravity for the deformed shape is given by  $cg_1$ , measured from the left side as  $\bar{x}_1$ .

Measurements  $\bar{x}_0$  and  $\bar{x}_1$  can be calculated as

$$\bar{x}_0 = \frac{w}{2}, \text{ and} \quad (\text{J.1})$$

$$\bar{x}_1 = \frac{w}{2} - \frac{s^2}{2h}. \quad (\text{J.2})$$

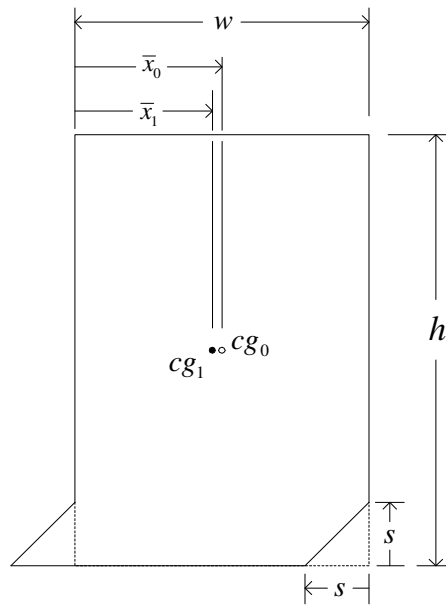


**Figure J.1: Diagram for calculation of change in c.g. position from idealized shear deformation of wall**

The distance from  $cg_0$  to  $cg_1$ , given as  $\Delta cg$ , can be calculated as

$$\Delta cg = \bar{x}_0 - \bar{x}_1 = \frac{s^2}{2h}. \quad (\text{J.3})$$

Through observation of the results of the FEM model, an approximate value for the maximum shear attained in this idealised shape is 25 cm for a two-course Mil 3 wall of height of 195 cm and an average width of 110 cm. The change in  $cg$  can be evaluated as

$$\Delta cg = \frac{25^2}{2(195)} = 1.6 \text{ cm}. \quad (\text{J.4})$$

The calculated shift in the centre of gravity is not large compared to the overall shear of 25 cm or the average width of 110 cm. The moment of inertia about the original  $cg$  in the undeformed shape can be found as

$$I_{cg_0} = \frac{wh}{12} (w^2 + h^2). \quad (\text{J.5})$$

The moment of inertia about  $cg_1$  can be found as

$$I_{cg_1} = \frac{wh}{12}(w^2 + h^2) + \frac{ws^3}{12}\left(4 - 3\frac{s}{h}\right) = I_{cg_0} + \frac{ws^3}{12}\left(4 - 3\frac{s}{h}\right). \quad (J.6)$$

For a wall of the same dimensions as stated, the percent difference in the second moment of inertia from the undeformed shape to the deformed shape can be calculated as

$$\%diff = \frac{s^3\left(4 - 3\frac{s}{h}\right)}{h(w^2 + h^2)} \times 100 = \frac{25^3\left(4 - 3\frac{25}{195}\right)}{195(110^2 + 195^2)} \times 100 = +0.578\% . \quad (J.7)$$

Thus the difference in the rotational inertia is very small and it is a reasonable assumption to assume the changes in  $I_{cg}$  to be negligible. This is of benefit considering the difficulty in the calculation caused by accounting for both the bulges and the shear in the wall, and that the actual shape of the sidewall near the base due to shear has not been formulated within the Rigid-Body Hybrid model.

# Appendix K

## Further Blast Loading Details and CFD

Uniformly distributed loading was assumed as an approximation in the experiments. The spatial differences in pressures along the length of wall generally depends on both the differences in distance to the wall surface, (centre of the wall compared with the edge), as well as differing off-normal angles of incidence to the wall surface. Figure K.1 shows the effect of reflected pressure on differing off normal angles to the wall surface. Note that in the experiments, the off-normal angle did not exceed  $15^\circ$ , and minimal differences are shown in the reflection coefficient for the magnitudes of incident pressures in the experiment. Little change in loading along the wall length is also predicted by ConWep [17] as well as Computational Fluid Dynamics (CFD). For security reasons the charge weight, shape and dimensions, type of explosive used, size, shape, and type of booster charge, height of burst, and distance have been omitted.

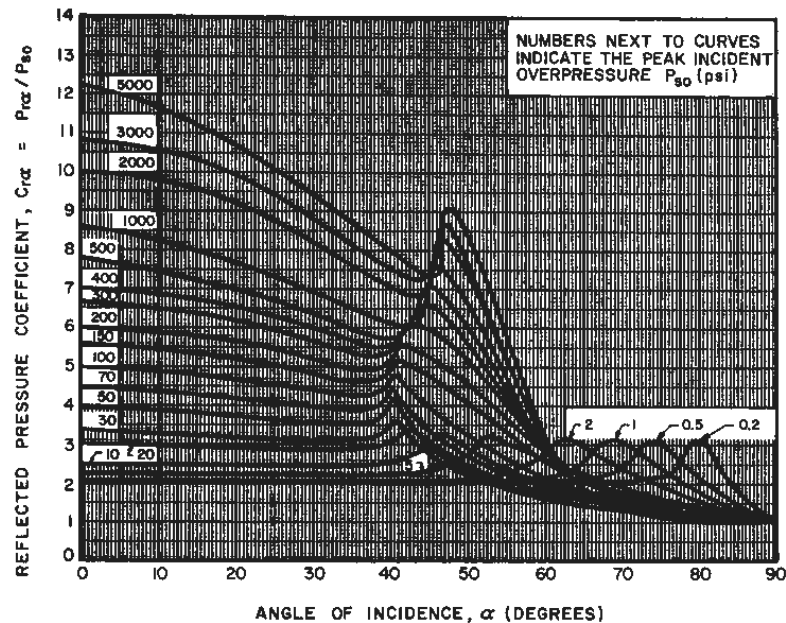
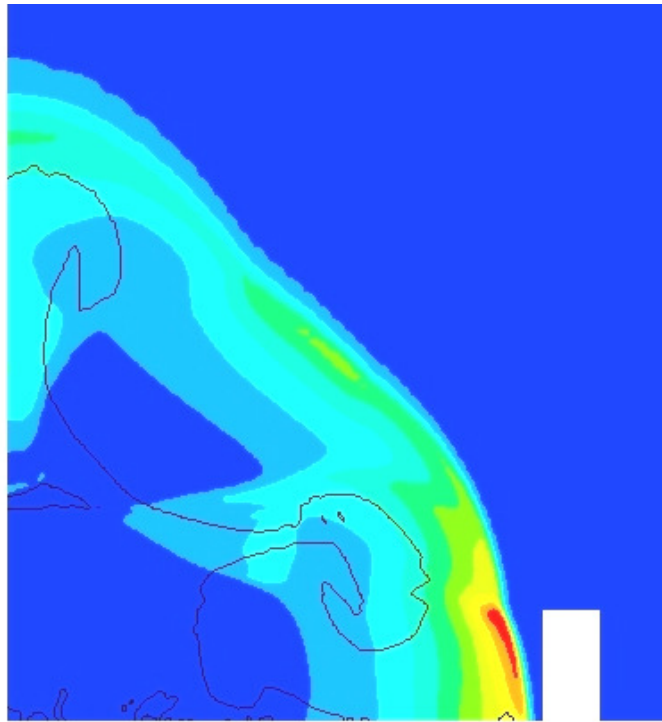


Figure K.1: Ratios of reflected to incident pressure for different angles of incidence (source: TM5-1300 [11])

The charge was configured in a height of burst which produced a Mach stem. Figure K.2 shows the pressure wave contours before the pressure wave impacted the wall in one of the experiments. The height of the Mach stem upon reaching the wall was at least the height of the wall in all experiments. As a result, the loading was approximately uniform along the height of the wall and little difference in the response of the FE model occurred when a spatially distributed load was used.



**Figure K.2: Pressure contours obtained from CFD showing Mach stem height before impacting wall**

In the experiments the pressures on the rear of the wall were not measured. In retrospect measurement of the pressure on the rear of the wall should have been conducted for validation that the loading was negligible on the rear of the wall in comparison to the front, and thus is recommended for future experiments. AutoDyn CFD software [34] was used to calculate the pressure-time history on the front and rear of the wall. Figure K.3 shows the pressures at the rear of the wall were very small compared with that on the front. The peak reflected pressure on the rear of the wall at mid-height is less than 3 % of the reflected pressure on the front face at mid-height, where the peak pressures differed by a factor of 35 times, which may be counter-intuitive.



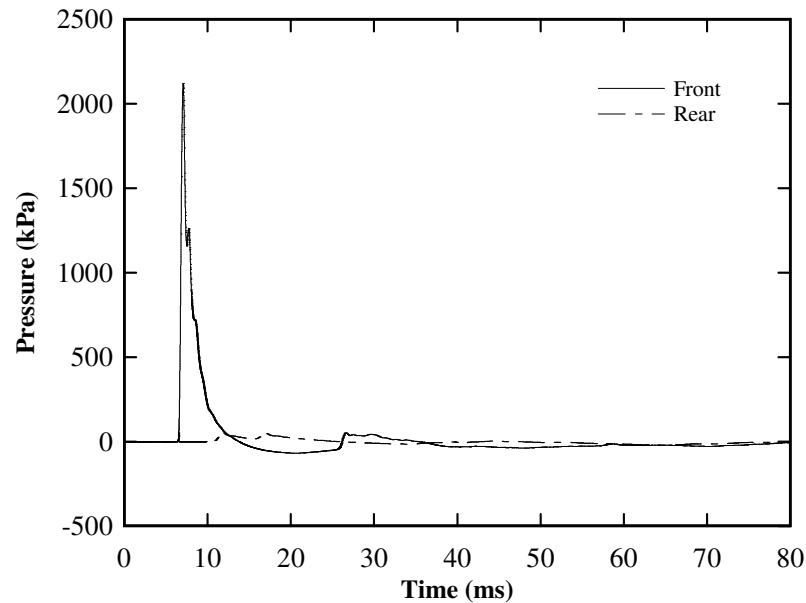


**Figure K.3: Comparison of front and rear loading from CFD**

Rose et al. [53] published a study on the effectiveness of cantilever walls in attenuating blast waves. In their study, they compared the reductions in terms of what incident pressures would have resulted without the wall at the same location. In the same paper, Rose also gives a contour plot for a single scenario showing the reductions behind a wall as a percentage of the pressures in absence of a wall as shown in Figure K.4. Note that the CFD calculation also assumes that the wall is rigid and survives the blast, which may not always be the case. Figure K.4 shows that at mid-height, only 10 to 20 % of the pressure results in comparison to incident pressure without a wall, which equates to a factor of 5 to 10 times less loading. Considering that the reflection coefficient in the experiments was approximately 6, the 5 to 10 times reduction in incident pressure would equate to 30 to 60 times reduction in reflected pressure. The 35 times reduction encountered in the CFD-simulated results in Figure K.3 is within this range.

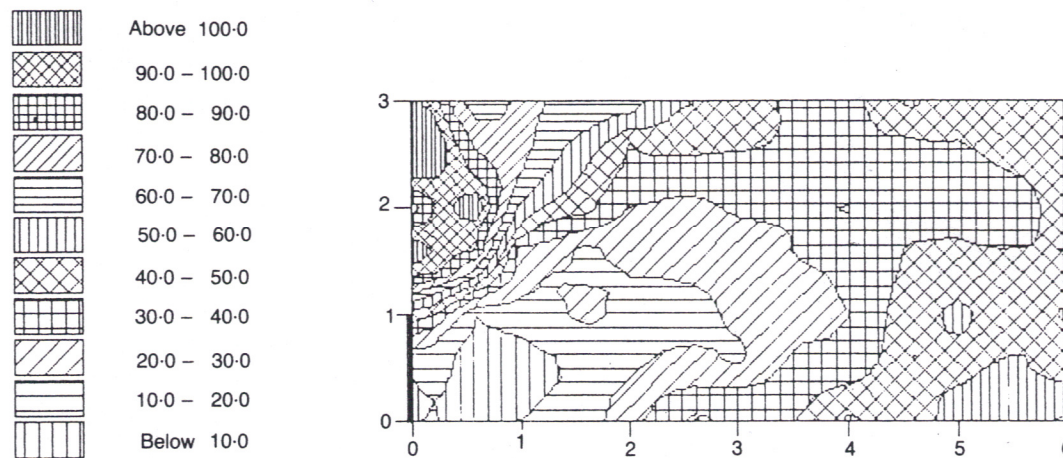


**Figure K.4: Contour plot of pressure with wall in place as a percentage of pressure without wall,**  
(Source: Rose et al. [53])

In Figure K.3, the net impulse of the positive and negative phases on the rear face of the wall was slightly positive. However the magnitude of net impulse on the rear face of the wall was less than 3 % of the net impulse on the front face of the wall. Since the wall response is largely governed by the impulse of the loading (Scherbatiuk et al. [24]), it was concluded that in this case, using the pressure recorded on the front face of the wall was a sufficient approximation for the net loading on the wall. Comparison of the response of the FE model using only the pressure at the front versus using both the front and rear pressures for loading showed little difference.